António José Espadinha Vieira Soares

Licenciado em Ciências da Engenharia Mecânica
Licenciado em Estudos Ingleses: Especialização em Comunicação
Mestre em Ciências da Comunicação

Numerical simulation of vegetated flows using RANS equations coupled with a porous media approach in OpenFOAM

Dissertação para obtenção do Grau de Mestre em

Engenharia Mecânica

Orientador: José Manuel Paixão Conde, Prof. Auxiliar,
Universidade Nova de Lisboa

Júri

Presidente: Doutor José Fernando de Almeida Dias
Arguente: Doutor Eric Lionel Didier
Vogal: Doutor José Manuel Paixão Conde

FACULDADE DE CIÊNCIAS E TECNOLOGIA
UNIVERSIDADE NOVA DE LISBOA

Março, 2017

Numerical simulation of vegetated flows using RANS equations coupled with a porous media approach in OpenFOAM

Este documento foi gerado utilizando o processador (pdf)LaTeX, com base no template "unlthesis" [1] desenvolvido no Dep. Informática da FCT-NOVA [2]. [1] https://github.com/joaomlourenco/unlthesis [2] http://www.di.fct.unl.pt

Para a minha mãe...

Acknowledgements

First and foremost my thanks go out to FCT-UNL for taking me in and providing me with the chance to fulfil my dreams and ambitions, to my adviser, Prof. José Paixão Conde, our course coordinator Prof. António Mourão, Prof. Alberto Martinho, Prof. Daniel Vaz, Prof. Ana Sá, Prof. António Gil de Oliveira Santos and my colleagues at the Departamento de Engenharia Mecânica e Industrial (DEMI) Computational Fluid Dynamics (CFD) Lab. I'd like to thank all of my friends and family, in particular my mother, Prof. Maria Antónia Nicolau Espadinha, without whom none of this work would have been possible.

Abstract

The purpose of this Masters thesis is to study the use of an alternative formulation of a submerged vegetation layer in open channel flow, using a porous medium instead. The turbulent flow is modelled with the use of Reynolds-Averaged Navier-Stokes (RANS) equations using the open-source toolbox Open Field Open Access Manipulation (OpenFOAM). The porous medium is defined according to the Darcy-Forchheimer model which requires the determination of the intrinsic permeability and passability coefficients. These parameters are estimated from the average geometric properties of the vegetation elements in a method validated in previously published studies. This method eliminates the ad hoc calibration required in the use of global drag coefficients in the RANS equations traditionally used to take into account the effects of submerged vegetation on open-channel flow. The use of this methodology has been previously partially validated using commercial numeric simulation codes. However, these tend to be costly solutions and very limited in their customizability. This study seeks to partially reproduce work done on the commercial code ANSYS-CFX in an open-source code environment as well as to try and conduct numeric studies of other open-channel flow experiments with a range of varied submerged vegetation parameters (ergo, porosity values) so as to not only test the robustness of the numeric code but of this methodology as well. This work's methodology also took on a more simplified numerical solution approach by use of a less robust algorithm (with no time derivative) than previously conducted studies. It was then possible to further understand the types of phenomena present in this type of flow and the required theoretical considerations which should be taken into account so as to produce valid computational study results.

Keywords: OpenFOAM, porousSimpleFOAM, SIMPLE, Porous medium, Porosity, Submerged vegetated flow, open-channel flow, RANS, Turbulence, open-source

Resumo

O propósito desta tese de Mestrado incide no uso de um método alternativo no caso particular de uma camada de vegetação densa submersa em canal aberto, modelando esta como um meio poroso. O escoamento e a sua turbulência é modelado com as equações RANS usando a ferramenta de simulação numérica de código aberto OpenFOAM. O meio poroso é definido recorrendo ao modelo Darcy-Forchheimer que requer a determinação de dois parâmetros; o coeficiente de perda de carga devido às forças de viscosidade e o coeficiente de perda de carga devido às forças de inércia. Estes parâmetros são estimados a partir da média geométrica dos elementos da vegetação através de métodos validados em estudos prévios, eliminando a calibração ad hoc necessária para o uso dos métodos mais tradicionais que fazem uso de um coeficiente global de arrasto nas equações RANS para ter em conta a perda de carga induzida pela vegetação submersa. A metodologia de uso de meio poroso para este fim já foi validada em parte em estudos prévios usando códigos de simulação numérica comerciais. Porem estes tendem a ser dispendiosos e limitados no que diz respeito à sua modificação para aplicação a casos muito específicos. Este estudo visa tentar reproduzir em parte o que já foi comprovado com o código comercial ANSYS-CFX em ambiente código aberto assim como tentar reproduzir numericamente os valores de outros estudos experimentais com parâmetros de vegetação (logo, também de porosidade) variados de modo a averiguar o quão robusto é tanto o código numérico assim como a metodologia. A metodologia deste trabalho também consistiu numa maior simplificação da simulação numérica, usando um algoritmo menos robusto (sem derivada temporal) que o algoritmo usado previamente. Foi possível assim aprofundar o conhecimento dos fenómenos presentes neste tipo de escoamento e os requisitos teóricos fundamentais que devem ser contemplados na simulação efectiva deste tipo de escoamentos.

Palavras-chave: OpenFOAM, porousSimpleFOAM, SIMPLE, Meio poroso, vegetação submersa, escoamento em canal aberto, RANS, Turbulência, código aberto

Contents

List of Figures

List of Tables

Listings

Acronyms

1D	One Dimensional
2D	Two Dimensional
3D	Three Dimensional
ASM	Algebraic Stress Model
BSL	Menter's BaSeLine $k-\omega$ turbulence model
BSL-EARSM	Baseline Explicit Algebraic Reynolds Stress Model
CAD	Computer Aided Design
CFD	Computational Fluid Dynamics
CFX	ANSYS-CFX
COHM	CoHerence Method
DEMI	Departamento de Engenharia Mecânica e Industrial
DNS	Direct Numerical Simulation
EARSM	Explicit Algebraic Reynolds Stress Model
FCF	Flood Channel Facility
FCT	Faculdade de Ciências e Tecnologia
FD	Finite Difference
FEM	Finite Element Method

FP	Flood Plain
FVM	Finite Volume Method
GNU	GNU's Not Unix
GUI	Graphical User Interface
HFA	Hot Film Anemometry
HWA	Hot Wire Anemometry
LDA	Laser Doppler Anemometry
LES	Large Eddy Simulation
LRR	Launder-Reece-Rodi pressure strain rate correlation model
LRR-QI	Quasi-isotropic LRR
LRR-IP	Isotropization of production model of the LRR
MC	Main Channel
MIT	Massachusetts Institute of Technology
MPI	Message Passing Interface
MRF	Multiple Reference Frame
OpenFOAM	Open Field Open Access Manipulation
PIV	Particle Image Velocimetry
RANS	Reynolds-Averaged Navier-Stokes
RAS	Reynolds-Averaged Simulation
REV	Representative Elementary Volume

RHS	Right Hand Side
RSM	Reynolds Stress Model
SERC	Science and Engineering Research Council
SIMPLE	Semi-Implicit Method for Pressure Linked Equations
SKM	Shiono and Knight Method
SMC	Second Moment Closure
SMC-ω	Second Moment Closure - Omega Reynolds Stress Model
SSG	Speziale-Sarkar-Gatski pressure strain rate correlation turbulence model
SST	Menter's Shear-Stress Transport turbulence model
STDEV	STandard DEViation
STL	STereoLithography file format
SWAK4FOAM	SWiss Army Knife for FOAM
TKE	Turbulent kinetic energy
UNL	Universidade Nova de Lisboa
VARANS	Volumetric-averaged Reynolds-averaged Navier-Stokes
VoF	Volume of Fluid
WDCM	Weighted Divided Channel Method
WJ-EARSM	Wallin & Johansson Explicit Algebraic Reynolds Stress Model

Symbols List

Symbol	Description	Units
a	Frontal area per volume	$[m^{-1}]$
a_I	Linear resistance coefficient	$[s{\cdot}m^{-1}]$
a_I'	Mathematical adjustment constant used in fully turbulent flow regime	[-]
a_I''	Mathematical adjustment constant used in Darcy flow regime	[-]
A	Channel cross-section area	$[m^2]$
A_p	Surface area of the particle	$[m^2]$
A_{sp}	Surface area of an equivalent volume sphere	$[m^2]$
$A_i{}^m$	Interfacial area between the solid and the fluid phase within a porous matrix	$[m^2]$
b	Blade thickness	[m]
b_C	Main channel bottom width in asymmetric channels	[m]
b_I	Non-linear resistance coefficient	$[s^2{\cdot}m^{-2}]$
b_I'	Nonlinear constant used in fully turbulent flow regime	[-]
B	Channel width	[m]
B_{fp}	Floodplain width	[m]
B_{mc}	Main channel width	[m]
C	Scalar volume fraction	[-]
C_F	Non-linear Forchheimer coefficient for the volumetric average Darcy-Forchheimer extended model	[-]
C_β	Porous media interface stress jump coefficient	[-]
C_A	Viscous term constant	[-]
C_B	Inertial term constant	[-]
C_D	Canopy drag coefficient	[-]
C_μ	Empirical constant	[-]
$C_{\epsilon 1}$	Empirical constant	[-]

Symbol	Description	Units
$C_{\epsilon 2}$	Empirical constant	[-]
C_E	Ergun constant	[-]
d	Characteristic diameter/width of the canopy elements	[m]
d_{eq}	Equivalent particle diameter	[m]
d_p	Particle diameter	[m]
d_{sd}	Sauter mean diameter	[m]
d_v	Average diameter of cylinders analogous to the synthetic grass elements used in an experiment	[m]
d_{vs}	Actual diameter of a particle	[m]
D	Darcy/linear coefficient α in **OpenFoam**	[m^{-2}]
D_V	Spatially averaged drag	[-]
e_1	*porosityProperties* axis-rotation vector	[-]
e_2	*porosityProperties* axis-rotation vector	[-]
e_3	*porosityProperties* axis-rotation vector	[-]
f_i	Body forces	[N]
F	Forchheimer/Non-Darcy coefficient β in **OpenFoam**	[m^{-1}]
g	Gravitational acceleration	[$m \cdot s^{-2}$]
h_b	Main Channel height	[m]
h_{MC}	Main Channel depth	[m]
h_{fp}	Floodplain height	[m]
h_{FP}	Floodplain height	[m]
h	Canopy height	[m]
h_r	Relative depth	[-]
h_v	Vertically uniform grass height	[m]
H	Flow depth	[m]
k	Turbulence kinetic energy	[$m^2 \cdot s^{-2}$]
I	Hydraulic gradient	[$m \cdot Kg^{-1}$]
k_S	Nikuradse's absolut roughness	[m]
K	Intrinsic permeability	[m^2]
K_{app}	Apparent permeability	[m^2]
K_f	Hydraulic conductivity tensor	[$m \cdot s^{-1}$]
L	Characteristic length	[m]
L_c	Canopy drag length scale	[m]
l	Turbulence length-scale	[m]
p	Pressure	[Pa]

Symbol	Description	Units
p'	Pressure deviations	[Pa]
P_k	Turbulence kinetic energy production	[$m^2 \cdot s^{-2}$]
Q	Flow discharge	[$m^3 \cdot s^{-1}$]
$\mathbf{R}$	Total drag per unit volume acting on the fluid by the action of the porous structure	[-]
Re	Reynolds number	[-]
Re_d	Reynolds number for time and spatially averaged velocity	[-]
Re_p	Porous medium Reynolds number	[-]
$-\overline{u_i' u_j'}$	Reynolds stress tensor	[$m^2 \cdot s^{-2}$]
S	Spacing between canopy elements	[m]
S_i	Source term in Navier-Stokes equations	[-]
S_V	Specific surface area	[$m^2 s$]
S_v	Specific inter-facial area	[$m^2 s$]
s	Clearance for the non-obstructed flow passage	[m]
t	Time	[s]
T	Temperature	[K]
T_F	Solid matrix temperature	[K]
T_S	Fluid phase temperature	[K]
U	Streamwise velocity	[$m \cdot s^{-1}$]
$\mathbf{u}_s$	Seepage velocity vector	[$m \cdot s^{-1}$]
u	Longitudinal velocity	[$m \cdot s^{-1}$]
u_i	Velocity component in the i direction, u, v or w	[$m \cdot s^{-1}$]
u_i'	Velocity component fluctuations in the i direction	[$m \cdot s^{-1}$]
u'	Longitudinal velocity fluctuations	[$m \cdot s^{-1}$]
u_*	Frictional velocity	[$m \cdot s^{-1}$]
$\langle \mathbf{u} \rangle^i$	Intrinsic (fluid) average of $\mathbf{u}$	[$m \cdot s^{-1}$]
U_A	Cross section bulk velocity	[$m \cdot s^{-1}$]
U_{max}	Maximum stream-wise velocity	[$m \cdot s^{-1}$]
U_{MC}	MC bulk velocity	[$m \cdot s^{-1}$]
U_{FP}	FP bulk velocity	[$m \cdot s^{-1}$]
$\mathbf{u}$	Velocity vector comprised by the components u, v and w	[$m \cdot s^{-1}$]
U_i	Mean velocity component in the i direction, U, V or W	[$m \cdot s^{-1}$]

Symbol	Description	Units
$\mathbf{u}_D$	Darcy velocity	[m·s^{-1}]
v	Lateral velocity	[m·s^{-1}]
v'	Lateral velocity fluctuations	[m·s^{-1}]
V_p	Volume of a particle	[m^3]
v_{cf}	Cross flow (secondary flow) velocity	[m·s^{-1}]
w	Vertical velocity	[m·s^{-1}]
w'	Vertical velocity fluctuations	[m·s^{-1}]
x	Longitudinal Cartesian Coordinate	[m]
y	Lateral Cartesian coordinate	[m]
y^+	Dimensionless wall distance in the y direction	[-]
z	Vertical Cartesian coordinate	[m]
z^+	Dimensionless wall distance in the z direction	[-]
z_0	Displacement height	[m]
z_m	Roughness height	[m]

Greek Symbols

α	Darcy/Linear coefficient	[m^{-2}]
α_ω	$k-\omega$ turbulence model empirical constant	[-]
β	Forchheimer/Non-Darcy coefficient	[m^{-1}]
β^*	Model constant	[-]
β_ω	$k-\omega$ turbulence model empirical constant	[m^{-1}]
β'	$k-\omega$ turbulence model empirical constant	[-]
δ_e	Penetration length scale	[-]
Δ	Variation in a given scalar	[-]
δ_{ij}	Kronecker Delta	[-]

Symbol	Description	Units
ϵ	Turbulent dissipation or Dissipation rate	$[m^2 \cdot s^{-3}]$
η	Kolmogorov length scale	[-]
η_p	Passability coefficient	[m]
γ	Experimentally determined additional mass	[-]
κ	Von Kármán constant	[-]
λ	Roughness density	[-]
μ	Fluid viscosity	$[Kg \cdot s^{-1}]$
μ_e	Effective viscosity	$[Kg \cdot s^{-1}]$
$\hat{\mu}$	Viscosity ratio	$[Kg \cdot s^{-1}]$
ν	Fluid kinematic viscosity	$[m^2 \cdot s^{-1}]$
ν_t	Turbulence eddy viscosity	[-]
ω	Dissipation frequency or Specific dissipation rate	$[s^{-1}]$
Ω_1	Stream-wise vorticity	$[s^{-1}]$
ϕ	Porosity	[-]
φ	Solid Volume Fraction	[-]
ψ	Sphericity/Shape factor	[-]
ρ	Fluid density	$[Kg \cdot m^{-3}]$
σ_ϵ	$k - \epsilon$ turbulence model empirical constant	[-]
σ_ω	$k - \omega$ turbulence model empirical constant	[-]

Symbol	Description	Units
σ_k	Turbulent Schmidt number	[-]
τ	Characteristic length	[-]
τ_a	Apparent shear stress	[N·m^{-2}]
τ_t	Reynolds number transition constant	[-]
τ_{zu}	Vertical shear stress	[Pa]
θ	Bed slope	[-]

Chapter 1

Introduction

"Essentially, all models are wrong, but some are useful."
(Box and Draper, 1987)

1.1 Background and Motivation

Floods are one of the costliest natural disasters to which mankind is subject to. The study of anthropomorphic climate change and its effects make the study of flooding phenomena with the aid of Computational Fluid Dynamics tools ever more pertinent. "Floods have a major (defining) impact on floodplains and have significant socio-economic importance. The relatively flat, generally fertile, land with an adjacent water supply has attracted a large proportion of the world's human population to dwell on floodplains at the mercy of the hazards of major flooding, landslides and mudflows" (Marriott, 1999).

According to Terrier (2010) "flood disasters are responsible for approximately a third of the financial losses due to natural disasters throughout the world and account for more than half of the fatalities". He also cites a study on the trends of such disaster occurrences which demonstrate that these figures have been increasing significantly in recent years, making the point that this rise is partly to blame on the twentieth century engineering perspective of alleviating these phenomena by way of hard engineering solutions in the form of embankments, channel straightening or detention reservoirs. "However, such methods often failed to fulfil their objectives. Floodplains, which had been developed, continued to flood in spite of costly flood alleviation schemes", prompting advocacy of a more open approach to flood control focusing on the Main Channel (MC) - Flood Plain (FP) ensemble rather than solely the MC.

This new approach stemmed from the recognition and promotion of the vital role of floodplains in flood alleviation strategies. "For flood engineers, a prerequisite to applying

this policy is a sound understanding of the hydrodynamic processes that link a floodplain to its channel" (Terrier, 2010).

Compound channel flow is a complex phenomenon where the interaction between the MC and FP generates a complicated flow structure. "In practice, the modelling of such typically three-dimensional flows structures, for example for design purposes, usually has to be simplified" (Terrier, 2010), not only in terms of its overall geometry but in terms of other properties which have a critical impact on flow properties.

The presence of vegetation on the floodplain, traditionally regarded by flood engineers as a problem which hinders flow capacity, riparian vegetation is now recognised as an integral part of the solution given its proven ecological role, thus the need to accurately numerically model its effect on the aforementioned flow structures.

The effect of submerged vegetation in both simple and compound-channel flow has been the topic of investigation for quite some time, with numerous experimental studies providing valuable data for the development and refinement of numeric algorithms that are cost effective by being both fastidious and swift on a practical engineering time scale.

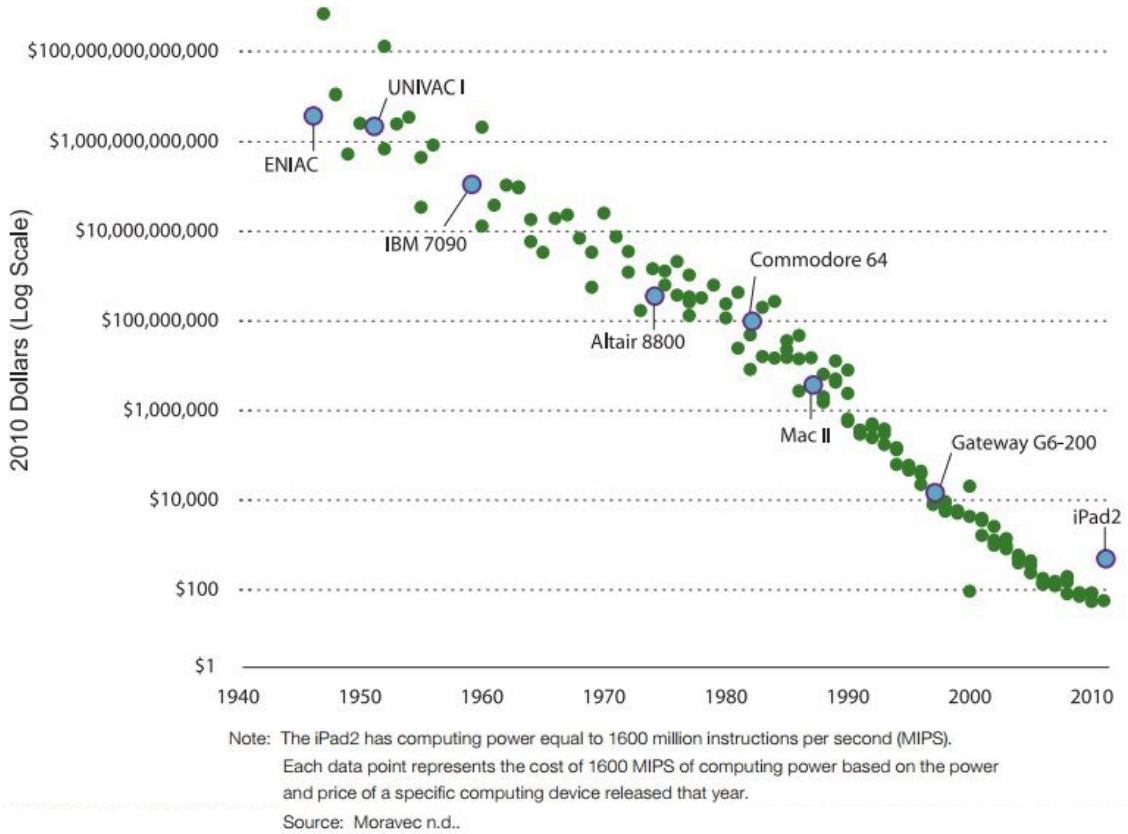

Figure 1.1: Cost of computing power equal to an iPad2. Adapted from The Hamilton Project (2011).

In the past six decades computational power and cost have taken on unprecedented diverging paths, with the former having grown by a trillion fold (Experts Exchange, 2015) while the latter has taken the opposite trajectory as exemplified by The Hamilton Project

(2011) (Figure 1.1). This remarkable diverging trend has made computational power, previously unattainable but to the wealthiest of governments, now readily available to the regular end user, and more so to financially limited research institutions and businesses.

Mathematical models which had been contemplated more than a century ago became useful with computers that could now put them into practice, and the available processing power could be further optimised by deliberate simplifications to applied models. However, these simplifications need to be validated given their often limited contextual applicability, so as to ensure that the results they produce are not only mathematically sound, but truly informative in regards to real world phenomena.

Another development that has aided in the rapid development of CFD solutions has been the advent of the *open-source* movement which re-established the academic principles of source code sharing initially present in software development, which grew out of favour as computer programs became more complex and were turned into a commodity. The establishment of the *GNU Project* (GNU's Not Unix (GNU) being a recursive acronym), first announced on September 27, 1983 by Richard Stallman at MIT, planted the seed for the *open-source* software movement, which was essentially a splinter group from the *free-software* movement established by Stallman (Stallman, 2016). "Free" not as in "free of charge", but as in freedom to run the software study it, modify it and share it. As Stallman (2016) himself puts it, "in practice, open source stands for criteria a little looser than those of free software. As far as we know, all existing released free software source code would qualify as open source. Nearly all open source software is free software, but there are exceptions". Given the often commercial applications and customizations of the OpenFOAM (CFD Direct, 2017) toolbox used and referred to in this thesis work, the *open-source* moniker will hence be used. Much like the mathematical models previously mentioned, so too these tools need validation for them to be applicable to real world situations.

1.2 Objectives and Methodology

The main objective of this thesis is to evaluate the use of the *open-source* CFD toolbox OpenFOAM in the study of vegetated open-channel flow with a porous media analogue to the rigid submerged vegetation. The use of porous media as an analogue to vegetation patches is not new, although its use has been typically used to simulate the effect of forest canopies on atmospheric boundary flow (Lemos, 2006; Peralta et al., 2014). Flows of the type which are the focus of this study, in which "a macroscopic interface exists between a porous media and a clear fluid, the configuration so formed is called a *hybrid medium*" (Lemos, 2006).

Typically, the effect of submerged vegetation on open-channel flow has been accounted for by a drag coefficient which has to be calibrated on a case by case basis (Brito et al., 2016; Chen et al., 2015; Dijkstra and Uittenbogaard, 2010; Hu et al., 2012; Sonnenwald

et al., 2016; Uittenbogaard, 2003), a method which can be heavily reliant on assumptions which affect the validity of the results if not backed up by experience in the field.

In this thesis we start out by evaluating the performance of the porousSimpleFOAM solver from the OpenFOAM toolbox in conjunction with an added turbulence model by Jeyapaul (2015) and Yogesh (2017) on a rectangular compound channel flow case by Filonovich (2015), then trying to partially replicate the numerical study by Brito et al. (2016) which made use of a commercial software solution, both for the good results that it was able to achieve and as a stress test due to the complexities inherent in trapezoidal compound open-channel flow, as detailed in Filonovich (2015), and summed up in 2.5.3 as well as Brito et al. (2016).

Finally, further numerical simulations are conducted based on select parts of the experimental work of Lopez and Garcia (1997) and Nezu and Sanjou (2008) on rectangular open-channel flow, and comparison not only with that experimental, but also numerical work.

As mentioned above, the *open-source* toolbox OpenFOAM will be used, in particular the porousSimpleFOAM solver which, as the name implies, is a SIMPLE algorithm based solver for single-phase, steady-state, incompressible fluid turbulent flows with explicit or implicit porosity treatment.

1.3 Thesis Outline

The present work is divided into five chapters and one appendix. Chapter 1 introduces the reader to the studied topic, giving a background that motivated this study, stating the main objectives and a brief description of the methodology used to accomplish them, and presenting the outline of the thesis.

In Chapter 2 a brief review of fundamental theoretical concepts required to understand the phenomena involved in submerged vegetated flow and how it's typically modelled. Then there's an introduction to flow in porous media, how porosity is modelled and how to apply existing models to submerged vegetation. A brief overview of turbulence modelling and introduction to the turbulence models used in this work is presented and an abridged description the main aspects on numerical modelling of rectangular and trapezoidal compound channel flows is presented. This later section aims to illustrate the turbulent field in compound channel flows and the different numerical approaches used previously by other authors in their simulations.

Chapter 3 introduces the OpenFOAM CFD toolbox, structure of the CFD package, and the algorithms and numerical techniques used in this study. This chapter also presents the importance of convergence and mesh independence study in CFD simulations.

Chapter 4 first presents the experimental and numerical study used for validation and the experimental studies used for the numerical simulations of this work.

Chapter 5 summarizes the results of each individual experiment and resumes the mains conclusions and findings of this thesis, and suggests several approaches for future

work.

Appendix A should be considered an extension of chapter two, with additional theoretical concepts. These are basic concepts about submerged flexible vegetation, additional formulation of porous media and further considerations on the Reynolds number (Re) in porous media flow.

Chapter 2

Theoretical Framework

2.1 Introduction

The main focus of this thesis is the validation of the OpenFOAM toolbox for the study of submerged vegetated flows with the use of a porous media analogue. In order to properly set-up the numerical case studies and then evaluate their results, it is necessary to comprehend the complexities of submerged vegetated flows, porous and hybrid media flow, turbulence modelling and vegetated open-channel flows, the latter by focusing first on cases non vegetated flow of various complexities, and then taking into account the effect of the introduction of submerged vegetation to these types of flow.

There have been numerous studies focused on the impact of submerged vegetation on simple and compound channel flows. These studies offer an abundance of experimental and numerical results (from commercial codes) to which one can compare and adequately validate untested codes.

However, the use of a porous media analogue for dense submerged vegetation has not yet become a commonly adopted "tried and tested" approach, although the few studies that do make use of this technique show it to be a promising technique.

This Chapter is divided into the reviews of the following subjects which are relevant to the validating of OpenFOAM for the study of these types of flow:

- Section 2.2 presents a definition of submerged vegetated flow, how the vegetation is typically characterized, modelled and the impact that it has on the fluid flow.
- Section 2.3 describes the parameters and formulation of steady state, single-phase, incompressible porous media flow, how to integrate the vegetation parameters described in the previous section into the classic Darcy-Forchheimer model, and the particularities of hybrid media flow.

- Section 2.4 introduces basic concepts in turbulence modelling with basic formulation of the prevalent two-equation models and brief descriptions of more robust models able to account for the flow structures in open channel flow which were used to conduct both the studies in the bibliography as well as in this work.

- Finally, Section 2.5 summarizes the flow characteristics of open channel flow, both simple and vegetated, and their respective numerical simulation research.

2.2 Basic concepts in submerged vegetated flow

The presence of submerged vegetation (i.e., rooted vegetation with a vertical extent less than the water depth) in floodplains is common in flood situations. In order to adequately model the effects of submerged vegetation on open compound and/or rectangular channel flow by means of a porous medium, its necessary to first understand both how to characterize the vegetation at hand, and how its experimental real flow is affected so as to assess the validity of its numerical study.

Brito et al. (2016) rely on Nepf (2012b) and Nepf (2012a) description and characterisation of vegetation parameters to characterize the geometric scales used to build up the porous media analogue (see Section 2.3). What follows is a description of the characteristics of vegetated flow, pertaining to the topic at hand, based on Nepf (2012b) and Nepf (2012a) (original sources omitted), and complemented by additional sources.

As mentioned in the Nepf (2012b), "the presence of vegetation alters the velocity field across several scales, ranging from individual branches and blades on a single plant to the community of plants, called the meadow or canopy".

Although there are many aspect pertaining to submerged canopy flow which are adapted from terrestrial canopy flow (Nepf, 2012b), "unlike terrestrial canopies, aquatic canopies can occupy all or a large fraction of the flow depth such that the dynamic impact of the canopy is felt over the entire flow domain". (Nepf, 2012b)'s review focused on the fully developed flow structure over and through long canopies, of which this study is only concerned with the submerged kind.

2.2.1 Geometric scales

The canopy geometry is defined by the scale of its individual elements, namely the individual stems and blades and the number of these elements per bed area. The frontal area per canopy volume a (known as the leaf area index in terrestrial canopy literature) is defined as follows:

$$a = \frac{d}{\Delta S^2} \qquad [\mathrm{m}^{-1}] \tag{2.1}$$

where d is a characteristic diameter or width of the canopy elements, and ΔS the average spacing between those elements. A dimensionlless measure of the canopy density

is the frontal area per bed area, λ, known as the roughness density (Nepf, 2012b). For vertically uniform grass height h_v (i.e., vertically uniform a), and $z = 0$ at the bed:

$$\lambda = \int_{z=0}^{h_v} \mathrm{a}\, \mathrm{d}z = a h_v \qquad [\text{-}] \tag{2.2}$$

A value of $\lambda > \approx 0.23$ is considered to be a dense vegetation layer (Nepf, 2012a).

Vegetation density can also be be described by the solid volume fraction, φ, occupied by the canopy elements (see Section 2.3.3.2). If the individual elements approximate an individual cylinder such as reed stems, then:

$$\varphi \approx \frac{\pi a d_v}{4} \qquad [\text{-}] \tag{2.3}$$

If the morphology of the elements is strap like, such as sea grasses, then:

$$\varphi = \frac{d b}{\Delta S^2} = a b \qquad [\text{-}] \tag{2.4}$$

where d is the blade width and b the blade thickness (Nepf, 2012b).

"Aquatic canopies exhibit a wide range of geometry. marsh grasses are relatively sparse with $d = 0.1$ to $1\ cm$, $[\varphi] = 0.001$ to 0.1, and $a = 0.01$ to $0.07\ cm^{-1}$ (...). Mangroves are among the densest canopies, with $[\varphi]$ as high as 0.45, mean trunk diameters of 4 to $9\ cm$, and a up to $0.2\ cm^{-1}$ (...). Seagrasses have $a = 0.01$ to $1\ cm^{-1}$ and $[\varphi] = 0.01$ to 0.1 (...). Emergent plants tend to have rounded stems for higher stiffness, and submerged grasses tend to have a blade geometry in which the width (0.3 to $1\ cm$) is larger than the thickness ($\approx 0.1\ cm$), in which case d is the blade width" (Nepf, 2012b).

2.2.2 Momentum Scales

According to Nepf (2012b), "within a canopy, flow is forced to move around each branch or blade so that the velocity field is spatially heterogeneous at the scale of these elements. A double-averaging method is used to remove the element-scale spatial heterogeneity, in addition to the more common temporal averaging (...). We let the coordinates x and z be parallel and normal to the local mean bed slope, with $z = 0$ at the bed and positive away from the bed. The velocity vector $\mathbf{u} = (u, v, w)$ corresponds to the coordinates (x, y, z), respectively, The instantaneous velocity and pressure p fields are first decomposed into a time averaged (overbar) and deviations from the time average (single prime). The time-averaged quantities are further decomposed into a spatial mean (angle bracket) and deviations from the spatial mean (double prime). The spatial averaging volume is thin in the vertical direction, to preserve vertical variation in the canopy density, and large enough in the horizontal plane to include several stems ($> \Delta S$).

Using the double-averaging method, the streamwise momentum equation becomes":

$$\frac{D\langle\overline{u}\rangle}{Dt} = g\sin\theta - \frac{1}{\rho}\frac{\partial\langle\overline{p}\rangle}{\partial x} - \underbrace{\frac{\partial}{\partial z}\langle\overline{u'w'}\rangle}_{(i)} - \underbrace{\frac{\partial}{\partial z}\langle\overline{u}''\overline{w}''\rangle}_{(ii)} + \underbrace{\nu\frac{\partial^2\langle\overline{u}\rangle}{\partial z^2}}_{(iii)} - D_V \tag{2.5}$$

"Here ρ is the water density, ν the kinematic viscosity, θ is the bed slope, and g is the gravitational acceleration [(see Figure 2.1)]. Term i is the spatial average of the Reynolds stress. Term ii, called the dispersive stress, is the momentum flux associated with spatial correlations in the time-averaged velocity field [which has been shown to be] less than 10% of the Reynolds stress (term i) for [$\lambda > 0.1$]. Term iii is the viscous stress associated with the spatial variation in $\langle \mathbf{u} \rangle$ [(see Section 2.4 for detailed description of these terms)]. The final term, D_V, is the spatially averaged drag associated with the canopy elements, which is often represented by a quadratic drag law:

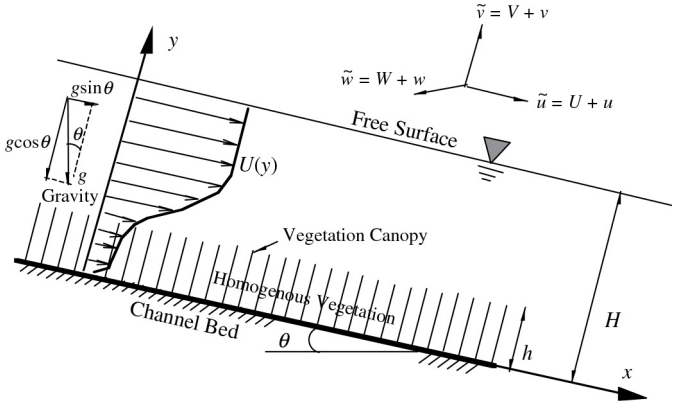

Figure 2.1: 2D vegetated canopy open-channel flows and coordinate system. Adapted from Nezu and Sanjou (2008).

$$D_V = \frac{1}{2}\frac{C_D a}{1-\phi}\langle \overline{u} \rangle |\langle \overline{u} \rangle| \qquad [\text{-}] \tag{2.6}$$

where C_D is the canopy drag coefficient. Because the drag acts on the fluid within the canopy, which occupies only $(1-\phi)$ of the total volume, the drag is divided by the factor $(1-\phi)$. The canopy drag length scale, L_c, is defined from the quadratic law, i.e., based on the dimensional reasoning $D_V = \langle \overline{u} \rangle^2 / L_c$ (...). From Equation [2.6],

$$L_c = \frac{2(1-\phi)}{C_D a} \qquad [\text{m}] \tag{2.7}$$

This represents the length scale over which the mean and turbulent flow components adjust to canopy drag. Because most aquatic canopies have high porosity ($\phi < 0.1$), this scale is commonly approximated by $(C_D a)^{-1}$.

The drag coefficient, C_D, is affected by the canopy density, a; the element Reynolds number, $Re_d = \langle \overline{u} \rangle d/\nu$ [(see Sections 2.3.3.5 and A.3)]; and the morphology of the individual canopy elements. (...). The Darcy-Forchheimer equation [(see Section 2.3.4.2)] has also been used to described drag in wetlands (...) and coral canopies (...). For flexible vegetation, the posture of the bed is affected by the flow speed, a phenomenon called reconfiguration. As velocity increases, the blades are pushed over into more streamlined positions so that the drag force increases more slowly with increasing velocity than predicted by the quadratic drag law. The impact of a changing plant shape on the drag

force has been represented by altering the exponent in the drag law, while holding a, the frontal area, constant at the undisturbed (no flow) value, a_0. (...) In practice, it is difficult to characterize the frontal area a for real plants, which has led to contradictory results in the dependency of drag on velocity" (Nepf, 2012b).

Equation 2.5 is also know as the VARANS equation (Higuera Caubilla, 2015; Marques, 2015), which determines the average flow in a porous medium (such as a submerged canopy) without taking account the exact direction of the flow, as illustrated in Figure 2.2.

In Pedras and Lemos (2001), it is shown that for the macroscopic momentum equation the order of integration (time average and volume average) "is immaterial in regard to the final expression obtained. Also, the TKE resulting from application of the two averaging operators, following both orders of integration, are different". This work and it sources (Gray and Lee, 1977; Slattery, 1967; Whitaker, 1969; Whitaker, 1999) should be consulted for a more in-depth understanding of the application of the volumetric operator. In regards to the time-averaging operator, which is used when turbulence effects are of concern, see section 2.4.

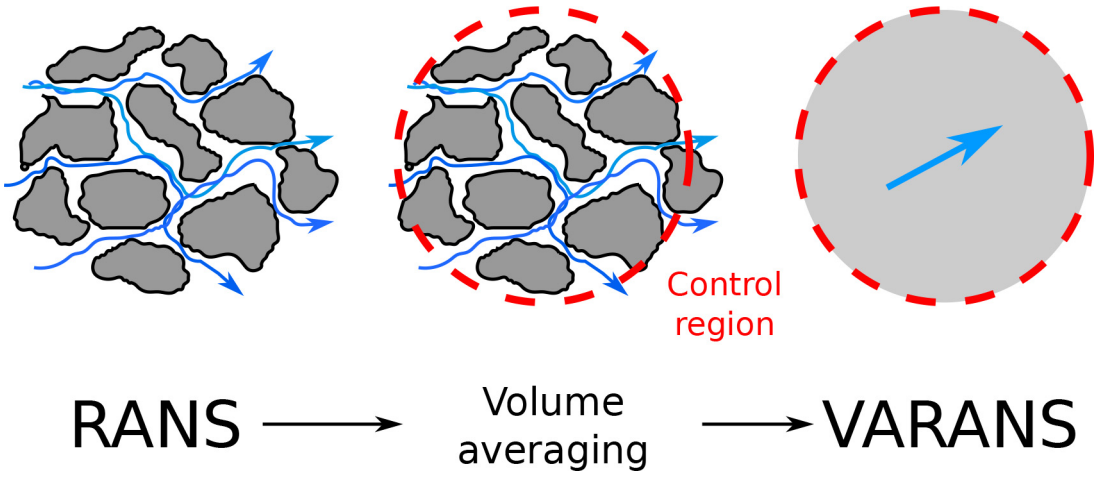

Figure 2.2: Representation of fundamental VARANS principle. Adapted from Higuera Caubilla (2015).

For an application of the VARANS equations to submerged vegetated patches in OpenFOAM consult Chen et al. (2015), where models for the drag (or sink) term by Pedras and Lemos (2001) and Uittenbogaard (2003) are compared.

2.2.3 Submerged Canopies

"The velocity within a submerged canopy has a range of behavior depending on the relative depth of submergence, defined as the ratio of flow depth, H, to canopy height, h [(see Figure 2.4b)]. The flow within the canopy is driven by the turbulent stress at the top of the canopy as well as by the gradients of pressure and gravitational potential

(bed slope). The relative importance of these driving forces varies with the depth of submergence (Nepf, 2000):

$$\frac{turbulent\ stress}{pressure\ gradient} \sim \frac{H}{h} - 1 \qquad [-] \tag{2.8}$$

Three classes of canopy flow can be defined from Equation 2.8: deeply submerged or unconfined ($H/h > 10$), shallow submergence ($H/h < 5$), and emergent ($H/h = 1$). A great deal is known about unconfined canopy flow based on work in terrestrial canopies(...). When unconfined, the flow within a canopy is driven by the turbulent stress at the top of the canopy, i.e., by the vertical turbulent transport of momentum from the overflow, with negligible contribution from the pressure gradients. The terrestrial canopy model can be applied to aquatic canopies that are deeply submerged. However, because of the limitation of light penetration, most submerged aquatic canopies occur in the range of shallow submergence $H/h < 5$ (...), for which both turbulent stress and potential gradients are important in driving flow in the canopy. For emergent conditions ($H/h = 1$), flow is driven by the potential gradients, (...).

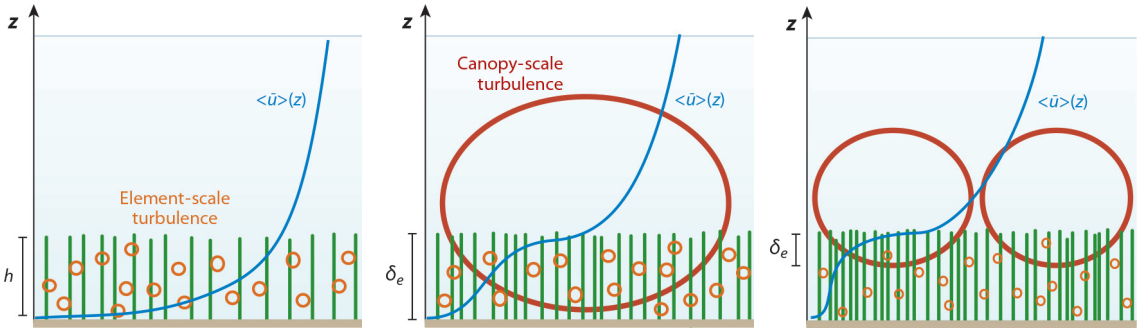

(a) Sparse canopy ($\lambda \ll 0.1$) (b) Transitional canopy ($\lambda \approx 0.1$) (c) Dense canopy ($\lambda \gg 0.1$)

Figure 2.3: Vertical (z) profile of longitudinal velocity and dominant turbulent scale for a sparse (a), transitional (b) and dense (c) canopies, where h is the submerged canopy height and δ_e is the vortice fixed penetration length into the canopy. Adapted from Nepf (2012b).

For a submerged canopy, there are two limits of behaviour, depending on the relative importance of the bed drag and the canopy drag. If the canopy drag is small compared with the bed drag, then the velocity follows a turbulent boundary profile, with the vegetation contributing to the bed roughness (sparse canopy; Figure 2.3a). If the canopy drag is large compared to the bed drag, the discontinuity in drag that occurs at the top of the canopy ($z = h$) generates a region of shear resembling a free shear layer with an inflection point near the top of the canopy (dense canopy, Figure 2.3b,c)" (Nepf, 2012b). Nepf (2012b) also states, based on his sources, that the transition between the sparse and dense regimes occurs at the roughness density $C_D\lambda = ah = 0.1$, C_D being the canopy drag coefficient, with one study showing it be as high as $C_D\lambda = 0.15$. "On the basis of measured velocity profiles in aquatic systems (...), the profile exhibits a boundary layer form with

no inflection point if $C_D ah < 0.04$. A pronounced inflection point appears at the top of the canopy for $C_D ah > 0.1$. Because $C_D \approx 1$ in most of the studies considered, these limits are consistent with the scaling and numerical estimates given above" (Nepf, 2012b). He does stress that his review focuses only on unidirectional flow, and that in flow conditions dominated by waves the canopy drag may have little impact on induced wave velocity, a topic which he further elaborates on in his paper.

Focusing on the dense canopy conditions ($\lambda > 0.1$) there is a demonstrated similarity between canopy sheer layers and free shear layers. "In a free shear layer, the velocity profile contains an inflection point, which triggers a flow instability that in turn leads to the generation of Kelvin-Helmholtz vortices (...). These structures dominate the transfer of momentum between the high speed and low-speed streams, and their size sets the length scale of the shear layer. For dense submerged canopies ($\lambda > 0.1$), the momentum absorption by the canopy is sufficient to produce an inflection point in the velocity profile, which, as in free shear layers, leads to the generation of Kelvin-Hulmholtz vortices (Figure 2.3b,c). These vortices are called canopy-scale turbulence to distinguish it from the much larger boundary-layer turbulence, which may form above a deeply submerged or unconfined canopy, and the much smaller stem-scale turbulence.

Over a deeply submerged (or terrestrial) canopy ($H/h > 10$), the canopy scale vortices are highly three dimensional owing to their interaction with larger boundary-layer turbulence, which stretches the canopy-scale vortices, enhancing secondary instabilities (...). However, with shallow submergence ($H/h \leq 5$), which is common in aquatic systems, larger-scale boundary-layer turbulence is not present, and the canopy-scale vortices dominate the turbulence field, both within and above the canopy (...). For shallow submergence, the canopy scale turbulence is also more coherent (less than three dimensional) than that observed with deeply submerged (or terrestrial) conditions. However, in both cases, the canopy style vortices dominate the vertical transport at the canopy interface (...).

In a free shear layer, the vortices grow continually downstream, predominantly through vortex pairing (...). In canopy shear layers, however, the vortices reach a fixed scale and a fixed penetration into the canopy (δ_e in Figure 2.3b,c) at a short distance from the canopy's leading edge (...). On the basis of measurments with a flexible model of the seagrass *Z. marina* ($a = 5.7\ m^{-1}$), a fixed shear layer scale is reached at a distance of $10h$ from the leading edge of the meadow (...). The fixed vortex and shear-layer scale is reached when the shear production that feeds energy into the canopy-scale vortices is balanced by dissipation by canopy drag. This energy balance predicts the following length scale, which has been verified by laboratory observations (...)" (Nepf, 2012b):

$$\delta_e = \frac{0.23 \pm 0.6}{C_D a} \qquad [\text{-}] \tag{2.9}$$

where C_D is the Canopy drag coefficient. As mentioned previously a factor of $C_D \lambda \geq 0.1$ is required to produce shear layer vortices, so Equation 2.9 applies only to those

canopies. "In the range $C_D\lambda = [0.1, 0.23]$, the shear layer vortices penetrate to the bed, $\delta_e = h$, creating a highly turbulent condition over the entire canopy height (Figure [2.3b]). At higher values of $C_D\lambda$, the canopy scale vortices do not penetrate to the bed, $\delta_e < h$ (Figure 2.3c).

The scaling $\delta_e \sim a^{-1}$ has been observed in flows near porous layers over a wide range of physical scales, from granular beds to terrestrial forests and urban canopies (...). However, the scale relation must brake down when $(C_D a)^{-1}$ approaches the scale of the canopy elements , d, because a is defined only as an average over multiple elements. For rigid cylinders, when $(C_D a)^{-1}$ is less than $2d$, the penetration scale transitions to a constant $\delta_e \approx 2d$ (...). The depth of submergence, H/h, can also affect the penetration length scale. For $H/h < 2$, δ_e is diminished from Equation [2.9], as interaction with the water surface diminishes the scale and the strength of the vortices.

The penetration length, δ_e, segregates the canopy into an upper layer of strong turbulence and rapid renewal and a lower layer of weak turbulence and slow renewal (...). Flushing of the upper canopy is enhanced by the canopy-scale vortices that penetrate this region (Figure [2.3c]). In contrast, turbulence in the lower canopy ($z < h - \delta_e$) is generated in stem wakes and has a significantly smaller scale, set by the stem diameters and spacing. Canopies for which $\delta_e/h < 1$ (Figure [2.3c]) shield the bed from strong turbulence and turbulent stress. Because turbulence near the bed plays a role in resuspension, these dense canopies are expected to reduce resuspension and trap sediment. (...). We note that the transition in near-bed turbulence and resuspension does not occur abruptly at $C_D\lambda = 0.23$ but occurs gradually with increasing $C_D\lambda$ above this value, as the canopy scale vortices are progressively pushed further from the bed. Because of the reduced near-bed turbulence, dense canopies can promote sediment retention. In sandy regions, which tend to be nutrient poor, the preferential retention of fines and organic material (i.e., muddification) enhances the supply of nutrients to the canopy so that dense canopies provide a positive feedback to canopy health in sandy regions. In contrast, in regions with muddy substrate, which is more susceptible to anoxia [(lack of oxygen)], sparse meadows ($C_D\lambda \leq 0.23$) may be more successful because the enhanced near-bed turbulence removes fines, leading to a sandier substrate that is less prone to anoxia" (Nepf, 2012b).

"In compound open-channel flows H/h (see Figure 2.4a) is a function of the relative depth h_r, defined as the relation between FP flow depth h_{FP} and MC flow depth h_{MC}" (Brito et al., 2016):

$$h_r = \frac{h_{FP}}{h_{MC}} \qquad [-] \tag{2.10}$$

2.2.4 Mean Velocity Profile

Based on Nepf (2012b)'s description of vegetated flow so far, "sufficiently far above a submerged canopy ($z > 2h$), the velocity profile is logarithmic (...):

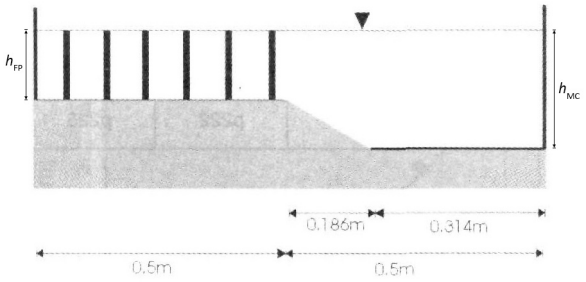

(a) Compound open-channel with Main Channel and Flood Plain.

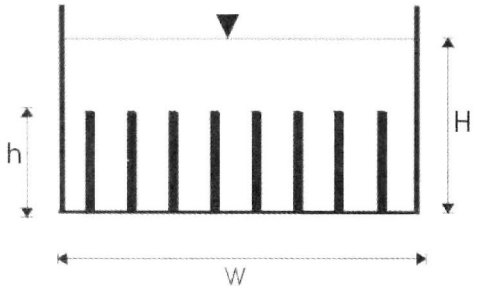

(b) Rectangular open-channel flow.

Figure 2.4: Cross-sections of open-channel flow geometries with vegetation. Adapted from Fischer-Antze et al. (2001).

$$\langle \overline{u} \rangle = \frac{u_*}{\kappa} \ln\left(\frac{z - z_m}{z_0}\right) \qquad [\mathrm{m{\cdot}s^{-1}}] \tag{2.11}$$

with $\kappa = 0.4$ (von Kármán constant). The horizontal average (in angled brackets) is not strictly needed above the canopy but is retained for consistency with the equations within the canopy. The friction velocity, u_*, is related to the Reynolds stress at the top of the canopy, ${u_*}^2 = \langle \overline{u'w'} \rangle_h$. The parameters z_m and z_0 are the displacement and roughness heights, respectively, both of which depend on the canopy roughness density, λ. On the basis of studies with both model and real vegetation, a simple estimate for friction velocity is":

$$u_* = [gS(H - h)]^{0.5} \qquad [\mathrm{m{\cdot}s^{-1}}] \tag{2.12}$$

with S defined as:

$$S = \frac{\partial H}{\partial x} + \sin\theta \qquad [\mathrm{m}] \tag{2.13}$$

"If the vegetation is flexible, then h is the mean deflected height of the canopy (...). However, if the depth of submergence is small, compared to the displacement height, the following estimator is more accurate":

$$u_* = [gS(H - z_m)]^{0.5} \qquad [\mathrm{m{\cdot}s^{-1}}] \tag{2.14}$$

The "penetration length scale, δ_e [(Figure 2.3)], describes the distance over which turbulent stress penetrates the canopy from above. Similarly, the displacement height is the centroid of momentum penetration into the canopy (...). This similarly suggests the physically intuitive scaling":

$$\frac{z_m}{h} \approx 1 - \frac{1}{2}\frac{\delta_e}{h} = 1 - \frac{0.1}{C_D \lambda} \qquad [-] \tag{2.15}$$

"which has been confirmed for $\lambda \approx [0.2, 0.3]$ (...). For $\lambda > 1$, the displacement thickness tends towards $z_m \approx h$, indicating that essentially the entire canopy is cut off from the overflow. In addition, z_m goes to zero at $\lambda = 0.1$. When $z_m = 0$, the velocity profile has no inflection point (Figure [2.3a), consistent with the observation that $\lambda > 0.1$ is required to produce an inflection point in measured velocity profiles (Figure [2.3b,c]).

The dependency of the roughness height, z_0, on the canopy density, λ, differs significantly above and below the threshold of $\lambda = 0.1$ (...). In the sparse-canopy range ($\lambda < 0.1$), the roughness height increases with increasing λ. In sparse canopies, the flow penetrates the full canopy so that z_0 is proportional to the drag imparted by the full canopy, $C_D\lambda$, i.e., $z_0/h \sim C_D\lambda$. In contrast, for dense canopies ($\lambda > 0.1$), the roughness height decreases with increasing λ. The effective heigh of the canopy, as seen by the overflow, is the penetration scale, δ_e. The roughness height depends on this effective height, rather than canopy height, so that $z_0 \sim \delta_e \sim a^{-1}$. (...).

The logarithmic profile form is based on equilibrium turbulence such that dissipation and production are locally in balance (...). Largely because of the vertical transport provided by the shear layer structures, this condition is not met for some distance above the canopy, called the roughness sublayer. For very shallow submergence, $H/h \leq 1.5$, the roughness sublayer extends to the surface, and a logarithmic structure is not observed above the canopy".

Nepf (2012b) goes on to describe the velocity profile within the bed so as to obtain a reasonably accurate full velocity profile by combining the models for above-canopy and in-canopy profiles. This is illustrated in Figure 2.5 which contains the measured velocity (*dots*) and predicted velocity (*solid line*) with confidence line (*dashed lines*) from Ghisalberti, 2005. Parameters are: $H = 46.7\ cm$, $h = 13.9\ cm$, $S = 2.5 \times 10^{-5}$, $a = 0.034\ cm^{-1}$, and $C_D = 0.77$ (measured). Above the meadow, the velocity is predicted from the logarithmic profile (Equation 2.11), with friction velocity as per Equation 2.12, z_m as per Equation 2.15, and $z_0 = (0.04 \pm 0.02)a^{-1}$. For the equations used to determine the in-canopy velocity profile please consult the source.

Given that the use of a porous medium as an analogue to a dense submerged canopy nullifies any study of a valid in-canopy velocity profile (Marques, 2015; Sonnenwald et al., 2016), the details of how to model it will not be discussed here.

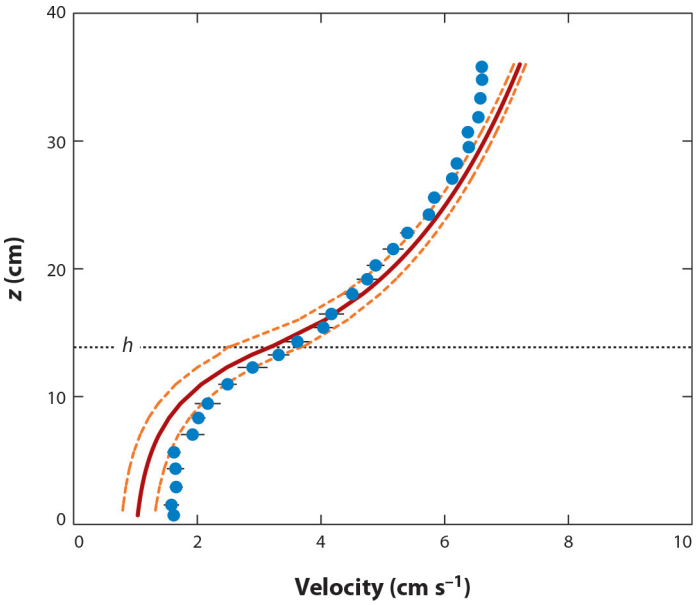

Figure 2.5: Measured velocity (*dots*) and predicted velocity (*solid line*) with confidence line (*dashed lines*) from Ghisalberti, 2005. Adapted from Nepf (2012b).

2.3 Basic concepts in porous media flow

A porous medium can be described as a solid (or solid matrix) with interconnected voids distributed somewhat uniformly throughout the bulk of the body (Jambhekar, 2011; Polezhaev, 2006), of which its main characteristic is *porosity*, ϕ (Equation 2.17).

The use of porous media in CFD goes beyond its initial applicability in describing actual physical porous structures. It extends to other physical structures, which on a physical level, act as a porous medium in the way that these structures might dampen the flow of a given fluid, and even redirect its flow, such as the use of porous media as an analogue for swirl vanes in a gas turbine engine as in Ford et al. (2013).

It is therefore a topic of great interest in various scientific and technical fields, with wide applications in the field of engineering (Jambhekar, 2011; Li and Ma, 2011; Nield and Bejan, 2013) as can be seen in Figure 2.6.

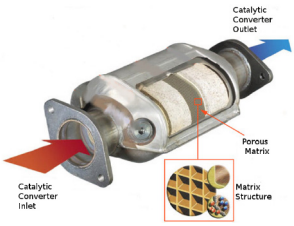

(a) Catalytic converter for automobile exhaust system

(b) Porous heat exchanger for air cooled condensers

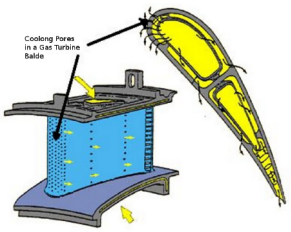

(c) Cooling pores in a gas turbine blade

Figure 2.6: Applications of porous media. Adapted from Jambhekar, 2011.

As stated in chapter 1, this thesis has as its main purpose the validation of the use of a porous medium as a stand-in for a submerged dense vegetative layer, as initially validated by Brito et al. (2016) and more recently Sonnenwald et al. (2016), using the OpenFOAM open-source tool. Although limited (Marques, 2015; Sonnenwald et al., 2016), the use of a porous medium to simulate a vegetative layer provides a more pragmatic and scientific approach to achieving valid numeric simulations of the effects of submerged vegetation (Brito et al., 2016; Sonnenwald et al., 2016), effects which have been traditionally taken into account by introducing an extra sink term into the momentum equations, thus accounting for the additional flow resistance of the submerged vegetation. This term is usually "modelled as a drag force on a rigid obstacle (cylinder/vegetation element) with drag coefficient of an isolated cylinder, accounting for both viscous and form drag arising from the spatial perturbation of velocity and pressure" (Brito et al., 2016). There are similar methods which use more complex turbulence models such as RSM, which are more computationally expensive to run (Cebeci, 2004; Filonovich, 2015; Pope, 2000; Versteeg and Malalasekera, 2007), or which just make use of a bulk drag coefficient. However, these approaches have their own limitations. The method which makes use of a cylinder's drag coefficient, though able to reproduce the flow velocity profiles, disregards eddy-eddy and eddy-cylinder interactions, as well as being unable to properly address the vegetation spatial heterogeneity and requiring a numerical mesh fine enough to account for individual vegetation elements (Brito et al., 2016).

In his Master's thesis, Jambhekar (2011) thoroughly describes the fundamentals of Darcy and non-Darcy (Forchheimer) flow models. What follows is a literature review composed of mainly this source complemented by additional sources. However, some details will be abridged or omitted due to the particular nature of the type of porous media flow which is the scope of this thesis, namely isothermal single-phase steady-state flow in porous media.

2.3.1 Scales - The continuum approach

How one treats the problem of flow through a porous medium is largely dependent on the scale considered. It is only convenient to apply a conventional fluid mechanics approach to the flow phenomenon in the fluid filled spaces if one is looking at a micro-scale or pore-scale, analysing the flow in a particular section of the porous medium. In cases such as those being studied in this thesis, i.e. the macro-scale, such an approach is not feasible due to the complicated flow paths and the need to describe the complex spatial resolution of the porous structure, requiring an excessively refined mesh in order to accurately describe the flow (Jambhekar, 2011).

"The finite scale and engineer would look at is the molecular scale. The continuum mechanics based approach is used for transition from the molecular-scale to the micro-scale. The consideration of a continuum corresponds to replacing the molecular properties by averaged properties over a large number of molecules. (...), the consideration of a

continuum at the macro-scale is a fundamental concept of fluid mechanics" (Jambhekar, 2011).

In Brito et al. (2016), Lemos (2006), and Pedras and Lemos (2001), the continuum approach is adopted by means of a volume averaged approach so as to describe the flow properties on a macro-scale. Figure 2.7 illustrates the different scales involved in the averaging process.

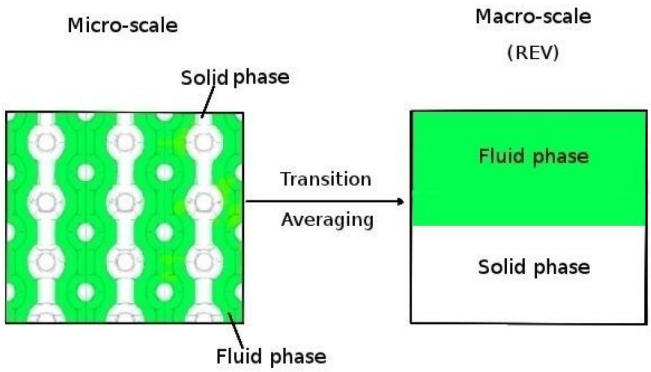

Figure 2.7: Micro-scale to macro-scale transition. Adapted from Jambhekar (2011).

The domain is first analysed at the micro-scale (see Section 2.3.3) and its properties are averaged over a Representative Elementary Volume (REV) "in order to obtain a macro-scale description of the system with effective parameters such as porosity ϕ (...) and intrinsic permeability K" (see Section 2.3.4). "The macro scale is also referred to as the REV-scale. It can be seen from Figure" 2.7 "that at the REV scale, detailed spatial resolution of solid matrix and fluid phase is lost, and effective volume averaged parameters (effective parameters) are available" (Jambhekar, 2011).

The volume averaged quantities need to be independent from the REV-size, so the latter must be properly selected. This is illustrated in Figure 2.8, where it's shown that the selected REV should be smaller than the flow domain and larger than a single pore in the porous medium. This is to avoid both oscillations due to existence of inhomogenieties at the micro-scale, and fluctuations caused by macroscopic heterogeneities of the medium (Jambhekar, 2011).

2.3.2 Local equilibrium in porous media

"The local thermodynamic equilibrium in porous media mainly consists of thermal, chemical and mechanical equilibria as follows:

Thermal equilibrium: A system is said to be in local equilibrium, if at any given point of the system all the phases exist at the same temperature T:

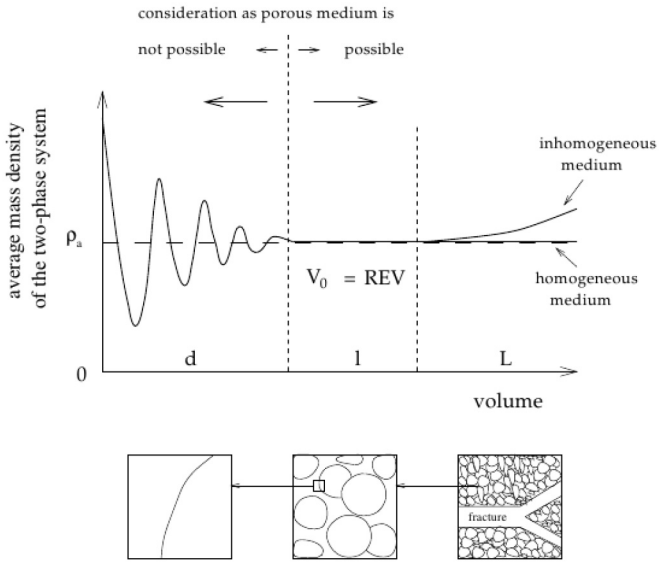

Figure 2.8: Definition of the REV. Adapted from Jambhekar (2011).

$$T = T_S = T_F \qquad [\mathrm{K}] \tag{2.16}$$

Here, T_S and T_F are the temperatures of the solid matrix and fluid phase respectively.

Chemical equilibrium: A system is said to be in chemical equilibrium, if the potential for exchange of chemical components across different phases or within a phase is zero. In other words, there is no exchange of components within a phase or between phases.

Mechanical equilibrium: When multiple fluid phases are present in the system, mechanical equilibrium refers to the existence of equal pressure on either side of the phase boundary (e.g., a lake surface). However, in the context of the porous media flow, one must account for the pressure jump at the fluid phase boundaries due to capillarity *i.e.*, the capillary pressure" (Jambhekar, 2011).

2.3.3 Effective parameters

In order to accurately describe the porous medium and translate the measurements of the REV properties into parameters usable by the numerical simulator, its necessary to accurately define the parameters relevant to the type of flow being studied.

2.3.3.1 Porosity (ϕ)

As first mentioned in the beginning of this Section, porous media consist of a solid (or solid matrix) with interconnected voids distributed somewhat uniformly throughout the bulk of the body. It is defined as the ratio of the volume of pores in an REV to to the volume of the REV (Jambhekar, 2011):

$$\phi = \frac{Volume\ of\ pores\ in\ REV}{Volume\ of\ REV} \qquad [\text{-}] \tag{2.17}$$

As indicated in Equation 2.17, porosity is a dimensionless parameter, and in the current study the solid matrix composed of vegetation elements is assumed to be a rigid structure (Brito et al., 2016; Lopez and Garcia, 1997; Nezu and Sanjou, 2008).

2.3.3.2 Solid volume fraction (φ)

The density of a porous medium can also be described by the solid volume fraction, $\varphi = 1 - \phi$, which in the case of the present work can be calculated as:

$$\varphi = \frac{\pi a d_v}{4} \qquad [\text{-}] \tag{2.18}$$

where d_v is the average diameter of cylinders analogous to the synthetic grass elements used in a given experiment, and a is the frontal area per volume:

$$a = \frac{d_v}{\Delta S^2} \qquad [\mathrm{m}^{-1}] \tag{2.19}$$

2.3.3.3 Porous media comprised of non-spherical particles

"A great number of empirical or semi-empirical models have been developed to predict flow characteriscs in porous media" (Li and Ma, 2011). As described in Section 2.3.4.2, these models are based on Darcy's earliest work which made use of sand columns as a porous medium. The medium then has particles which are approximately spherical, or can be assumed to be as such. For porous media packed with non-spherical elements, which is usually the case in reality (Li and Ma, 2011), an equivalence between spherical and non-spherical particles (e.g., cylinders, hollowspheres, hollow cylinders, or rings), has to be established so as to make use of established models (see Section 2.3.4.2). "Some research works in this aspect showed that much higher pressure drops have been obtained than anticipated from the calculations based on spheres (...). The increase in tortuosity was considered as the reason why non-spherical partical beds generate higher pressure drop". Li and Ma (2011) go on to specify that other parameters such as the dynamic specific surface, i.e., the wetted surface and the form drag were proposed to modify the model while others correlated the Ergun constants (see Section 2.3.4.2) to the shape factors of particular cylinders and rings. "However, all these aditional parameters and approaches are rather vague in physical meaning and hard (if not impossible) to quantify experimentally" (Li and Ma, 2011).

What follows are descriptions of some basic parameters required to take this difference in pressure drop into account while making use of established equations (see Section 2.3.4.2).

Sphericity (ψ) "The constant ψ is the shape factor of the particles (also called sphericity), which is defined as the ratio of the surface area of equivalent-volume sphere to that of the actual particle:

$$\psi = \frac{\text{surface of sphere of equal volume to the particle}}{\text{surface area of the particle}} = \frac{A_{sp}}{A_p} = \frac{\pi^{\frac{1}{3}}(6V_p)^{\frac{2}{3}}}{A_p} \qquad [-] \quad (2.20)$$

where V_p is volume of the particle, A_p the surface area of the particle, and A_{sp} the surface area of the equivalent volume sphere" (Li and Ma, 2011).

Equivalent Diameters of Non-Spherical Particles For a packed bed with spherical particles, the shape factor ψ is taken as unity and the diameter d_{vs} as the actual diameter of the particles. For a bed packed with non spherical particles, the diameter d_{vs} is obtained through the shape factor ψ of the particles (Li and Ma, 2011):

$$d_{vs} = \frac{6V_p}{A_{sp}} = \frac{6V_p}{\psi A_p} \qquad [\text{m}] \quad (2.21)$$

which is also referred to as the volume-surface mean diameter. When we take this term and multiply it by the shape factor ψ defined in Equation 2.20 for non-spherical particles, we obtain the term ψd_{vs} which can be rewritten as follows:

$$\psi d_{vs} = \psi \frac{6V_p}{\psi A_p} = \frac{6V_p}{A_p} = \frac{6}{S_V} = d_{sd} \qquad [\text{m}] \quad (2.22)$$

where S_V is the specific surface area and d_{sd} the Sauter mean diameter which is defined as the diameter of a sphere that has the same ratio of volume to surface area as the particle of interest (Li and Ma, 2011).

In studies prior to Li and Ma (2011) only the Sauter mean diameter was employed in the prediction of the pressure gradient, while the non-sphericity of particles was not explicitly considered, since the Sauter mean diameter emphasizes the importance of specific surface area in particle characterisation, eliminating the shape factor ψ in the expression of ψd_{vs}, as show in Equation 2.22. In their study, Li and Ma (2011) found that the Sauter mean diameter was not sufficient to predict the pressure drop of fluid flow in the packed beds with the non-spherical particles. They then proposed another mean particle diameter, which is called the equivalent particle diameter, being equal to the product of the shape factor and Sauter mean diameter:

$$d_{eq} = \psi d_{sd} \qquad [\text{m}] \quad (2.23)$$

By choosing the equivalent particle diameter and applying it to the modified Ergun equation (see Sections 2.3.3.3 and 2.3.4.2, respectively), Li and Ma (2011) were able to establish a correlation between the numerical results and the corresponding experimental data. "The definition of the equivalent particle diameter has an emphasis on the shape

factor in the friction laws and explicitly reflects a physical mechanism for the contribution of an increased tortuosity to the frictional drag because of the complexity in shapes, especially at turbulent regime" (Li and Ma, 2011).

2.3.3.4 Intrinsic permeability (K)

The ability of a porous medium to allow a fluid to pass through it is referred as its intrinsic permeability (K), a macro-scale property, and is part of the definition of the hydraulic conductivity tensor (K_f). The latter is also a macro-scale property which accounts for the influence of viscosity and adhesion at the soil grain surfaces (Jambhekar, 2011). For a single-phase flow, it's given as:

$$K_f = K\frac{\rho g}{\mu} \qquad [\mathrm{m{\cdot}s^{-1}}] \tag{2.24}$$

where K is the intrinsic permeability tensor, ρ and μ are fluid properties, namely, density and viscosity, respectively, and g is the gravitational acceleration (Jambhekar, 2011). "The intrinsic permeability tensor is a second order tensor with nine components indicating permeabilities in different directions:

$$K = \begin{bmatrix} K_{xx} & K_{xy} & K_{xz} \\ K_{yx} & K_{yy} & K_{yz} \\ K_{zx} & K_{zy} & K_{zz} \end{bmatrix} \qquad [\mathrm{m^2}] \tag{2.25}$$

Intrinsic permeability (K) is only dependent on the porous structure and can be [the] same or different in different directions, depending on whether the porous matrix is isotopic or anisotropic" (Jambhekar, 2011). If it's given a scalar value, then it is to be assumed that the porous medium is isotropic in nature, and its intrinsic permeability and Forchheimer tensor values are the same in every direction (Jambhekar, 2011).

2.3.3.5 Reynolds number (Re)

The Reynolds number in porous media is defined by:

$$Re = \frac{Inertia\ force}{Viscous\ force} = \frac{\rho u_s L}{\mu} \qquad [\text{-}] \tag{2.26}$$

where ρ, $\mathbf{u}_s$ and μ are fluid density, seepage velocity and viscosity, respectively. (Jambhekar, 2011) considers L to be the characteristics length, obtained from the specific interfacial area (S_v), defined as the area of contact between the solid and fluid phase per unit volume.

The Reynolds number in porous media flow is adequately named the pore (or porous) Reynolds number Re_p, based on which (according to Pedras and Lemos (2001)) "the literature recognizes distinct flow regimes, namely: (a) Darcy or creeping flow regime ($Re_p < 1$); (b) Forchheimer flow regime ($1 \sim 10 < Re_p < 150$); (c) post-Forchheimer flow regime (unsteady laminar flow, $150 < Re_p < 300$); (d) fully turbulent flow ($Re_p > 300$). The

mathematical description of the last regime has given rise to interesting discussions in the literature and remains a controversial issue.

For $Re_p < 150$, classical mathematical treatment of flow in porous media (...) invokes the notion of a REV for which balance equations governing momentum, energy and mass transfer are written. Models based on this macroscopic (*volume-averaged*) point of view lose details on the flow pattern inside the REV and, together with ad-hoc information, give results on global flow characteristics.

For high Reynolds numbers ($Re_p > 300$), however, turbulence models presented in the literature follow two different approaches. In the first one (...), governing equations for the mean and turbulent fields are obtained by time averaging the volume-averaged equations. In the second method (...), a volume-average operator is applied to the local time-averaged equation. Or say, in the first case, volume-average is taken first and the time averaging is applied. In the latter method, the order of averaging is reversed. In the literature, these two different approaches lead to different governing equations and, ultimately, to contradicting overall conclusions" (Pedras and Lemos, 2001).

A more comprehensive review of Re in regards to porous medium flow is presented in Appendix A.

2.3.4 Governing equations

By opting for the continuum approach one needs the definition of the laws for conservation of mass, momentum and energy for the study at hand.

2.3.4.1 Mass conservation

The mass conservation equation (or continuity equation) ensures that the net change of mass within a continuum is zero (Jambhekar, 2011; Pope, 2000; Vafai, 2005; Versteeg and Malalasekera, 2007). The conservation of mass for a free flow system is defined as follows:

$$\frac{\partial \rho}{\partial t} + \nabla \cdot (\rho \mathbf{u}) = 0, \tag{2.27}$$

where ρ is the fluid density, t is time, $\mathbf{u}$ is the fluid velocity vector. "The first term on the left hand side is the rate of change in time of the density (mass per unit volume). The second term describes the net flow of mass out of the element across its boundaries and is called the convective term" (Versteeg and Malalasekera, 2007).

Equation 2.27 "indicates that the rate of change of mass per unit control volume, fluxes across the faces of the control volume and the potential sources and sinks must balance" (Jambhekar, 2011). As in Jambhekar's work, porosity is included in Equation 2.27, as the continuity is only considered for the fluid flow through the porous medium:

$$\phi \frac{\partial \rho}{\partial t} + \nabla \cdot (\rho \phi \mathbf{u}) = 0, \tag{2.28}$$

Using the relation between the Darcy/Forchheimer velocity vector $\mathbf{u}_D$ and the seepage velocity vector $\mathbf{u}_s$ given by:

$$\mathbf{u}_s = \frac{\mathbf{u}_D}{\phi} \qquad [\mathrm{m{\cdot}s^{-1}}] \tag{2.29}$$

Equation [2.28] can be rewritten as follows:

$$\phi \frac{\partial \rho}{\partial t} + \nabla \cdot (\rho \mathbf{u}_D) = 0, \tag{2.30}$$

The velocity vector $\mathbf{u}_D$ is referred to both as the Darcy velocity vector and the Forchheimer velocity vector in Sections 2.3.4.2 and 2.3.4.2. It is also mentioned in literature as the superficial velocity (Lemos, 2006; Marques, 2015).

Furthermore, (Marques, 2015) describes the Darcy velocity vector as the average flow velocity in the porous media, not representative of the exact velocity of the fluid coursing through the voids, and defined as a simple algebraic manipulation of Equation 2.29:

$$\mathbf{u}_D = \mathbf{u}_s \times \phi \qquad [\mathrm{m{\cdot}s^{-1}}] \tag{2.31}$$

As Smart (2013) describes it, "Darcy velocity [$\mathbf{u}_D$] is a fictitious velocity since it assumes that flow occurs across the entire cross section of the [porous media]. Flow actually takes place only through interconnected pore channels (voids), at the seepage velocity [$\mathbf{u}_s$]".

Taking into the account the nature of the flow studied in this thesis, i.e., that of an incompressible fluid, a rigid porous medium and no source or sink, Equation 2.30 is reduced to:

$$\nabla \cdot (\mathbf{u}_D) = 0 \tag{2.32}$$

2.3.4.2 Momentum Balance

In this section the momentum balance equations for the macro-scale analysis of fluid flow through proous medium are described. The Darcy law (see Section 2.3.4.2) and the Forchheimer law (see Section 2.3.4.2) are the basis for describing both slow creeping flows and high velocity flows, respectively. "Both the Darcy law and the Forchheimer law are obtained experimentally in order to describe the flow through a porous medium and have become the macro-scale equation of choice in literature. (...), these equations for momentum description allow the decoupling of the continuity and momentum balance" (Jambhekar, 2011).

Darcy Law Henry P.G. Darcy developed what is now known as Darcy's Law in 1856 whilst studying the city of Dijon's water supply system (Moura, 2014). This was the first mathematical expression of fluid flow through porous media, and has thus become the foundations for fluid flow in porous media studies (Lai et al., 2009). Darcy used

sand packs for his steady-state unidirectional flow experiments to show that the potential gradient ($\partial p/\partial L$) could be related to the fluid viscosity (μ) and Darcy velocity $\mathbf{u}_D$ (see equation 2.29) through a permeability constant K (see Section 2.3.3.4):

$$-\frac{\partial p}{\partial x} = \frac{\mu}{K}\mathbf{u}_D \tag{2.33}$$

In his original publication it was expressed in terms of hydraulic head:

$$\mathbf{u}_D = -K_f \cdot \nabla h \qquad [\mathrm{m{\cdot}s^{-1}}] \tag{2.34}$$

"where K_f is the hydraulic conductivity tensor as explained in Section 2.3.3.4 and ∇h is the gradient of the piezometric head h given by:

$$h = \frac{p}{\rho g} + z \qquad [\mathrm{m}] \tag{2.35}$$

where $\frac{p}{\rho g}$ is the pressure head and z is the elevation head" (Jambhekar, 2011). Taking 2.35 into account and substituting in Equation 2.34, Darcy's Law can be re-written as follows:

$$\mathbf{u}_D = -\frac{K}{\mu} \cdot (\nabla p + \rho g \nabla z) \tag{2.36}$$

where ∇p is the applied (or potential) pressure gradient, previously referred to as $\frac{\partial p}{\partial x}$, and as mentioned previously, μ and K are the dynamic viscosity and intrinsic permeability tensor of the porous medium, respectively. Often times the intrinsic permeability tensor is referred to in its inverse form, as the linear coefficient α (Polezhaev, 2006):

$$\alpha = \frac{1}{K} \qquad [\mathrm{m^{-2}}] \tag{2.37}$$

According to Lai et al. (2009), Darcy mentioned in the publication of his work how he had difficulties conducting measurements at higher flow rates due to the demand placed by others on the flow system of the hospital where he was conducting his experiments (Support, 2013). This limited his experimental analysis, and mathematical model, for slow (creeping) flows (see Section 2.3.3.5).

Forchheimer Law It was only in 1901 that Austrian engineer Philipp Forchheimer observed deviations from the linearity from Darcy's Law at high flow rates which Darcy had not been able to observe in his original studies (Lai et al., 2009). Namely, he observed that as the flow velocity increases, the inertial effects start dominating the flow (Jambhekar, 2011). Taking his observations into account, Forchheimer expanded Darcy's linear form into a quadratic flow equation (Lai et al., 2009), Equation 2.38:

$$-\frac{\partial p}{\partial x} = \frac{\mu}{K}\mathbf{u}_D + \beta\rho{\mathbf{u}_D}^2 \tag{2.38}$$

where β $[m^{-1}]$ is the Non-Darcy coefficient (or Forchheimer coefficient).

It is usually also given in its vector form:

$$-\frac{\partial p}{\partial x} = \frac{\mu}{K}\mathbf{u}_D + \beta\rho|\mathbf{u}_D|\mathbf{u}_D \tag{2.39}$$

According to (Jambhekar, 2011), "theoretical evaluation of the Forchheimer coefficient β is cumbersome. Thus, for most practical applications, this parameter is obtained from the best fit to the experimental data".

This is now commonly referred as the Forchheimer equation, and flows for which it is applicable to are called non-Darcy flows. Later on Forchheimer would end up adding an additional cubic term, as per Equation 2.40, as Equation 2.38 still didn't adequately describe his observational data, thus needing the extra cubic term to account for the deviations between his observations and analytical model. This limitation of Forchheimer's model has been noted by other authors, and as led to the development of new models for porous media flow (Jambhekar, 2011; Lai et al., 2009; Moura, 2014).

$$-\frac{\partial p}{\partial x} = \frac{\mu}{K}\mathbf{u}_D + \beta\rho{\mathbf{u}_D}^2 + \gamma\rho{\mathbf{u}_D}^3 \tag{2.40}$$

where γ $[Kg]$ is the experimentally determined additional mass, determined by Van Gent in 1995 as being 0.34 (Marques, 2015).

Figure 2.9 shows how the effects of these discrepancies an have a considerable impact on the assessment of a given porous medium, not only by way of an example where the experimental data deviates from the Forchheimer plot but by also showing that the Darcy coefficient β varies with increased flow rate.

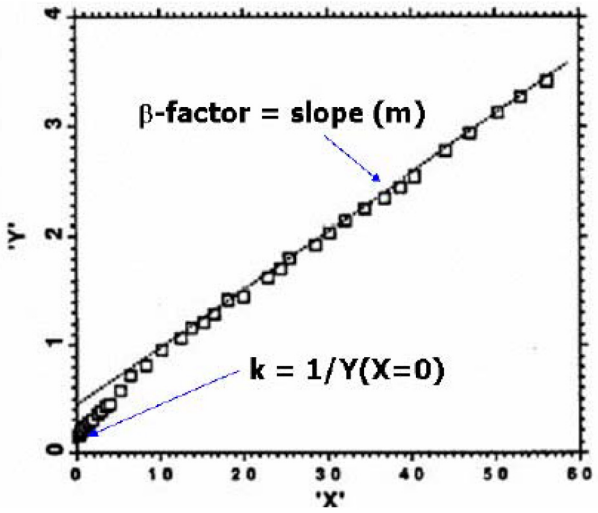

Figure 2.9: Typical Forcheimer plot where β is the slope of the line which intercepts varying value ranges of K. Adapted from Lai et al. (2009).

Ergun equation As mentioned in the Section 2.3.4.2, the non-Darcy coefficient (or Forchheimer coefficient) is difficult to be determined theoretically. Based on his earlier

work with Orgning, the Turkish chemical engineer Sabir Ergun proposed and expression for the Forchheimer coefficient β (Jambhekar, 2011):

$$\beta = \frac{C_E}{\sqrt{K}} \qquad [\mathrm{m}^{-1}] \tag{2.41}$$

"where C_E is called the Ergun constant and it accounts for the inertial (kinetic effects). K is the intrinsic permeability" (see Section 2.3.3.4) (Jambhekar, 2011).

In Li and Ma, 2011, the β is referred to in its inverse form, the passability coefficient η_p, referred to in Jambhekar (2011) as intrinsic passability, defined as the ratio of the square root of intrinsic permeability to the Ergun coefficient C_E:

$$\eta_p = \frac{\sqrt{K}}{C_E} = \frac{1}{\beta} \qquad [\mathrm{m}] \tag{2.42}$$

From Equation 2.41 and Equation 2.39, we get the Ergun equation which is also referred to as the Forchheimer equation with Ergun coefficient (Jambhekar, 2011):

$$-\frac{\partial p}{\partial x} = \frac{\mu}{K}\mathbf{u}_D + \frac{C_E}{\sqrt{K}}\rho|\mathbf{u}_D|\mathbf{u}_D \tag{2.43}$$

"The Ergun coefficient C_E is strongly dependent on the flow regime. For slow flows, C_E is very small. Thus, the second term on the right hand side of" Equation 2.43 "is very small and can be neglected. This reduces the Forchheimer equation to the Darcy equation.

As the flow velocity increases, inertial effects also increase and the flow adapts to the Forchheimer flow regime. These inertial effects are accounted for by the Ergun coefficient C_E and the kinetic energy of the fluid $\rho\mathbf{u}|\mathbf{u}|$. However, (...), a constant Ergun coefficient C_E is valid as long as the fluid flow is laminar. Thus, in the high velocity flow regime, the Ergun coefficient C_E needs to be adapted to reflect the experimental inertial effects" (Jambhekar, 2011).

Although Jambhekar (2011) states that the modified Ergun equation only applies to multi-phase flow, Li and Ma (2011) and Brito et al. (2016) make no such distinction and apply the interpretation put forth in Ergun (1952) for the intrinsic permeability K and intrinsic passability η_p, interpreted in terms of spatial parameters, as follows:

$$K = \frac{d_p^2\phi^3}{C_A(1-\phi)^2} \qquad [\mathrm{m}^2] \tag{2.44}$$

and:

$$\eta_p = \frac{d_p\phi^3}{C_B(1-\phi)} \qquad [\mathrm{m}] \tag{2.45}$$

where ϕ stands for porosity and d_p is the averaged diameter of particles in the porous medium. C_A and C_B are the Ergun constants (Li and Ma, 2011), which take on the values of 150 and 1.75, respectively (Ergun, 1952; Jambhekar, 2011; Li and Ma, 2011). When applied to Equation 2.38, we obtain:

$$-\frac{\partial p}{\partial x} = C_A \frac{(1-\phi)^2 \mu}{d_p^2 \phi} \mathbf{u}_D + C_B \frac{(1-\phi)\rho}{d_p \phi^3} {\mathbf{u}_D}^2 \tag{2.46}$$

For porous media with non-spherical particles, one must consider Li and Ma (2011) study and take into account the equivalent diameters of the non-spherical particles (see Section 2.3.3.3). The constants C_A and C_B in Equations 2.44 and 2.45 for viscous and inertial terms, respectively, may vary based on the data of experiments performed on different porous media comprised of packed beds, with differing values by different authors (Handley and Heggs, 1968; Leva, 1959; Li and Ma, 2011; Macdonald et al., 1979; Roshani, 1993). Figures 2.10 and 2.11 illustrate the discrepancy between using Equation 2.48 as per Li and Ma (2011) and Equation 2.47 with differing values of C_A and C_B as per tables 2.1 and 2.2.

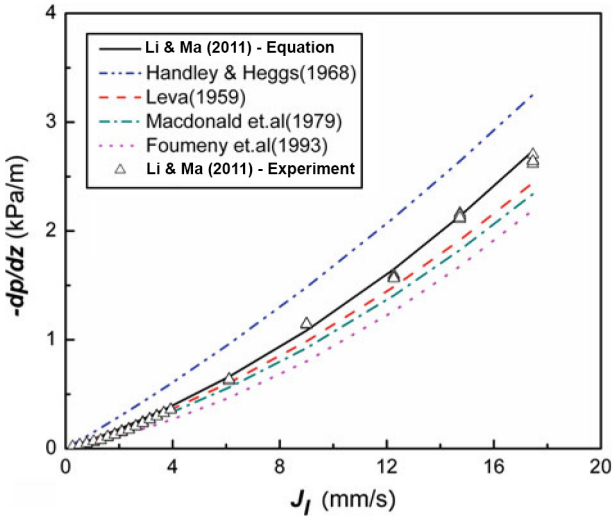

Figure 2.10: Comparisons of experimental data with various models of Equation 2.47 and Equation 2.48 for Li and Ma, 2011 for a test bed packed by 6 mm spheres with 1 mm centric holes and porosity value of $\phi = 0.39$ (Bed-2 in cited study). Adapted from Li and Ma (2011).

Table 2.1: Parameters of various porous models in eq. 2.47 for Bed-2. Adapted from Li and Ma (2011)

Model	**Parameter** C_A	**Parameter** C_B	$d_{sd}(mm)$
Li and Ma, 2011 - eq. 2.48	150	1.75	5
Leva, 1959	200	1.75	5
Handley and Heggs, 1968	368	1.24	5
Macdonald et al., 1979	180	1.8	5
Roshani, 1993	130	2.1	5

"The reason for the variation of the constants is mainly due to the diversity in particles' morphology (shapes) and size distribution, as well as the packing structure of a bed" (Li and Ma, 2011). According to the authors of this study, efforts have been made to

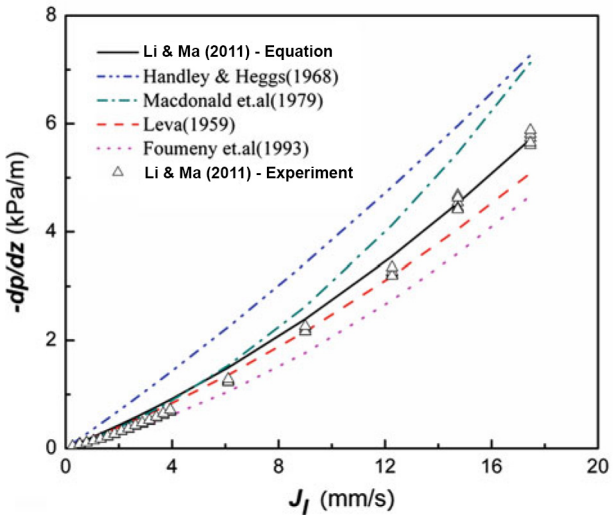

Figure 2.11: Comparisons of experimental data with various models of Equation 2.47 and Equation 2.48 for Li and Ma, 2011 for a test bed packed by particles with 3 mm diameter and 6 mm in length, and porosity value of $\phi = 0.37$ (Bed-5 in cited study). Adapted from Li and Ma (2011).

Table 2.2: Parameters of various porous models in eq. 2.47 for Bed-5. Adapted from Li and Ma (2011)

Model	**Parameter** C_A	**Parameter** C_B	$d_{sd}(mm)$	STDEV (kPa)
Li and Ma, 2011 - eq. 2.48	150	1.75	3.6	-
Leva, 1959	200	1.75	3.6	0.21
Handley and Heggs, 1968	368	1.24	3.6	0.47
Macdonald et al., 1979	180	1.8	3.6	0.37
Roshani, 1993	130	2.1	3.6	0.31

generalize constants C_A and C_B given the inconvenience of having different constants for varying porous media. "It is well known that the Ergun equation with the constants of respective 150 and 1.75 fits the experimental data of spherical packed beds extremely well"(Li and Ma, 2011). In order to still use the Ergun equation for prediction of the frictional pressure drop in porous media consisting of non-spherical particles Li and Ma (2011) set out to determine what effective particle diameter should be employed in the calculation. They first considered the use of the Sauter mean diameter d_{sd} (see Equation 2.22), which gives us the following equation:

$$-\frac{\partial p}{\partial x} = 150\frac{(1-\phi)^2\mu}{d_{sd}^2\phi}\mathbf{u}_D + 1.75\frac{(1-\phi)\rho}{d_{sd}\phi^3}{\mathbf{u}_D}^2 \tag{2.47}$$

However, it was found insufficient in predicting the pressure drop of fluid flow in packed beds with non-spherical particles, proposing instead the equivalent particle diameter d_{eq} (see Equation 2.23), which applied to Equation 2.47 results in the following equation:

$$-\frac{\partial p}{\partial x} = 150\frac{(1-\phi)^2\mu}{d_{eq}^2\phi}\mathbf{u}_D + 1.75\frac{(1-\phi)\rho}{d_{eq}\phi^3}{\mathbf{u}_D}^2 \tag{2.48}$$

This means that the two crucial parameters to be obtained, the linear and non-linear coefficients for the modified Ergun equation α and β, can be quickly estimated taking into account the equivalent particle diameter d_{eq} (see Equation 2.23 and REV porosity ϕ (see Section 2.3.3.1). These coefficient can be derived using the following equations:

$$\alpha = \frac{1}{K} = \frac{150(1-\phi)^2}{d_{eq}^2\phi^3} \qquad [\mathrm{m}^{-2}] \tag{2.49}$$

and:

$$\beta = \frac{1}{\eta_p} = \frac{1.75(1-\phi)}{d_{eq}\phi^3} \qquad [\mathrm{m}^{-1}] \tag{2.50}$$

2.3.5 Flow in hybrid media

As per Lemos (2006), when a macroscopic interface exists between a porous media and a clear fluid, the configuration so formed is called a *hybrid-medium*. There are numerous engineering applications for this sort of medium to be considered in a numerical study, for both laminar and turbulent flow. In this sub-section a brief summary of Lemos (2006) will be given with a focus on the equations and conditions which govern laminar flow and a few considerations for turbulent flow. However, a comprehensive reading and consultation of that work and its sources should be conducted for proper numerical implementation of the methods therein in any numerical tool, for both laminar and turbulent flow conditions.

The focus will here will be on flow in composite channels, i.e., a two-dimensional channel having a layer of porous material inside as illustrated in Figure 2.12. "The channels are partially filled with a layer of porous material. A constant-property fluids flows longitudinally from left to right permeating through both the clear region and the porous structure. Also, in Figure [2.12], B is the distance in between the channel walls and s the clearance for the non-obstructed flow passage.

2.3.5.1 Macroscopic model for laminar flow

Governing equations "A macroscopic form of the governing equations is obtained by taking the volumetric average of the entire equation set. In this development, the porous medium is considered rigid, undeformable, and saturated by an incompressible fluid.

The microscopic continuity equation for the fluid phase is given by":

$$\nabla\cdot(\mathbf{u}) = 0 \tag{2.51}$$

"Applying the volume average operator to Equation 2.51, one has (see Pedras and Lemos (2001))":

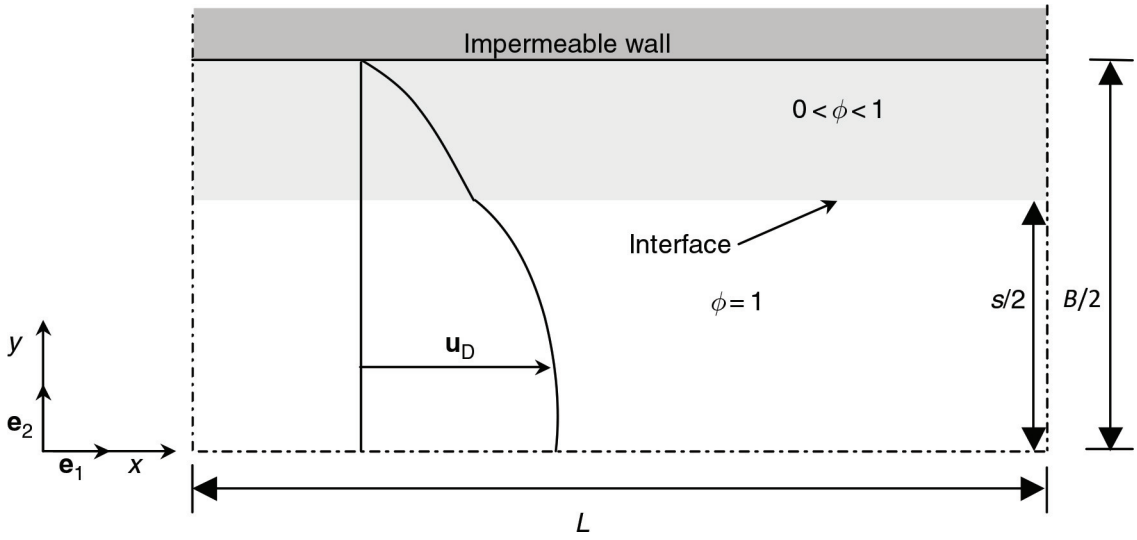

(a) Model without Forchheimer term.

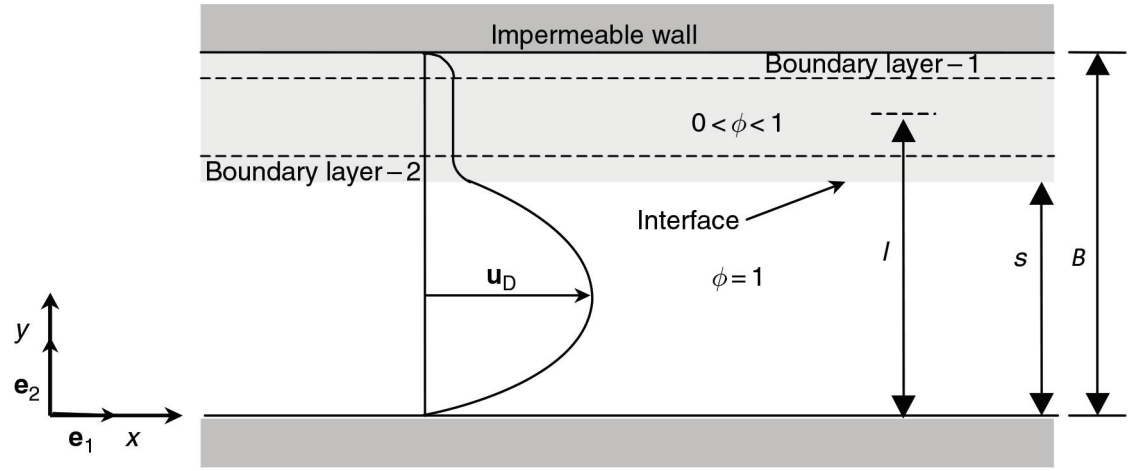

(b) Model with Forchheimer term.

Figure 2.12: Model for channel flow with porous material. Adapted from Lemos (2006).

$$\nabla \cdot (\mathbf{u}_D) = 0 \tag{2.52}$$

"where the local velocity vector **u** is of null value at the local interfacial area $A_i{}^m$ and the Dupuit-Forschheimer relationship [(Brock, 1991; Ritzi and Bobeck, 2008)]" has been used:

$$\mathbf{u}_D = \phi \langle \mathbf{u} \rangle^i \qquad [\mathrm{m \cdot s^{-1}}] \tag{2.53}$$

where $\langle \mathbf{u} \rangle^i$ is the intrinsic (fluid) average of **u** (Equation 2.52) represents the macroscopic continuity equation for an incompressible fluid in a rigid porous medium.

The reason as to why, in a porous medium, one should volume average the Navier–Stokes equations, is that it "allows considering the porous zones as continuous media, characterized by their macroscopic properties only, thus eliminating the need for a detailed

description of their complex internal geometry. Hence, this technique can be thought of as a spatial filter to obtain an average flow behaviour inside porous zones, as already sketched in" Figure 2.2 (Higuera Caubilla, 2015).

The microscopic Navier-Stokes equation for an incompressible fluid with constant properties can be written as:

$$\rho\left[\frac{\partial \mathbf{u}}{\partial t} + \nabla\cdot(\mathbf{u}\mathbf{u})\right] = -\nabla p + \mu\nabla^2\mathbf{u} \tag{2.54}$$

where by applying the volume averaging procedure as per Hsu and Cheng (1990):

$$\rho\left[\frac{\partial}{\partial t}(\phi\langle u\rangle^i) + \nabla\cdot(\phi\langle\mathbf{u}\mathbf{u}\rangle^i)\right] = -\nabla(\phi\langle p\rangle^i) + \mu\nabla^2(\phi\langle\mathbf{u}\rangle^i) + \mathbf{R} \tag{2.55}$$

where:

$$\mathbf{R} = \frac{\mu}{\Delta V}\int_{A_i{}^m}\mathbf{n}\cdot(\nabla\mathbf{u})\,dS - \frac{1}{\Delta V}\int_{A_i{}^m}\mathbf{u}p\,dS \tag{2.56}$$

as in Equation 2.5, the term $\mathbf{R}$ (analogous to the term D_V) represents the total drag per unit volume acting on the fluid by the action of the porous structure. Here, a slightly different (but commonly used) Darcy-Forchheimer extended model, similar to the Ergun equation (Equation 2.43) is given for it:

$$\mathbf{R} = -\left[\frac{\mu\phi}{K}\mathbf{u}_D + \frac{C_F\phi\rho|\mathbf{u}_D|\mathbf{u}_D}{\sqrt{K}}\right] \tag{2.57}$$

where the constant C_F is the non-linear Forchheimer coefficient (albeit a formulation different from the β coefficient). Then, making use of the Dupuit-Forchheimer relation in Equation 2.53, and the Darcy-Forchheimer formulation in Equation 2.57 to Equation 2.55, it can be rewritten as:

$$\rho\left[\frac{\partial \mathbf{u}_D}{\partial t} + \nabla\cdot\left(\frac{\mathbf{u}_D\mathbf{u}_D}{\phi}\right)\right] = -\nabla(\phi\langle p\rangle^i) + \mu\nabla^2\mathbf{u}_D - \left[\frac{\mu\phi}{K}\mathbf{u}_D + \frac{C_F\phi\rho|\mathbf{u}_D|\mathbf{u}_D}{\sqrt{K}}\right] \tag{2.58}$$

Interface condition "The equation proposed in in Ochoa-Tapia and Whitaker (1995a) and Ochoa-Tapia and Whitaker (1995b) for describing the stress jump at the interface between the clear flow region and the porous structures is given by":

$$\mu_e\frac{\partial u_{D_x}}{\partial y}\bigg|_{\texttt{Porous medium}} - \mu_e\frac{\partial u_{D_x}}{\partial y}\bigg|_{\texttt{Clear fluid}} = C_\beta\frac{\mu}{\sqrt{K}}u_{D_x}\bigg|_{\texttt{Interface}} \tag{2.59}$$

where $\mathbf{u}_{Dx}$ is the Darcy velocity component parallel to the interface aligned with direction x and normal to the direction y, $\mu_e = \mu/\phi$ is the effective viscosity for the porous region according to Ochoa-Tapia and Whitaker (1995a) and Ochoa-Tapia and Whitaker (1995b), μ is the fluid dynamic viscosity, K is the intrinsic permeability and C_β an adjustable coefficient which accounts for the stress jump at the interface (Lemos, 2006).

Considerations on turbulent flow This sub-section is by no means supposed to be a comprehensive review of flow in hybrid media and as such only the basic equations for laminar flow were introduced. The interface and jump conditions for turbulent flow are somewhat more elaborate and as such will not be discussed here given that this formulation of porous media is not implemented in OpenFOAM.

As mentioned previously, careful reading of chapter 9 of Lemos (2006) and further consultation of its sources is advised given that it includes a comprehensive review of literature on the subject spanning the last three decades.

Lemos (2006) also points out that there are two distinct lines of investigation on turbulent flow over permeable media. One "is based on the assumption that within the porous layer the flow remains laminar, which, in turn, precludes application of such methodology to flows through highly permeable media as atmospheric boundary layer over forests or crop fields". However, other studies "also emphasize that depending on the permeable structure shape, turbulence may exist inside the porous bed and, as such, a turbulence model must be employed".

2.4 Basic concepts in turbulence modelling

This section will present a brief overview on the valid governing equations for steady state Newtonian fluids and isothermal flows under a constant gravitational field. It will also focus on several turbulence models used for the closure of the Reynolds Averaged Navier-Stokes (RANS) equations with a focus on the models used in this work which are either available in the OpenFOAM package by default or which were able to be adapted for the current work.

2.4.1 Introduction to turbulence modelling

This sub-section will be based on the work by Pope (2000). The fundamentals of turbulent modelling are well established and can be consulted in a large number of easily obtainable sources.

It will also take from the summary and notation by Filonovich (2015), as well as a few additional sources regarding turbulence models not contemplated in her work. As such, the following equations in this subsection will also use the same Cartesian notation where $i = 1$ is for x-direction (along the flow) and stream-wise velocity component u, $i = 2$ is for y-direction (across the flow) and transversal velocity component v, and $i = 3$ is for z (orthogonal to the fluid bed) and vertical velocity component w.

2.4.1.1 Governing equations and Reynolds averaging

The basic system of governing equations for incompressible fluid flow is based on the conservation laws of physics, namely the conservation of mass (continuity equation, see Equation 2.32) and the conservation of momentum (Newton's second law).

As per Pope (2000), the mass-conservation or continuity equation for an incompressible fluid can be written in the long form:

$$\nabla \cdot (\mathbf{u}) = \frac{\partial u}{\partial x} + \frac{\partial v}{\partial y} + \frac{\partial w}{\partial z} = 0 \tag{2.60}$$

or

$$\frac{\partial u_i}{\partial x_i} = 0 \tag{2.61}$$

The equation for the conservation of momentum states that the rate of change of momentum equals the sum of the forces on a fluid element. For a constant property such as density or viscosity, Newtonian fluid and isothermal flow under a constant gravitational field can be written as (Pope, 2000):

$$\frac{\partial u_i}{\partial t} + u_j \frac{\partial u_i}{\partial x_j} = -\frac{1}{\rho}\frac{\partial p}{\partial x_i} + \frac{\partial}{\partial x_j}\left(\nu \frac{\partial u_i}{\partial x_j}\right) + f_i \tag{2.62}$$

where p is the instantaneous pressure field, ρ is the fluid density, ν is the fluid kinematic viscosity and f_i are body forces. Equations [2.62] are known as Navier-Stokes equations for constant property Newtonian fluids.

Equations 2.62 are theoretically enough to fully describe both the laminar and turbulent fields using Direct Numerical Simulation (DNS). "However, the numerical solution is extremely difficult, since the significantly different length and times scales in a turbulent field need to be resolved, and thus the stable solution requires such a fine mesh resolution that the computational effort grows rapidly with increasing [Re]. Thus, practically in most turbulent flows the flow-field variables are decomposed into the mean and fluctuating parts" (Filonovich, 2015), in a process known as the Reynolds decomposition, which can be expressed as:

$$\mathbf{u} = \mathbf{U} + \mathbf{u}' \tag{2.63}$$

or,

$$u_i = U_i + u_i' \tag{2.64}$$

for the velocity and the following Equation for pressure:

$$p = P + p' \tag{2.65}$$

where $\mathbf{u}$ and u_i are (respectively) the instantaneous velocity vector and velocity vector component (u, v and w for $i = 1$, $i = 2$ and $i = 3$, respectively), u' and u_i' the fluctuating part (vector and component) for which $\overline{u_i'} = 0$, and U and U_i is the mean velocity vector and component. "Note that this mean value should be obtained from classic statistics knowing the probability density function of the random variable (velocity field). However, a very common approach, also adopted here, is to consider that the flow is statistically

stationary (*i.e.* all statistics are invariant under a shift in time). This allows estimating the statistical mean by performing a time-average(over a time interval). For statistically stationary flows, the time-averaged value tends to the statistical mean value as the used time interval tends to infinity (*e.g.* Pope (2000))" (Filonovich, 2015).

Substituting the decomposition 2.64 for velocity and pressure into the continuity and momentum equations ([Equations 2.60 and 2.62]), and then by time averaging all the terms in the equations and taking into account that $p' = 0$, $\overline{u_i'} = 0$ and $\overline{U_i} = U_i$, and taking into consideration that $\nabla \cdot (u_i) = \nabla \cdot (U_i)$, the RANS equations for constant-property Newtonian fluids are obtained:

$$\frac{\partial U_i}{\partial x_i} = 0 \tag{2.66}$$

$$\frac{\partial U_i}{\partial t} + U_j \frac{\partial U_i}{\partial x_j} = -\frac{1}{\rho}\frac{\partial P}{\partial x_i} + \frac{\partial}{\partial x_j}\left(\nu \frac{\partial U_i}{\partial x_j}\right) - \frac{\partial \overline{u_i' u_j'}}{\partial x_j} \tag{2.67}$$

"The last term in Equation 2.67 is new compared to equation 2.62. An extra term in Equation 2.67, $-\overline{u_i' u_j'}$, is the fluctuating contribution to the nonlinear convective acceleration term in the momentum equation 2.62, also called the apparent stress arising from the fluctuating velocity field (Pope, 2000). This apparent stress tensor is $-\overline{u_i' u_j'}$ which statistically represents the correlation matrix between fluctuating components of the velocity field, is also denominated the Reynolds stress tensor" (Filonovich, 2015).

2.4.2 Problems and limitations in turbulence modelling.

"Turbulence can either be resolved or modelled. Resolving implies proper solution of the governing equations (at all scales) with no modelling or empirical assumptions. Modelling implies a solution that uses some degree of approximation and empiricism.

There are three levels of resolving turbulence: fully resolved, partially resolved, and unresolved. DNS is one technique that attempts to fully resolve turbulent flow by solving the Navier-Stokes equations at all length and times scales. In DNS, turbulence or empirical models are not required. The ample variation in length and time scales is an important characteristic of turbulent flows which is in part responsible for the difficulty encountered in the numerical and theoretical analysis of turbulent flows. The largest [L] in the flow account for most of the transport of momentum and energy. The size of these eddies is constrained by the physical boundaries of the flow. Thus, for compound channel flow the largest eddies can have the size of the channel width.

Kinetic energy from the largest eddies is transferred to the smaller eddies during the cascading process until it is dissipated into heat (Pope, 2000). As we approach [ever] smaller length scales, the viscous effects become more important. Thus, the size of the smallest eddies, [η], at which this energy is dissipated depends on the [ϵ and ν] and is defined as":

$$\eta = \left(\frac{\nu^3}{\epsilon}\right)^{\frac{1}{4}} \qquad [-] \tag{2.68}$$

"This length scale is called the Kolmogorov length scale and it characterizes the smallest dissipative eddies. Therefore, it corresponds to the smallest length scale needed to properly resolve turbulent flow. The $[\tau]$ of the smallest eddies is":

$$\tau = \left(\frac{\nu}{\epsilon}\right)^{\frac{1}{2}} \qquad [-] \tag{2.69}$$

"The ratio of the largest to smallest length scales and times scales in the flow is proportional to the $[Re]$ raised to the $\frac{3}{4}$ and $\frac{1}{2}$ power, respectively. For example, in a flow with a $[Re]$ of 10^5, the ratio L/η is proportional to $10^{\frac{15}{4}}$. Thus , to resolve the entire range of length scales in 3D turbulence flow, we would need a computational domain that consists of at least 10^{10} grid points. The amount of information resulting from such simulation would exceed the capacity of any existing computer. This becomes even clearer when the unsteady, transient nature of turbulence is considered. Thus, the problem with DNS is that it consumes enormous computational resources since the grid resolution must be on the order of the Kolmogorov scales as indicated in previous paragraphs. Currently, DNS is a research tool and is only feasible for simple flows at lower $[Re]$ (...).

Large Eddy Simulation (LES) attempts to partially resolve turbulence. The fundamental idea is that the small scales of turbulence (close to the Kolmogorov scales) can be modelled by a subgrid model, while the larger scales are resolved by the governing equations. Grid resolution is on the order of the turbulent scale that wants to be solved, thus in LES the computational demands are considerably smaller than in DNS. The LES has become more and more popular and shows good results when compared to experimental data (...). Nevertheless, its application to real setups is still impractical, due to the exceptionally high computational effort required.

The most practical and still the most popular method of dealing with turbulence is that based on RANS equations. Only mean flow quantities are resolved. In the RANS method, all scales of turbulence are modelled; grid resolution is in the order of the mean flow scale - not a turbulent scale. This offers huge computational savings when compared to both DNS and LES. The complexity of RANS models ranges from purely algebraic or zero-equation models to a more complex [RSM]. Reynolds stresses appearing in RANS have to be related to the mean motion itself before the equations can be solved, since the number of unknowns and number of equations must be equal.

From Equations 2.66 and 2.67 we have 10 unknowns (p, U_1, U_2, U_3, and six Reynolds stresses $-\overline{u_i' u_j'}$) and only four equations, which configures an unclosed mathematical problem. The absence of these additional equations is often referred to the turbulence closure problem. To close these equations, *i.e.* have the same number of equations and unknowns, extra equations are introduced through the different turbulence models" (Filonovich, 2015).

2.4.3 Eddy viscosity models

This section will briefly address the eddy viscosity (or turbulence-viscosity) models. These models can be divided into linear and non-linear model, the former being subdivided into three categories: zero- (or algebraic), one- and two-equation models; the latter is sub-divided into two categories: Explicit non-linear constitutive relation and v2-f models (CFD-Online, 2017).

2.4.3.1 Linear eddy viscosity models

Linear models "use the Boussinesq eddy viscosity concept (Boussinesq, 1877). In analogy to viscous stresses in laminar flow, the turbulent stresses are assumed to be proportional to the mean velocity gradients (...). The Reynolds stress tensor is then related to the mean flow field through":

$$-\overline{u_i' u_j'} = \nu_t \left(\frac{\partial U_i}{\partial x_j} + \frac{\partial U_j}{\partial x_i} \right) - \frac{2}{3} k \delta_{ij} \qquad [\mathrm{m^2 \cdot s^{-2}}] \tag{2.70}$$

where ν_t is the eddy viscosity, δ_{ij} is the Kronecker delta ($\delta_{ij} = 1$ for $i = j$; and $\delta_{ij} = 0$ for $i \neq j$); and k is the turbulence kinetic energy, defined as:

$$k = \frac{\overline{u_i' u_i'}}{2} \qquad [\mathrm{m^2 \cdot s^{-2}}] \tag{2.71}$$

As Filonovich (2015) shows in her work, "the primary goal of many turbulence models is to find some estimation for the eddy viscosity to model the Reynolds stresses. These may range from the relatively simple algebraic models, to the more complex models such as the $k - \epsilon$ model, where two additional transport equations are solved in addition to the mean flow equations". Here, both linear and non-linear eddy viscosity models will be presented, namely the standard linear $k-\epsilon$ (an extensive presentation of which as applied to vegetated open channel flow can be found in Lopez and Garcia (1997)) two-equation model and the non-linear $k - \epsilon$ Shih model (Shih et al., 1994). A more comprehensive presentation of two-equation models can be consulted in Pope (2000) and Versteeg and Malalasekera (2007), and details of other turbulence models can be consulted in existing literature such as Cebeci (2004), Pope (2000), Rodi (1980), and Wilcox (2006). "The two-equation models are the simplest complete models, since these models provide independent transport equations for both variables, the turbulence kinetic energy and the turbulence length scale, or some equivalent parameter.

[Kolmogorov (1942) and Prandtl (2004)] suggested determining the distribution of k by solving a model transport equation for this quantity, which can be obtained by introducing the Reynolds decomposition in the Navier-Stokes equations, multiplying by the velocity and taking time-average of the resulting equation (*e.g.* Pope, 2000). The resulting transport equation for k can be written as":

$$\underbrace{\frac{\partial k}{\partial t}}_{\substack{\text{Rate of}\\ \text{change}\\ \text{of } k}} + \underbrace{U_i \frac{\partial k}{\partial x_i}}_{\substack{\text{Convective}\\ \text{transport}\\ \text{of } k}} = \underbrace{-\frac{\partial}{\partial x_i}\left[\overline{u_i'\left(\frac{u_j'u_j'}{2}+\frac{p'}{\rho}\right)}\right]}_{\text{Turbulent transport of } k} - \underbrace{\overline{u_i'u_j'}\frac{\partial U_i}{\partial x_j}}_{\substack{\text{Turbulence}\\ \text{production } (P_k)}} \underbrace{-\nu\overline{\frac{\partial u_i'}{\partial x_j}\frac{\partial u_i'}{\partial x_{j]}}}}_{\epsilon} \tag{2.72}$$

"Equation 2.72 is the exact k-equation and is of no use in the turbulence model since new unknown correlation appear in the dissipation terms. To obtain a closed set of equations, model assumptions must be introduced for these terms. Thus, [the] turbulent transport term is often modelled with a gradient-diffusion concept (Equation 2.73). The reader should keep in mind that gradient diffusion hypothesis is applicable to high Reynolds number flows and is not valid in certain regions, such as the viscous sublayer near walls.

Assuming that the turbulent transport of k is proportional to the gradient of k" (Filonovich, 2015):

$$-\overline{u_i\left(\frac{u_j'u_j'}{2}+\frac{p'}{\rho}\right)} = \frac{\nu_t}{\sigma_k}\frac{\partial k}{\partial x_i} \tag{2.73}$$

where σ_k does not have a universal value and for which empirical values in the range of $[0.3, 1.3]$ have been used, although it generally uses 1 as its value. The selected value of σ_k has a significant effect on the prediction of the results, for reasons which it's been recommended to determine it taking into the consideration the dominant flow structures in any given case. Taking into account the assumptions in Equations 2.70 and 2.73, Equation 2.72 now reads:

$$\underbrace{\frac{\partial k}{\partial t}}_{\substack{\text{Rate of}\\ \text{change}\\ \text{of } k}} + \underbrace{U_i \frac{\partial k}{\partial x_i}}_{\substack{\text{Convective}\\ \text{transport}\\ \text{of } k}} = \underbrace{\frac{\partial}{\partial x_i}\left(\frac{\nu_t}{\sigma_k}\frac{\partial U_i}{\partial x_i}\right)}_{\substack{\text{Turbulent transport}\\ \text{of } k}} + \underbrace{\nu_t\left(\frac{\partial U_i}{\partial x_j}+\frac{\partial U_j}{\partial x_i}\right)\frac{\partial U_i}{\partial x_j}}_{\substack{\text{Turbulence}\\ \text{production } (P_k)}} - \underbrace{\epsilon}_{\substack{\text{Rate of}\\ \text{dissipation}\\ \text{of } k}} \tag{2.74}$$

According to Filonovich (2015), "the choice of second variable in two-equation models is arbitrary and many proposals have been presented", with suggested equations for dissipation rate ϵ:

$$\epsilon = \frac{k^{\frac{3}{2}}}{l} \qquad [\mathrm{m^2 \cdot s^{-3}}] \tag{2.75}$$

with l being a turbulence length-scale, which is a physical quantity describing the size of the large energy-containing eddies in a turbulent flow, and is used to determine the relationship between the Taylor and Kolmogorov scales (Pope, 2000)). The Taylor micro-scale is an intermediate length scale at which fluid viscosity significantly affects the dynamics of turbulent eddies in the flow and is traditionally applied to turbulent flow which can be characterized by a Kolmogorov spectrum of velocity fluctuations. A

suggested equation for turbulence frequency ω with use of the turbulence length-scale l is:

$$\omega = \frac{k^{\frac{1}{2}}}{l} \qquad [\mathrm{s}^{-1}] \tag{2.76}$$

It is of note however that there are other suggested formulations for both ϵ and k. As per the CFD-Online turbulence properties calculator (CFD-Online, 2016), a suggested equation which relates k, ϵ and ω is:

$$\omega = \frac{\epsilon}{k\beta^*} \qquad [\mathrm{s}^{-1}] \tag{2.77}$$

where β^* is a model constant, most often set to the empirical constant $C_\mu = 0.09$, although some codes use a different definition without the model constant (CFD-Online, 2016; Filonovich, 2015). From CFD-Online (2016), the turbulence length scale l can be obtained from the following equation:

$$l = C_\mu \frac{k^{\frac{3}{2}}}{\epsilon} \qquad [\mathrm{m}] \tag{2.78}$$

however, for certain CFD codes such as Fluent, Phoenics and CFD-ACE, l is calculated with the following equation:

$$l = C_\mu^{\frac{3}{4}} \frac{k^{\frac{3}{2}}}{\epsilon} \qquad [\mathrm{m}] \tag{2.79}$$

"The $k-\epsilon$ model is the best known two-equation turbulence model and is incorporated in most commercial CFD codes. The most used formulation of the $k-\epsilon$, referred as the 'standard' $k-\epsilon$ model, is of Jones and Launder (1972). Those authors proposed the following transport equation for the dissipation rate:

$$\underbrace{\frac{\partial \epsilon}{\partial t}}_{\substack{\text{Rate of}\\ \text{change}\\ \text{of } \epsilon}} + \underbrace{Ui\frac{\partial \epsilon}{\partial x_i}}_{\substack{\text{Transport}\\ \text{of } \epsilon \text{ by}\\ \text{convection}}} = \underbrace{\frac{\epsilon}{k}(C_{\epsilon 1}P - C_{\epsilon 2}\epsilon)}_{\substack{\text{Production and}\\ \text{dissipation}\\ \text{rate of } \epsilon}} + \underbrace{\frac{\partial}{\partial x_i}\left(\frac{\nu_t}{\sigma_\epsilon}\frac{\partial \epsilon}{\partial x_i}\right)}_{\substack{\text{Turbulent transport}\\ \text{of } \epsilon}} \tag{2.80}$$

where the eddy viscosity used in the model is specified as:

$$\nu_t = C_\mu \frac{k^2}{\epsilon} \qquad [\text{-}] \tag{2.81}$$

It should be referred that equation 2.80 is not the exact transport equation for ϵ, but rather an entirely empirical equation that can account better for the fact that ϵ is determined by the large-scale motions (energy cascade) instead of motions in the dissipative range (*cf.* Pope, 2000). The $k-\epsilon$ model involves the five empirical constants C_μ, $C_{\epsilon 1}$, $C_{\epsilon 2}$, σ_k and σ_ϵ. Their standard values for open-channel flows are presented in table 2.3. The choice of these constants is based on the compatibility of the model to the logarithmic velocity distribution near the wall in channel flows with Von Kármán constant κ (...).

In open-channel flows, vertical fluctuations, w', are damped by the free-surface, which results in ν_t approaching to zero near the free-surface (...). This surface damping can be accounted for in the $k-\epsilon$ model by decreasing C_μ near the free-surface by means of damping functions, or surface-proximity function.

Table 2.3: Values of the constants in the $k-\epsilon$ model for open channel flows. Adapted from Filonovich (2015)

C_μ	$C_{\epsilon 1}$	$C_{\epsilon 2}$	σ_k	σ_ϵ
0.09	1.44	1.92	1.2	1.2

"Another popular two-equation model is the $k-\omega$ model (being the turbulence frequency [ω defined as per Equation 2.77]), which will be presented here in the form given by WILCOX (1988). The $k-\omega$ model solves the k-transport equation (2.74) and a transport equation for ω, instead of the ϵ-equation (2.75). The k-transport equation, re-written replacing $\epsilon = k\omega$, and the transport equation for w can be written (WILCOX, 1988)":

$$\frac{\partial k}{\partial t} + U_i \frac{\partial k}{\partial x_i} = \frac{\partial}{\partial x_i}\left(\frac{\nu_t}{\sigma_k}\frac{\partial k}{\partial x_i}\right) + P - \beta' k\omega \tag{2.82}$$

$$\frac{\partial \omega}{\partial t} + U_i \frac{\partial \omega}{\partial x_i} = \frac{\partial}{\partial x_i}\left(\frac{\nu_t}{\sigma_k}\frac{\partial \omega}{\partial x_i}\right) + \alpha_\omega \frac{\omega}{k} P - \beta_\omega k\omega \tag{2.83}$$

with the eddy viscosity given by:

$$\nu_t = \frac{k}{\omega} \qquad [\text{-}] \tag{2.84}$$

"The $k-\omega$ involces five empirical constants β', [β_ω], [α_ω], σ_k and σ_ω. Their standard values are presented in Table [2.4]".

Table 2.4: Values of the constants in the $k-\omega$ model for open channel flows. Adapted from Filonovich (2015)

β'	β_ω	α_ω	σ_k	σ_ω
0.09	0.075	$\frac{5}{9}$	2	2

"Another two-equation model was proposed by Menter (1994), which combines the best behaviour of the $k-\epsilon$ and $k-\omega$ models ($k-\omega$ performs better near the wall region and $k-\epsilon$ performs better in the fully turbulent region). This model is implemented into ANSYS-CFX (CFX) and it is known as the [Menter's BaSeLine $k-\omega$ turbulence model (BSL)]" (Filonovich, 2015). Filonovich (2015) presents this model in detail in the main thesis as well as in two research papers contained therein. Although this model isn't originally implemented in OpenFOAM, a third party implementation of a hybrid model which makes use of BSL is presented in chapter 3 and its results in chapter 4.

Filonovich (2015) also describes another popular two-equation model, also presented by Menter (1993), the SST $k-\omega$ model, which "accounts for the transport of the turbulent stresses, according to modifications introduced to the original $k-\omega$ model by Menter".

In her summary and presentation of linear eddy viscosity turbulence models, Filonovich (2015) comes to the conclusion that "two-equation models have proven that they perform reasonably well for a wide range of flows of engineering interest, with some limitations that may be accounted with the use of special bounding or damping functions. Their major advantage is the simplicity, and the low computational cost compared to more complex models, such RSM or LES.

Generally, neither two-equation model, $k-\epsilon$ of $k-\omega$ model, is capable of giving quantitatively good results for more complicated flows. As pointed out by Wilcox (2006), these models can fail drastically for flows with sudden changes in means train rate, curved surfaces, secondary motions, rotation, or if the flow is highly 3D. Regretfully, most flows of interest include some or all of these features. While two-equation models may be able to give qualitative results for such flows, generally a further level of complexity is needed in the model to obtain close agreement with experiments" as shown in Research Paper III in Filonovich (2015).

2.4.3.2 Non-linear eddy viscosity models

"Linear eddy viscosity models such as the well-known standard $k-\epsilon$ model are based on the isotropic linear stress–strain relation proposed by Boussinesq (1877), which assumes that the unknown turbulent fluxes, $\overline{u_i' u_j'}$, are proportional to the strain rate".

$$\frac{\overline{u_i' u_j'}}{k} = \frac{2}{3}\delta_{ij} - 2\frac{nu_t}{k}S_{ij} \tag{2.85}$$

"The Boussinesq linear stress–strain relation does not make differences among the normal stresses and thus it fails in predicting anisotropic turbulence in actual flow cases. Non-linear models try to eliminate this deficiency by considering non-linear relationships between Reynolds stresses and strain rates.

(...)

Non-linear eddy viscosity models are in an intermediate class between the linear eddy viscosity models and full Reynolds stress transport models (RSM). Non-linear models describe the Reynolds stress explicitly in an algebraic expression in terms of the strain rate and the vorticity tensors. All non-linear models have the same basic stress–strain formulation in the general form of Ehrhard and Moussiopoulos (2000)" (Bazdidi-Tehrani et al., 2015).

These models are considered a potential alternative to RSM models (mentioned in the next sub-section) due to their relatively less taxing computational requirements. as they retain elements of the linear eddy-viscosity framework, "based on the constitutive relations linking the Reynolds-stresses to non-linear expansions of strain and vorticity

components. These may be cast in a form of additive terms, each pre-multiplied by an apparent viscosity - hence the term 'non-linear eddy-viscosity models'" (Lien et al., 1996).

There are quadratic and cubic non-linear models implemented in OpenFOAM, based on the work of Lien et al. (1996) and Shih et al. (1994), the LienCubicKE and NonlinearKEShih, respectively.

The NonlinearKEShih implementation into the test cases were able to produced residual stabilization, which was not obtained for the LienCubicKE model. Further refinement of the test cases must be made in order to properly implement this latter model into the present work.

NonlinearKEShih model This model is based on the dynamic equation of the mean-square velocity fluctuation for Large Reynolds number turbulence, the advantage of which is that the physical meanings of the terms in this equation are clearer than those in the dissipation rate equation, and in his work Shih et al. (1994) showed considerable improvement over the standard $k-\epsilon$ model. Model applications for which this model is considered valid for are:

1. Rotating homogeneous shear flows.
2. Free shear flows.
3. Channel flow and boundary layers with and without pressure gradients.
4. Backward-facing step flows.

LienCubicKE model This model cites as references in its source code Etemad et al. (2006) and Lien et al. (1996). The latter is the original proposal for both quadratic and cubic versions of the model while the former provides a comparative study between high- and low-Re non-linear eddy-viscosity models.

The LienCubicKE models are a low-Re derived from high Re models (Lien et al., 1996). "These are denoted 'lowRe' because by using damping functions, their validity is not only restricted to the region remote from the wall, but also down to the solid wall. This includes the viscous sub-layer (low-Reynolds number region). No wall function is needed for these models. However, the computational grid should resolve the boundary layer so that the wall adjacent cell centres have y^+ values about unity" (Etemad et al., 2006).

2.4.4 Reynolds Stress Models

"The most complex classical turbulence model is the **Reynolds stress equation model** (RSM), also called the second-order or second-moment closure model [(Second Moment Closure (SMC))]. Several major drawbacks of the $k-\epsilon$ model emerge when it is attempted to predict flows with complex strain fields or significant body forces. Under such conditions the individual Reynolds stresses are poorly represented by formula 2.70 even if

the turbulent kinetic energy is computed to reasonable accuracy. The exact Reynolds stress transport equation on the other hand can account for the directional effects of the Reynolds stress field. The modelling strategy originates from work reported in Launder et al. (1975).

(...)

RSMs are clearly quite complex, but it is generally accepted that they are the 'simplest' type of model with the potential to describe all the mean flow properties and Reynolds stresses without case-by-case adjustment. The RSM is by no means as well validated as the $k-\epsilon$ model, and because of the high cost of computations it is not so widely used in industrial flow calculations. Moreover, the model can suffer from convergence problems due to numerical issues associated with the coupling of the mean velocity and turbulent stress fields through source terms. The extension and improvement of these models is an area of very active research" (Versteeg and Malalasekera, 2007).

As per Bauer (2017b), one should consider using RSM models for the following types of flows:

- Free shear flows with strong anisotropy, like a strong swirl component. This includes flows in rotating fluids.
- Flows with sudden changes in the mean strain rate.
- Flows where the strain fields are complex, and reproduce the anisotropic nature of turbulence itself.
- Flows with strong streamline curvature.
- Secondary flow.
- Buoyant flow.

"Reynolds stress models have shown superior predictive performance compared to eddy-viscosity models in these cases. This is the major justification for Reynolds stress models, which are based on transport equations for the individual components of the Reynolds stress tensor and the dissipation rate. These models are characterized by a higher degree of universality. The penalty for this flexibility is a high degree of complexity in the resulting mathematical system. The increased number of transport equations leads to reduced numerical robustness, requires increased computational effort and often prevents their usage in complex flows.

Theoretically, Reynolds stress models are more suited to complex flows, however, practice shows that they are often not superior to two-equation models. An example of this is for wall-bounded shear layers, where despite their (theoretically) higher degree of universality, Reynolds stress models often prove inferior to two-equation models" (Bauer, 2017b).

A comprehensive summary of the RSM models used by Filonovich (2015) can be consulted in that work so as to better contextualize her analysis as per Section 2.5. Here, only the two RSM models which were used in this study will be briefly mentioned.

2.4.4.1 LRR model

The LRR (Launder et al., 1975), which often refers to the Isotropization of production model of the LRR (LRR-IP) version of this turbulence model (the other being the Quasi-isotropic LRR (LRR-QI) (Bauer, 2017b; Filonovich, 2015)) is often included in numerical codes for historic reasons and because they are standard models (Bauer, 2017b).

However, its limitations and deficiencies have been pointed out as far back as Speziale (1987), who mentions that at that time linear two-equation models were still preferred over second-order closure models such as LRR since "the computational effort is more than doubled since transport equations must be solved for each individual component of the Reynolds stress tensor (...). Furthermore, in order to obtain these transport equations for the Reynolds stresses, closure models for the higher-order turbulence correlations must be provided which have uncertain physical foundations".

Speziale and Xu (1996) reiterate that "during the past decade, it has become apparent that second order closure models - as they have commonly been formulated since Launder et al. (1975) - perform poorly in the prediction of even basic turbulent flows that are far from equilibrium. Rapidly distorted homogeneous turbulence constitutes a notable example of where it has been shown that the existing hierarchy or second-order closures break down, yielding extremely poor predictions at times (...). This poor performance can occur for dimensionless shear rates that are as little as a factor of five larger than the corresponding equilibrium value. Such a factor occurs in practical turbulent flows".

As mentioned previously, the application of the LRR turbulence model implemented in OpenFOAM did not yield any valid results, even though residuals converged into stable values. The intricacies of wall bounded flows and other shortcomings of the solver which was used (see Chapter 5) likely contributed to the results obtained in numerical simulation.

2.4.4.2 BSL-EARSM model

As per Bauer (2017a), EARSM models "represent an extension of the standard two-equation models. They are derived from the Reynolds stress transport equations and give a nonlinear relation between the Reynolds stresses and the mean strain-rate and vorticity tensors. Due to the higher order terms, many flow phenomena are included in the model without the need to solve transport equations. The EARSM enables an extension of the current ($k-\epsilon$ and BSL) turbulence models to capture the following flow effects:

- Secondary flows
- Flows with streamline curvature and system rotation."

There are several EARSM models, with the one implemented in CFX being the Wallin & Johansson Explicit Algebraic Reynolds Stress Model (WJ-EARSM) which is based on a recalibrated LRR, "from which a fully explicit and self-consistent algebraic relation is derived. The approach replaces the eddy-viscosity assumption by a more general constitutive relation for the Reynolds stress anisotropy in terms of the strain- and rotation rate tensors" (Franke et al., 2005). This model was the basis for combining EARSM with the ω equation based BSL model, "to avoid free-stream sensitivities and ambiguities in comparison with the SST model" (Menter et al., 2012).

It is this formulation which is applied both to CFX (Bauer, 2017a) and to OpenFOAM (Jeyapaul, 2015; Yogesh, 2017), albeit each with their particular differences. According to Jeyapaul (2015), the "model is similar to the implementation in CFX, except for few differences noted below. The model solves for a Poisson equation in the first iteration to evaluate the wall distance. A low-Reynolds number boundary condition is used for omega. (...)

The equivalent model in ANSYS CFX-14 is the 'BSL EARSM' model. However, there are two differences.

- P_1 and P_2 have the coefficient of II_s to be different from [Menter et al. (2012)]. For P_1 the coeff. is 0.466875, while reference uses 0.45. For P_2 the coeff. is 0.93375, while the reference uses 0.9. This has a minor influence.

- The turbulence timescale does not use the Durbin limiter ([see validation study and Durbin (2009)]). This influences the near-wall predictions."

A small verification study for the model is made available at the source, with further description of how it was adapted for use in OpenFOAM.

2.5 Numerical modelling of open-channel flow

This section presents an overview of some of the most important aspects regarding numerical modelling of open-channel flow, particularly the types of open-channel flow (rectangular open-channel and trapezoidal compound open-channel) and turbulence models (RANS and RSM) addressed in this thesis. It's based primarily on Filonovich (2015) literature review. Further details on other types of open-channels are included in Filonovich (2015) and sources therein. The review given has already been summarized to begin with, and is further condensed in this work to the bare minimum required to make sense of the research presented in this thesis.

2.5.1 Historical developments and basic concepts

"In the past open-channel flows have been modelled using One Dimensional (1D) Saint-Venant equations (Saint-Venant, 1871). It is a simplification from two-dimensional shallow water equations, which are also known as the two-dimensional Saint-Venant equations. These 1D models contain [a] high level of empiricism which has been investigated experimentally, (...). Based on these experimental results a number of 1D methods were developed, such as [the] CoHerence Method (COHM) of Ackers (1993a) and Ackers (1993b), the Weighted Divided Channel Method (WDCM) of Lambert and Myers (1998) and the Shiono and Knight Method (SKM) of Shiono and Knight (1991). With advances in computer power, the interest has risen in applying more complex Three Dimensional (3D) models. However, (...), most of the models applied to open-channel flow are either 1D or Two Dimensional (2D) with few applications of 3D models due to the inherent difficulties found in applying CFD in natural river channels" (Filonovich, 2015).

As with Filonovich (2015), this research also partly focuses on compound open-channel flow. "Most rivers have compound cross-section consisting of the main channel and one or more floodplains on the lateral side, as shown in Figure 2.13.

For most of the time water flows only in the main channel. However, during floods the flow can overtop the river banks, inundating the floodplains and originating a compound section configuration. Compound channel flow is characterized by complicated 3D flow structures. These structures are called secondary flows and have been classified into two categories by [Prantdl (Prandtl, 2004)]. He distinguished the secondary flows of the first kind, which are derived from the mean flow skewing and by the centrifugal forces in curved or meandering channels, and the secondary flows of the second kind, which are generated by the non-homogeneity and anisotropy of turbulence" (Filonovich, 2015).

Filonovich (2015) characterizes turbulent flow as homogeneous when the fluctuating velocity field is statistically homogeneous "(*i.e.* all statistics are invariants under a shift in position or, in other words, under translations)", and isotropic when the fluctuating velocity field is statistically invariant to both, translations (homogeneous), rotations and reflections (*i.e.* all statistics are invariants) which implies zero mean velocity gradients" as per Pope (2000) for both cases. "There are several approaches for studying secondary flows (...). One of the approaches, which is widely used by researchers, is based on time-averaged vorticity equation. This equation stems from [the] Navier-Stokes (momentum) equation (Equation 2.67) and can be derived by eliminating the pressure term through cross-differentiation [by focusing] on Prandtl's second kind secondary flows, based on equation for streamwise vorticity Ω_1 (Equation 2.87), which, for steady and uniform flows in straight channels, *i.e.* $\partial/\partial t = 0$ and $\partial/\partial x = 0$, can be expressed as":

$$U_2\frac{\partial\Omega_1}{\partial x_2} + U_3\frac{\partial\Omega_1}{\partial x_3} = \frac{\partial^2}{\partial x_2 \partial x_3}\left(\overline{u_3' u_3'} - \overline{u_2' u_2'}\right) + \left(\frac{\partial^2}{\partial x_2^2} - \frac{\partial^2}{\partial x_3^2}\right)\overline{u_2' u_3'} + \nu\nabla^2\Omega_1 \tag{2.86}$$

where

$$\Omega_1 = \frac{\partial U_2}{\partial x_3} - \frac{\partial U_3}{\partial x_2} \qquad [s^{-1}] \tag{2.87}$$

"Secondary currents of the second kind are generated as a result of differences between the first and the second Right Hand Side (RHS) terms of equation [2.86]. The magnitude of the secondary flows of the second type is about 2-3% of the maximum stream-wise velocity (...), however, they have a major impact on the mean flow and turbulence structures. In order to understand the behaviour of these secondary flow structures, it is helpful to investigate simpler cases, such as the inbank flow in straight rectangular and trapezoidal open-channels". Filonovich (2015) thus focuses on summarizing the main aspect of straight simple and compound channel flows, keeping in mind that natural river channels are usually neither rectangular, nor prismatic. This review will be briefer still, focusing solely on Filonovich (2015) conclusions regarding rectangular open-channels and trapezoidal compound channels as these are the most relevant to the numerical analysis of the present work.

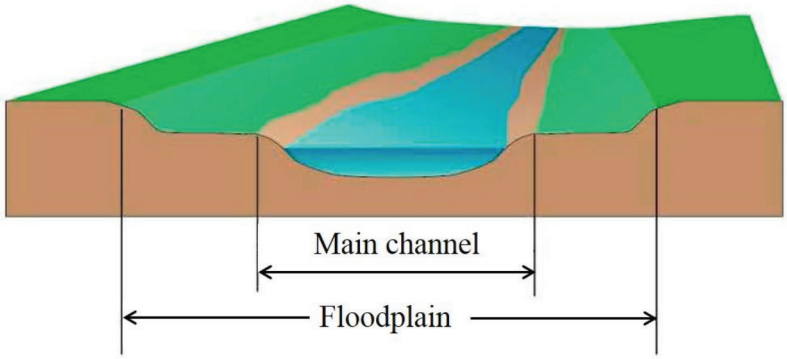

Figure 2.13: Schematic representation of natural river. Adapted from Filonovich (2015).

2.5.2 Inbank flows in straight channels

"In order to understand the more complex 3D turbulent structures of compound channel flow, a basic understanding of inbank flows is essential. The aspect ratio, B/H, defined as the ratio between the width of the channel B and the depth of the flow H, and the geometry have an impact on the flow structures in open-channel flows. The main characteristics of flow in straight inbank channels are briefly reviewed in this subchapter".

2.5.2.1 Rectangular open-channels

"The secondary currents in closed air ducts have been measured by several researchers (...) using Hot Wire Anemometry (HWA), [Hot Film Anemometry (HFA)] and (...) Laser Doppler Anemometry (LDA). These results contributed to the future development of Algebraic Stress Model (ASM) and Reynolds Stress Model" (see Section 2.4).

Accurate measurements of secondary currents in rectangular open-channel flow have been carried out, measuring streamwise (u) and vertical (w) velocities using LDA and calculated transverse velocity (v) from the equation of continuity for fully developed flow, as Figure 2.14.

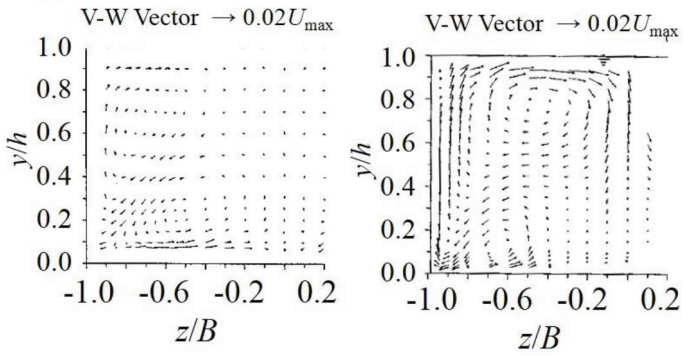

(a) Closed channel (b) Subcritical open Channel

Figure 2.14: Measured secondary-current velocity vectors at a section in: (a) closed duct; (b) open-channel. Adapted from Nezu (2005).

While secondary flow in a closed duct is symmetric, with two contra-rotating cells with regard to the corner bisector (Figure 2.14a), in open-channel flow two main secondary cells are observed. "Near the free surface ($z/h \geq 0.6$), a large scale secondary-current cell called "free-surface vortex" is generated which transports momentum and energy from the side wall towards the channel centre (Figure [2.14b]). At the channel bottom a smaller secondary cell called "bottom vortex" is formed which rotates in the opposite direction to the free-surface vortex" (Filonovich, 2015).

The cause for the velocity dip at the channel centre is the free-surface vortex due to the transport of momentum from the free surface to the mid-depth of the channel. Also, the pattern of the secondary flows depends on the aspect ratio, which leads to classifying the rectangular channels as narrow ($B/H < 5$) or wide ($B/H > 5$).

Further investigations on the secondary currents of rectangular channels using HFA to study the effects of geometry and wall roughness on the pattern of secondary currents. These studies revealed that the stream-wise velocity, turbulence intensities, Reynold stresses and boundary shear stress are all affected by secondary currents, and that the maximum value of the secondary flows was nearly equal to $0.015U_{max}$. Figure 2.15 shows the distribution of stream-wise velocity and secondary currents in rectangular open-channels.

Simulations of rectangular open-channels using ASM (Figure 2.16), backed by the experimental data in Figure 2.14, showed a strong free-surface vortex, "which transports high momentum from the water surface downwards, and a weak bottom vortex, which transports low momentum from near the walls, towards the channel centre. As the aspect ratio increases, the free-surface vortex becomes stronger and suppresses the lower bottom

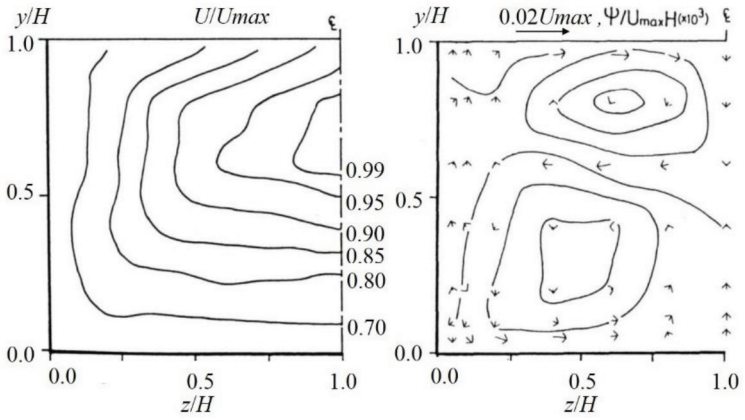

Figure 2.15: Isovels of stream-wise velocity and secondary currents in rectangular open-channel for aspect ratio 2. Adapted from Tominaga et al. (1989)

.

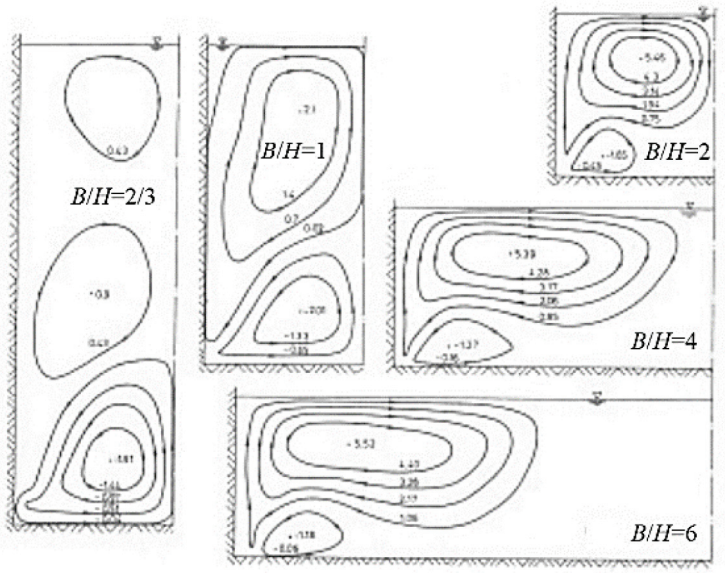

Figure 2.16: Calculated secondary current streamlines in open-channels under various aspect ratios. Adapted from Naot and Rodi (1982)

.

vortex. For aspect ratios below 2 the bottom vortex becomes dominant. When the aspect ratio is below 1, then the free-surface vortex splits into smaller and weaker vortices" (Filonovich, 2015).

Although many researchers have used ASM for the simulation of open-channel flows, the $k-\epsilon$ model has been the preferred choice, even though this model is unable to reproduce secondary flows.

Use of RSM model showed it to be able to predict the number and pattern of secondary flows, namely free-surface vortices and bottom vortices. A behaviour which was captured experimentally, and successfully numerically simulated using RSM, was how "with the

increase of the aspect ratio the free-surface vortex elongates until it separates into two contra-rotating vortices" (Filonovich, 2015).

Further studies conducted with the RSM turbulence model which showed some over-prediction of the position of maximum velocities for an aspect ratio of $B/H = 2$, with less satisfactory agreement between experimental and numerical studies for higher aspect ratios.

Further use of RSM models was given prevalence due to normal-stress anisotropy (as opposed to the isotropy of RANS models) being the driving force for the secondary currents (see Equation 2.86). Figure 2.17 illustrates the predicted (RSM) and measured secondary flow in rectangular open-channel by Cokljat and Younis (1995) and Figure 2.18 presents the predicted and measured contours of the stream-wise velocity field from Cokljat and Younis (1995) study of the effect of secondary flows on the primary velocity field.

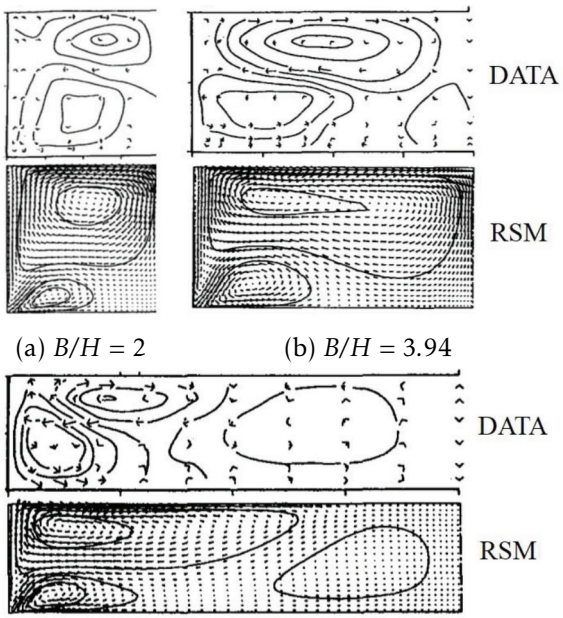

(a) $B/H = 2$ (b) $B/H = 3.94$

(c) $B/H = 8$

Figure 2.17: Predicted (RSM) and measured secondary flow in rectangular open-channel of differing aspect ratios (B/H). Adapted from Cokljat and Younis (1995).

In their study, Cokljat and Younis (1995) point out the shaded line in Figure 2.19, which is a zone where $\overline{v'v'}$ and $\overline{w'w'}$ are equal, having noticed that in closed ducts this line would lie along the corner bisector. "But the presence of the free surface in the model adds an asymmetry to the flow. The position of this shaded line predicted by the model matched the measured one, however some [over-prediction] was observed near the free surface" Filonovich (2015).

Further studies using RSM revealed the existence of inner secondary currents at the junction of the free surface and side wall. Albeit of small magnitude, about 1% of the

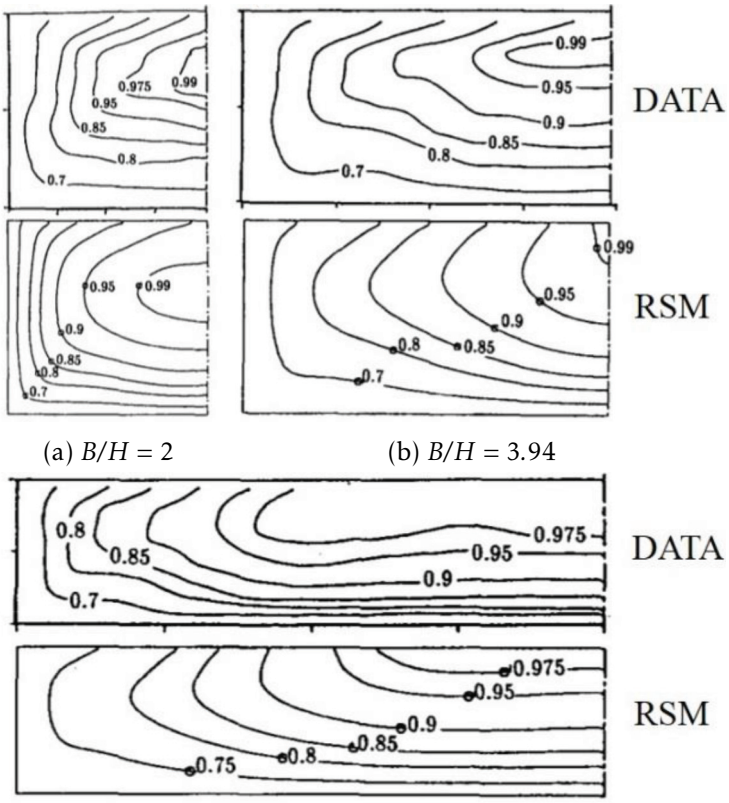

(a) $B/H = 2$ (b) $B/H = 3.94$

(c) $B/H = 8$

Figure 2.18: Contours of primary velocity for flow in rectangular open-channel of differing aspect ratios (B/H). Adapted from Cokljat and Younis (1995).

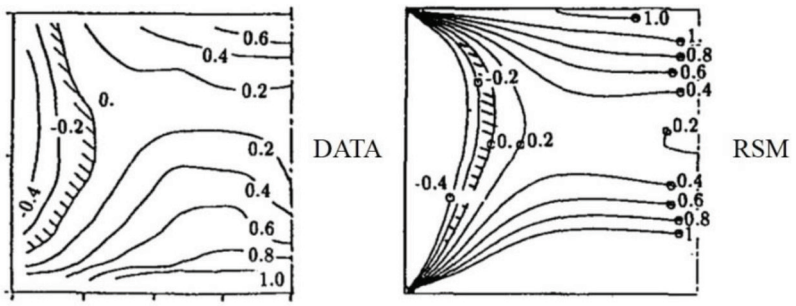

Figure 2.19: Predicted (RSM) and measured turbulence anysotropy for open rectangular channel with aspect ratio $B/H = 2$. Adapted from Cokljat and Younis (1995).

mean stream wise velocity, this small sized vortex still affects the mean flow and turbulence structures. The study by Kang (2006) focused on developing an RSM model capable of reproducing detailed mean flow and turbulence structure, including inner vortices, was able to reproduce an inner vortex not seen in other studies as shown in Figure 2.20, which depicts comparisons between Cokljat (1993), Kang (2006), Nezu et al. (1985), and Shi et al. (1999).

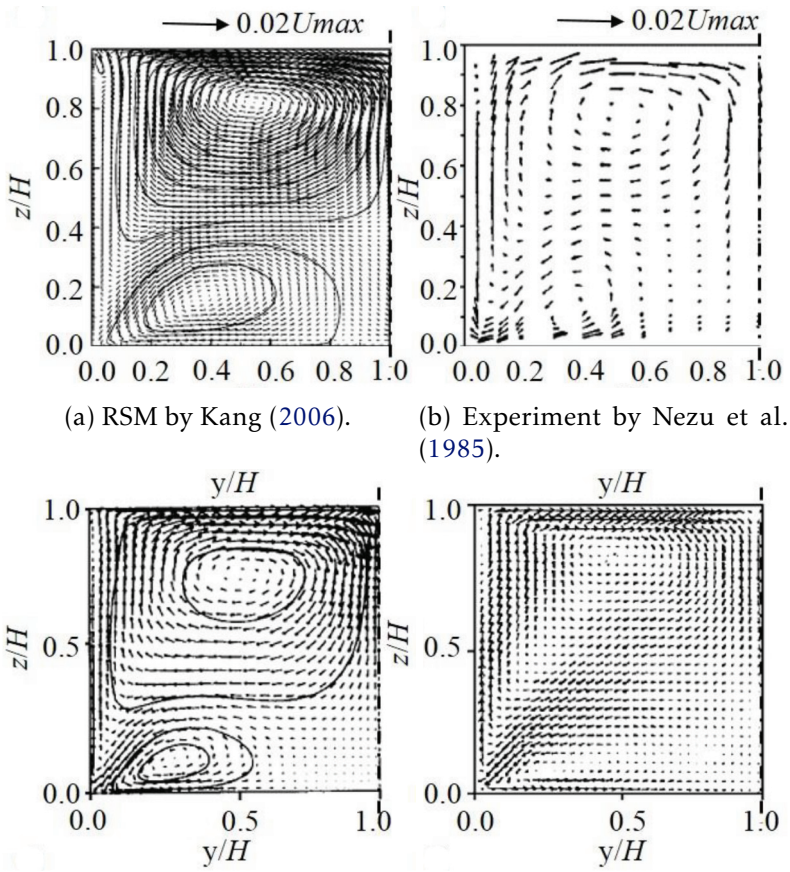

(a) RSM by Kang (2006).

(b) Experiment by Nezu et al. (1985).

(c) RSM by Cokljat (1993).

(d) LES by Shi et al. (1999).

Figure 2.20: Secondary current vectors in open-channel flow. Comparison between RSM (a and c) and LES (d) numerical studies and experimental study (2.20b). Adapted from Filonovich (2015).

2.5.2.2 Trapezoidal open-channels

Filonovich (2015) cites the work of Knight et al. (2005), Knight et al. (2007), and Tominaga et al. (1989) in describing trapezoidal open-channel flow (see Figure 2.21). The main conclusions that she draws from their work are that as the slide slope angle reduces, the free-surface vortex gets weaker and the bottom vortex expands, that there was no observable velocity dip phenomenon previously observed in rectangular channels, and that the maximum value of secondary currents was of the same magnitude as that in the rectangular channel.

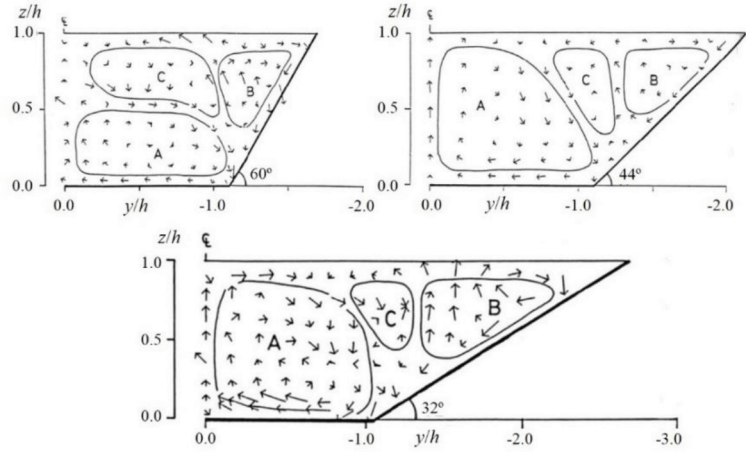

Figure 2.21: Secondary current vectors in smooth trapezoidal channels. Adapted from Tominaga et al. (1989).

Also, "the number of secondary cells in a simple trapezoidal channel depends on the aspect ratio $2b/H$ (for definition of b and H see Figure 2.24). For aspect ratios less than 2.2, three secondary current cells were observed; two of them were located at the side slope and one over the bottom of the channel. For $2b/H \geq 4$, the number of the secondary cells was found to be four, with two cells situated over the side slope and two over the flat bottom. The schematic representation of the pattern of the secondary current cells is presented in Figure 2.22.

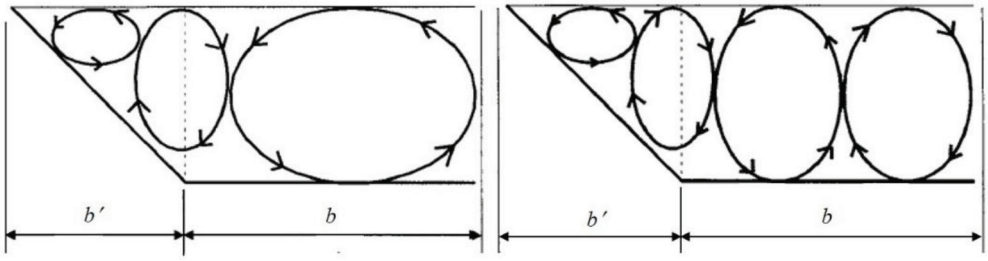

(a) $2b_C/H \leq 2.2$. (b) $2b_C/H \geq 4$

Figure 2.22: Secondary flow cells pattern in smooth trapezoidal channels with different aspect ratio $2b_C/H$. Adapted from Knight et al. (2007).

Knight et al. (2005) applied a state-of-the-art CFD workbench software to explore the physics within open-channel flows. In their research work they applied three different turbulent models, namely the $k-\epsilon$, Reynolds Stress model by Speziale, Sarkar and Gatski (SSG) by Speziale et al. (1991) and Reynolds Stress ω or Second Moment Closure - Omega Reynolds Stress Model (SMC-ω) (implemented in ANSYS-CFX) models to trapezoidal channel. The three models were compared with LES by Wright et al. (2004). The results reveal that $k-\epsilon$ did not show any recirculation, while some bulging of the velocity isovels was observed in the Speziale-Sarkar-Gatski pressure strain rate correlation turbulence model (SSG), and the bulging in the SMC-ω was found to be more prominent at the

middle of the side slope; the three secondary cells were present for the Reynolds stress models. However, there was no evidence of the velocity dip phenomenon.

To overcome this issue, a modified free surface boundary condition was applied in their study, (...), which yields a higher value for turbulent eddy dissipation and reduces turbulent kinetic energy near the free surface. The use of modified free surface boundary condition, affected the location of the secondary flows and the position of the bulging in SMC-ω was slightly shifted up than before [sic]. [SSG results verified] that the maximum velocity was beneath the water surface. The results from three models using the modified boundary condition are presented in Figure 2.23. The LES results showed a similar bulging of the isovels on the side slope of the trapezoidal channel as in the SMC-ω model. LES results also revealed and additional bulging near the bottom of the channel, and the magnitude of the v and w velocity components was greater than the results obtained by other models in [that] research"(Filonovich, 2015).

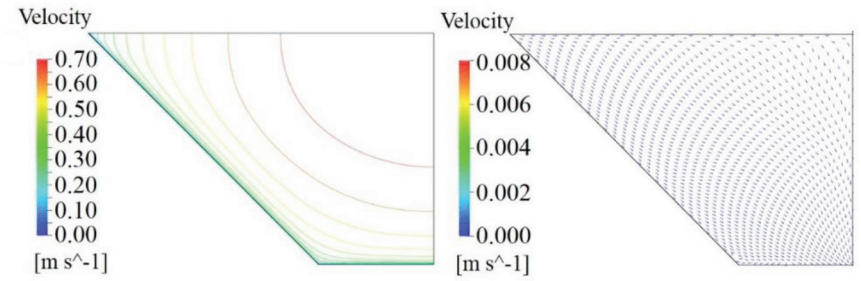

(a) $k-\epsilon$.

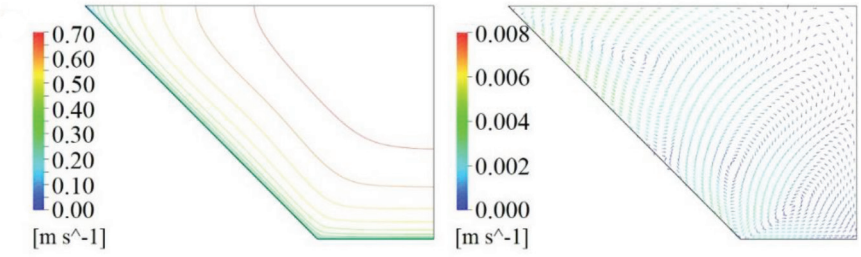

(b) SSG

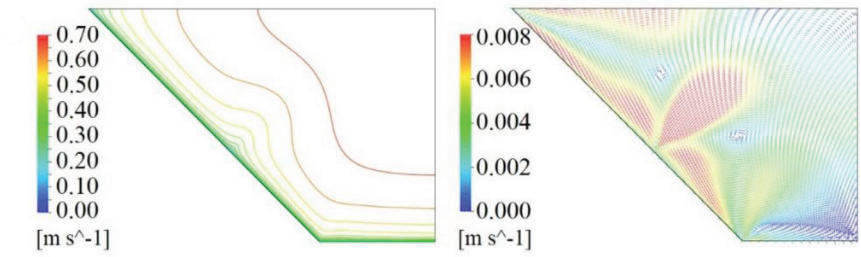

(c) SMC-ω

Figure 2.23: Velocity contours and secondary velocity vectors in smooth trapezoidal channels for different turbulence models. Adapted from Knight et al. (2005).

2.5.3 Flows in straight compound-channels

In this sub-section a heavily abridged description of Filonovich (2015) summary of compound open-channel flow is presented, focusing on symmetrical trapezoidal compound channels with a heavily summarized look into her analysis of rectangular compound channel flow.

"The complexity of turbulent structures in compound channel flow is higher than in a single rectangular or trapezoidal open-channel. The straight compound channels are classified into symmetric or asymmetric, and according to the shape of the cross section[,] into rectangular or trapezoidal.

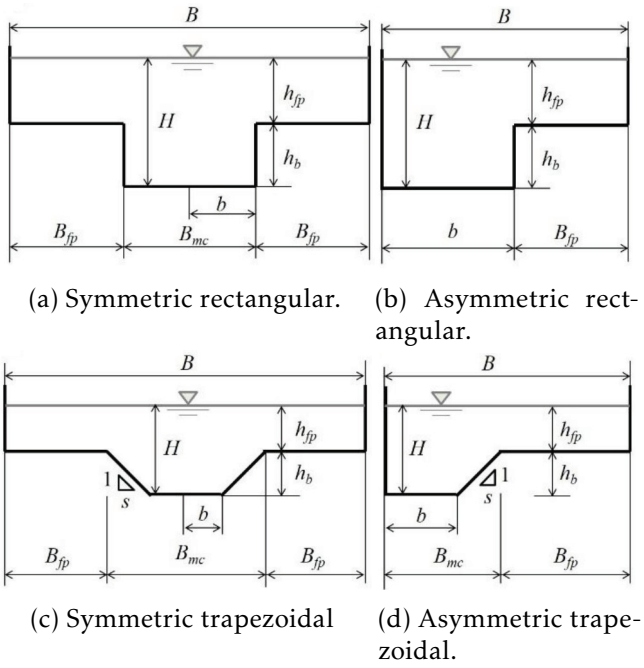

(a) Symmetric rectangular. (b) Asymmetric rectangular.

(c) Symmetric trapezoidal (d) Asymmetric trapezoidal.

Figure 2.24: Schematic representation of different types of compound channel configuration. Adapted from Filonovich (2015).

A schematic representation of compound channels and the geometric variables are presented in Figure 2.24, namely, the total channel width, B; the top main channel width, B_{mc}; the floodplain width, B_{fp}; the half of the main channel bottom width in symmetric channels and the main channel bottom width in asymmetric channels, b_C; and the side slope of the main channel $1 : s = vertical : horizontal$. Furthermore H and h_{fp} correspond to the main channel and the floodplain water depths, and h_b denotes the main channel bankfull height.

Figure 2.25 represents the typical hydraulic parameters and turbulent structures in symmetric prismatic compound channel (after Shiono and Knight (1991)). A strong lateral shear layer is present due to the difference between the faster flow in the deeper main channel and the slower flow in the shallower floodplain. This shear layer produces horizontal vortices with vertical axes at the edge between the main channel and the

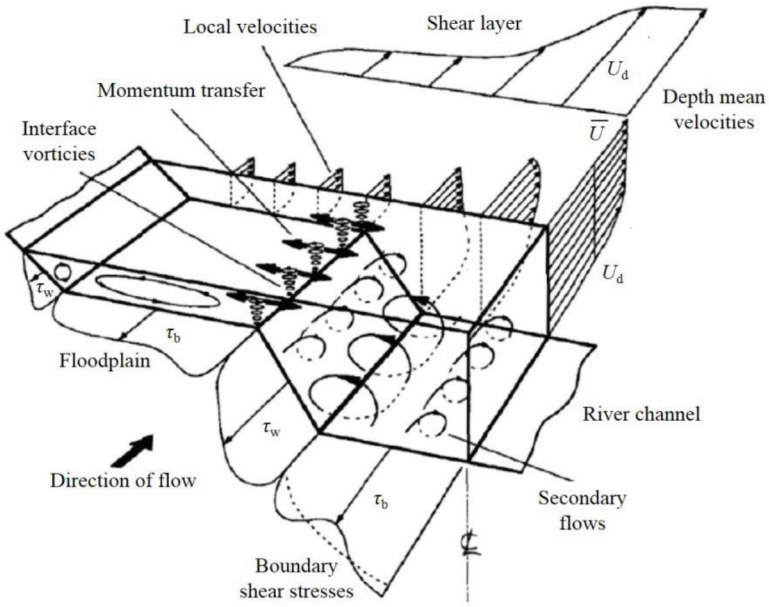

Figure 2.25: Hydraulic parameters associated with overbank flow in a trapezoidal compound channel. Adapted from Shiono and Knight (1991).

floodplain, which transport the high momentum fluid from the main channel towards the floodplain. (...). There are also streamwise vortices (Prandtl's second kind secondary flows [the mechanism of which is explained by Yang et al. (2012)]) with horizontal axes present in the main channel, which also contribute to the momentum exchange between the main channel and the floodplain.

Relative depth, $h_r = h_{fp}/H$, plays an important role in compound channel flows. Depending on the relative depth value, one form of the vortices may dominate another. Thus, for $h_r < 0.3$, the horizontal vortices are dominant, which can be extended to the entire width of the floodplain, even in natural rivers (...). For higher relative depths, that is, $h_r > 0.4$, the streamwise vortices tend to dominate the flow, thus making horizontal vortices smaller, as present in Figure 2.25" (Filonovich, 2015).

2.5.3.1 Rectangular compound-channels

"Much research has focused on rectangular compound channels. This type of channel has been studied by many researchers to understand the interaction mechanisms at the interface region between the main channel and the floodplain.

Myers (1978) measured the shear stress distributions across the entire cross-section of the compound channel using a Preston tube. He considered the entire cross-section in equilibrium and identified the acting forces. Taking into account a momentum balance separately in the main channel and in the floodplain, Myers (1978) identified an additional shear stress acting in the vertical interface between the main channel and the floodplain due to momentum transfer from the main channel to the floodplain and called

it apparent shear stress, τ_a. He also found that the apparent shear stress is higher at the lowest depth and suggested that the apparent shear stress may represent the intensity of the vorticity in the mixing region.

The apparent shear stress, τ_a, may be obtained by the integration over the width of a subsection, the floodplain (B_{fp}) of the main channel (B_{mc}), of the depth averaged momentum equation in the streamwise direction (which steams from the continuity equation [(Equation2.60)] by integrating over the flow depth). In the vertical interface between the main channel and the floodplain[,] τ_a is defined as (...):

$$\tau_a = -\rho\left(\overline{u_1' u_2'}\right)_d|_{B_{mc}} + \rho U_d V_d|_{B_{mc}} \qquad [\mathrm{N{\cdot}m^{-2}}] \tag{2.88}$$

The first RHS term of equation [2.88] represent the contribution of the shear layer to the overall stress in each subsection, and the second term represents the secondary flow contribution (...)" (Filonovich, 2015).

Based on several studies performed since then which made use of modern experimental techniques, Filonovich (2015) points these studies' conclusions.

In four cases, three with relative depths of $h_r = 0.25, 0.5, 0.75$ with smooth boundaries, and one relative depth of $h_r = 0.5$ with rough floodplain it was determined that for $h_r = \{0.25, 0.5\}$ "a pair of longitudinal vortices was recognised near the interface region, namely a main channel and a floodplain vortex, as well as a free surface vortex observed near the side wall of the main channel. For $h_r = 0.75$, the floodplain vortex appeared stronger and reached the free surface. They found that the magnitude of the secondary flows reaches approximately 4% of the maximum streamwise velocity. This magnitude is higher than the magnitude of secondary currents observed in the inbank case, which reaches typically $2-3\%$, (...). Turbulent intensities, Reynolds stresses and bed shear stress were also obtained. [TKE and anisotropy of turbulence were calculated with the results of turbulence intensities]. The TKE results revealed that the total magnitude of turbulence increases in the vicinity of the interface between the main channel and the floodplain. The anisotropy of turbulence determines the structure of secondary currents driven by turbulence showing a complicated behaviour near the junction. [It was also determined that roughened floodplains did not affect the structure of secondary currents].

(...)

Nezu et al. (1999)[,] using LDA and Particle Image Velocimetry (PIV) measurements[,] studied further the pattern and the strength of the coherent horizontal vortices for various relative depths between 0.16 and 0.67. They found that for relative depths higher than 0.375, a pair of horizontal vortices is observed near the junction. For lower h_r, a unique horizontal vortex develops at the interface region between the main channel and the floodplain" (see Figure 2.26) (Filonovich, 2015).

The first numerical study by Keller and Rodi (1988) which made use of the $k-\epsilon$ model incorporated a two-dimensional depth-averaged form of this turbulence model in a numerical study to predict flow characteristics in compound channels (both symmetric and

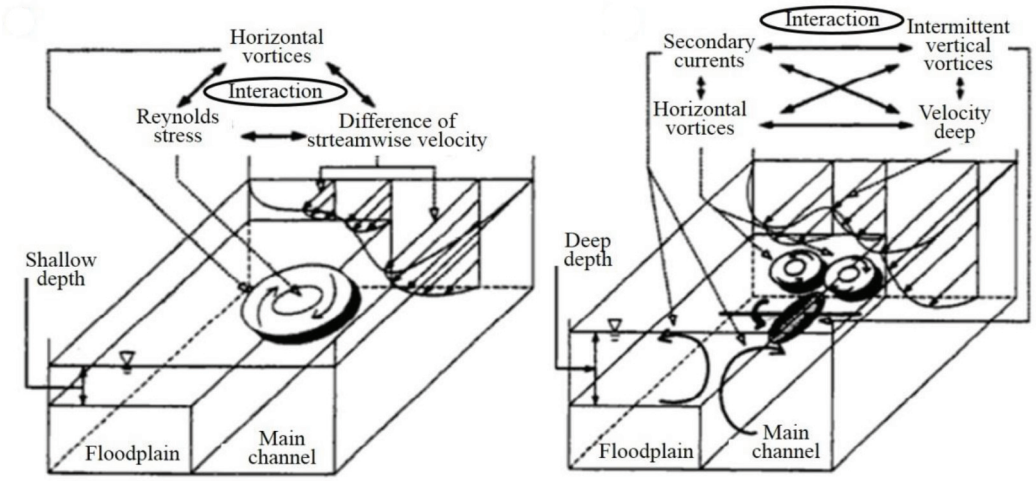

(a) Shallow depth flow.

(b) Deep depth flow.

Figure 2.26: Schematic representation of flow field in varying rectangular compound channel relative depth. Adapted from Nezu et al. (1999).

asymmetric) and compared to experimental studies found that the agreement between both numerical and experimental studies was generally quite good. However, there was some deviation in the interaction region from the experimental data which was attributed to the under-prediction of transverse mixing in regions with an abrupt change in depth which could not be correctly accounted for in the model that was used.

In this study "the non-linear $k-\epsilon$ model, first proposed by Speziale (1987), [was] employed to predict secondary currents in compound channel flows by Lin and Shiono (1995), Pezzinga (1994), and Sofialidis and Prinos (1998). The latter used a low-Reynolds non-linear $k-\epsilon$ model. Although these models successfully predicted both streamwise velocity and the secondary currents, especially the two vortices generated at the interface between the main channel and the floodplain, they could not accurately simulate the velocity-dip phenomenon. The non-linear $k-\epsilon$ model did not predict correctly the strength of the secondary currents. The measured and predicted isovels of the streamwise velocity are presented in Figure [2.27]" (Filonovich, 2015).

Further studies are described by Filonovich (2015) which take into make use of the $k-\epsilon$, ASM, RSM and LES turbulence models to study not only flow in compound channels but also solute transport in a compound channel. These varying studies reinforced the findings of the impact of secondary flows in accurately predicting flow velocities and Reynold stresses. The $k-\epsilon$ model proved to be the least reliable due to its inability to account for secondary flows. The ASM model, although able to reproduce secondary flows, was not as accurate as RSM. LES studies also revealed not to be as reliable as RSM whilst also being more computationally expensive to run.

"Cokljat and Younis (1995) applied their RSM to symmetric and asymmetric compound channels. The experimental data from Tominaga and Ezaki (1988) and Tominaga

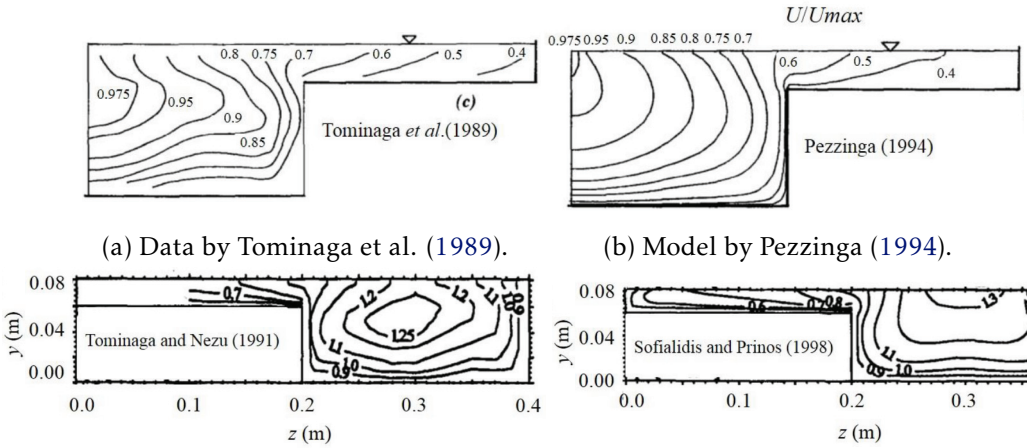

(a) Data by Tominaga et al. (1989).

(b) Model by Pezzinga (1994).

(c) Data by Tominaga and Nezu (1991).

(d) Model by Sofialidis and Prinos (1998). Adapted from Pezzinga (1994) and Sofialidis and Prinos (1998).

Figure 2.27: Experimental and computed stream-wise velocity contours. Adapted from Filonovich (2015).

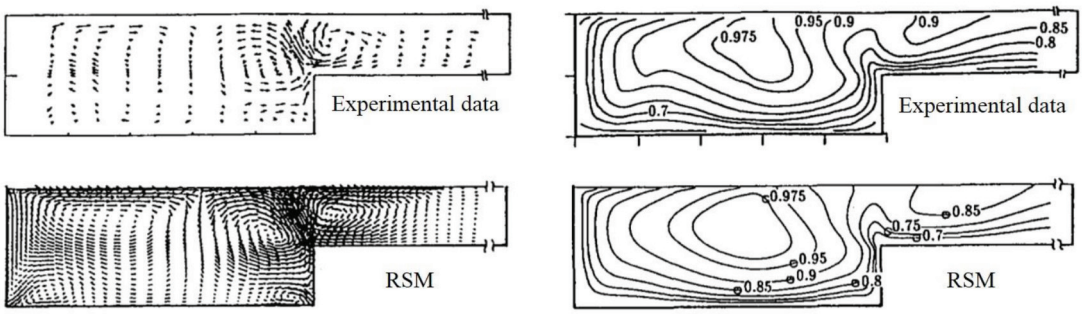

Figure 2.28: Secondary current vector plots and primary velocity contour plots in asymmetric compound channels for $h_r = 0.5$. Adapted from Cokljat and Younis (1995).

et al. (1989) were used for the model validation. It was found that RSM captured the secondary curents and even smaller vortices. The position, where free surface and main channel vortices [meet], was predicted almost exactly by the model. The effect that the secondary currents have on the primary flow was well predicted, where a significant bulging of the isovels at the junction between the main channel and the floodplain was present (see Figure 2.28). The velocity-dip phenomenon was captured by the RSM. Cokljat and Younis (1995) suggested that the latter was not reproduced in the work of Naot et al. (1993) due to the [under-prediction] of the levels of turbulence anisotropy by that model. They also compared the predicted an measured boundary shear stress distribution for the symmetric compound channel. The correspondence was fairly satisfactory, especially for the floodplain, where the RSM reproduced the waviness of the experimental data. The variation of the total discharge with different relative depths was well predicted" (Filonovich, 2015).

Other RSM studies further showed that "the secondary currents at the junction between the main channel and floodplain become weakened as the relative depth decreases. This aspect is reflected in the angle of inclination of the [up-flow] at the junction, which increases with decreasing relative depth (Kang and Choi, 2006). For shallow, flow h_r, the vertical structure in the main channel becomes similar to that observed in the rectangular channel ([see Figure 2.20]). The main channel vortex increases its intensity and the floodplain vortex decreases with the decrease of the relative depth. Kang and Choi (2006) also compared the wall shear stress distribution and concluded that the RSM overestimates bottom shear stress in the main channel. However, in the floodplain, the simulated bottom shear stress was in a good agreement with the experimental data" (Filonovich, 2015).

Using results from previous studies which had used the Shiono and Knight Method, and with the implementation of an LES turbulence model to study the effects of the floodplain depth on the flow in an asymmetric compound channel of two relative depths , $h_r = \{0.25, 0.5\}$, Kara et al. (2012) obtained good results and "demonstrated the anisotropy in [a] compound channel at the interface between the main channel and the floodplain leads to the formation of a vortex pair. The apparent shear stress (see Eq. [2.88]) was greater for the shallow floodplain case. The generation term (first RHS term in Eq. [2.86]) was found to be more significant at the interface for the shallow case, where the peak values extend to the free surface. The authors suggest that the extent and magnitude of the secondary current generation term influences the angle of inclination of secondary currents" (Filonovich, 2015).

Another LES study by Xie et al. (2013) revealed that stronger turbulent flow occurs in the near-wall region and a significant lateral transport of momentum is present.

2.5.3.2 Trapezoidal compound-channels

Based on the experimental data obtained by several studies at the Science and Engineering Research Council (SERC) Flood Channel Facility (FCF), several experimental and numerical studies have been conducted over the past three decades. One of the first of these studies "was the work presented by Knight and Shiono (1990). This study includes highly accurate measurements of the primary velocity, the turbulent intensities, TKE and the Reynolds stresses. One of the main conclusions of their study was the significance of the secondary currents contribution to the lateral transfer of momentum despite their small values. Longitudinal vortices have been found by those authors to be important for relative depths as low a 0.25. The vertical distributions for the shear stress τ_{zu} was found to be highly non-linear in the interface zone, indicating strong secondary [current] development. With an increase of the relative depth, the spreading of the shear layer into the floodplain decreases" (Filonovich, 2015). In her literature review Filonovich (2015) concludes that "besides DNS, much more complex models, such as LES, are necessary for simulating the fully 3D multi-scale phenomena in open-channel flows. However, despite

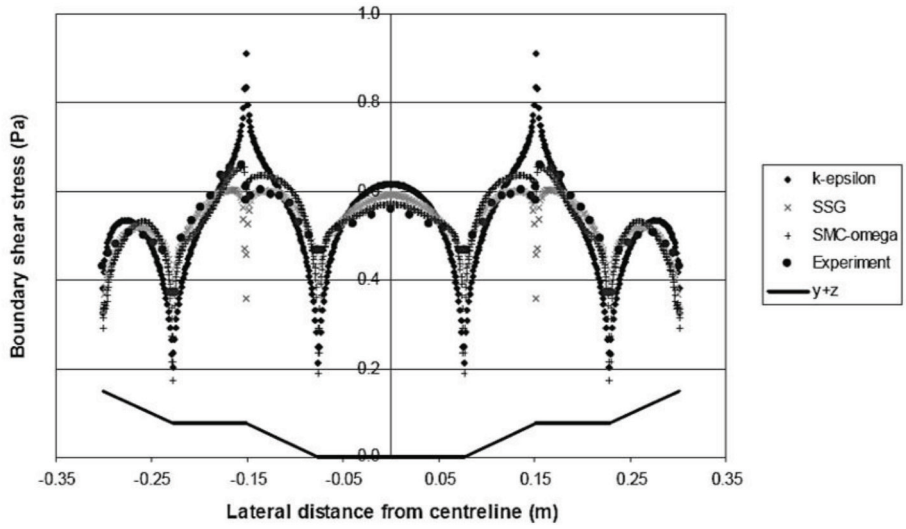

Figure 2.29: Boundary shear stress in symmetric compound channel with trapezoidal cross-section. Adapted from Knight et al. (2005).

the fact that LES produces accurate results, it increases computational cost further beyond typical engineering time and resource framework, which often leads to rejection of this method. Thus, a compromise is needed between capturing the complexity of anisotropic 3D secondary flows with accuracy" whilst keeping computational costs low.

In highlighting the flow complexity of compound open-channels she cites the work of Knight et al. (2005) who used state-of-the-art commercial CFD workbench software having tested $k-\epsilon$, SSG and SMC-ω models and comparing the results with experimental data by Yuen (1989). Both models, SSG and SMC-ω, predict the presence of four secondary cells where the strongest is located about the junction between the main-channel and the floodplain. In the case of bed boundary shear stress distribution, the SMC-ω prediction were in the closest match to the experimental data ([see Figure 2.29]). The authors have noticed that the predicted mass flow rate was higher than the experimental value. This is due to the fact that whilst the experiments were considered with relatively smooth walls, there was still some roughness to account for. This was reflected in CFD simulation though applying a small roughness (0.5 mm) in the cases of $k-\epsilon$ and SSG model. The introduction of roughness did not have any impact on the velocity contours or the boundary shear stress profiles. The $k-\epsilon$ model failed in predicting secondary currents and overestimated the boundary shear stress. The main conclusions from this research work has been that there are limitations as to what can be achieved with a turbulence model in the case of steady uniform flow. (Filonovich, 2015).

2.5.4 Vegetated compound channel flow

When analysing the overall flow characteristics of vegetated compound channels Terrier (2010) remarks that the "drag exerted by fluid on vegetation has a significant impact on the flow characteristics of a compound channel. The mean flow of vegetated areas is reduced

when compared to non vegetated areas while the flow depth can also increase (e.g. Darby (1999)". However, the rest of his characterisation of compound channel vegetated flow is focused on the effects of emergent vegetation, for which the porous media approach is not valid.

Brito et al. (2016) succinctly summarizes the effects of submerged vegetation on open-channel flows: "The vegetation affects significantly the flow hydrodynamics, changing its mean velocity, depth and shear stresses (...). In such vegetated flows, both the geometry of the vegetation elements (shape, size, flexibility and vegetation density) and flow patterns affects significantly the flow hydrodynamic resistance (...). The vegetation increases the flow resistance and depth, consequently, decreases the mean flow velocity (...). Due to flow resistance increase, a reduction in shear stresses and in turbulence intensities is also observed near the channel bottom (...). The conversion of mean kinetic energy to turbulent kinetic energy within vegetation elements wakes augments the turbulence intensity, and because wake turbulence is generated at the vegetation elements scale, the dominant turbulent length scale is shifted downward, relative to the non-vegetated open-channel. The combination of reduced velocities and eddy-scale should reduce the macroscale diffusion in the vegetated relative to non-vegetated regions. This reduction has been observed for aquatic grasses (...). A large scale coherent vortex is generated near the vegetation edge, which dominates the momentum and scalar transport".

Chapter 3

Modelling approach

In this chapter a brief introduction to the tools and mathematical models used in simulating the various cases will be presented. It is by no means supposed to be a comprehensive guide in the fundamentals of these tools and methods, but merely a brief introduction and reference to customizing them to process the case studies in this work. Special attention should be taken in regards to references to *files* and *folders*, **solvers** and **utilities**, and `source code` presented in numbered Listings.

3.1 Introduction to OpenFOAM

According to its user guide (CFD Direct, 2014), OpenFOAM "is first and foremost a *C++ library*, used primarily to create executables, known as *applications*. The applications fall into two categories: **solvers**, that are each designed to solve a specific problem in continuum mechanics; and **utilities**, that are designed to perform tasks that involve data manipulation. The OpenFOAM distribution contains numerous solvers and utilities covering a wide range of problems, (...).

One of the strengths of OpenFOAM is that new solvers and utilities can be created by its users with some pre-requisite knowledge of the underlying method, physics and programming techniques involved. OpenFOAM is supplied with pre- and post-processing environments. The interface to the pre- and post-processing are themselves OpenFOAM utilities, thereby ensuring consistent data handling across all environments. The overall structure of OpenFOAM is shown in Figure 3.1".

Like most other CFD software solutions, it is Finite Volume Method (FVM) based, which "is a numerical technique that transforms the partial differential equations representing conservation laws over differential volumes into discrete algebraic equations over finite volumes (or elements or cells). In a similar fashion to the Finite Difference (FD) or

Finite Element Method (FEM), the first step in the solution process is the discretisation of the geometric domain, which, in the FVM, is discretized into non-overlapping elements or finite volumes. The partial differential equations are then discretised/transformed into algebraic equations by integrating them over each discrete element. The system of algebraic equations is then solved to compute the values of the dependent variable for each of the elements.

In the finite volume method, some of the terms in the conservation equation are turned into face fluxes and evaluated at the finite volume faces. Because the flux entering a given volume is identical to that leaving the adjacent volume, the FVM is strictly conservative. This inherent conservation property of the FVM makes it the preferred method in CFD. Another important attribute of the FVM is that it can be formulated in the physical space on unstructured polygonal meshes. Finally in the FVM it is quite easy to implement a variety of boundary conditions in a non-invasive manner, since the unknown variables are evaluated at the centroids of the volume elements, not at their boundary faces" (Moukalled et al., 2016).

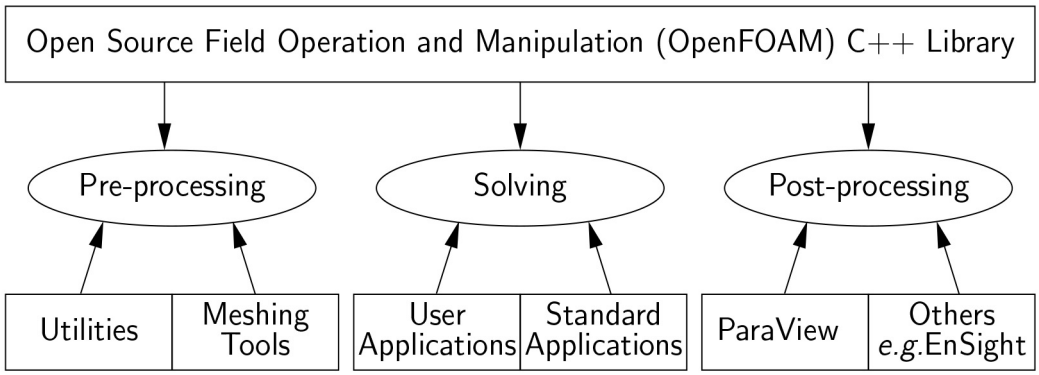

Figure 3.1: Overview of OpenFOAM structure. Adapted from (CFD Direct, 2014).

In Higuera Caubilla (2017), a brief description of the major branches of OpenFOAM is presented and illustrated (Figure 3.2).

The simulation work done in this thesis was all done using the main OpenFOAM branch maintained by the "The OpenFOAM Foundation".

One of the biggest advantages of using one of these distributions is in keeping costs down, as there are no licenses to be purchased and so the software can be installed and run on varying computer platforms that may be available to the user.

Case studies are put together in case folder which typically have a basic structure as per Figure 3.3. All files in black text are required files to set-up a working case for the **porousSimpleFoam** solver. The *0* folder is the first time step where all variables are initialized. The red coloured text files are not all required, but have to be set up according to the chosen turbulence model, which is specified in the *constant/RASproperties* file. In the *transportProperties* file the fluid properties are set, in the case of this particular solver only by specifying its kinematic viscosity, ν.

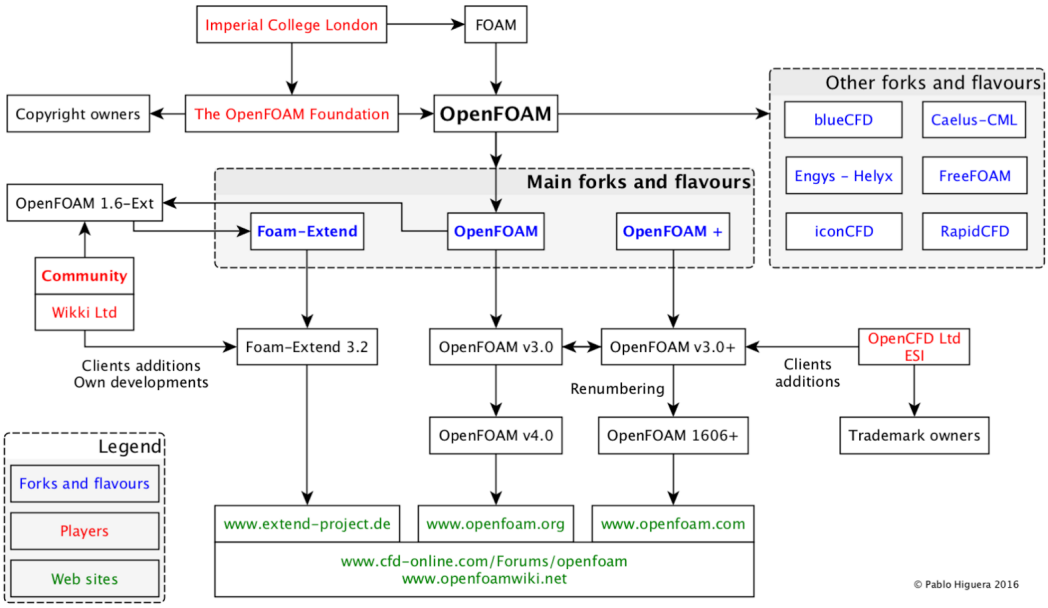

Figure 3.2: Simplified overview of OpenFOAM distribution hierarchy. Adapted from Higuera Caubilla (2017). Used with permission.

The *system* folder contains the following files, as described in CFD Direct (2014):

controlDict The control dictionary file is where the simulation parameters, such as run time and time step, are configured. "The OpenFOAM solvers begin all runs by setting up a database. The database controls I/O and, since output of data is usually requested at intervals of time during the run, time is an inextricable part of the database. The *controlDict* dictionary sets input parameters essential for the creation of the database".

fvSchemes Here we set the numerical schemes for terms, such as derivatives in equations, that are calculated during a simulation. "The terms that must typically be assigned a numerical scheme in `fvSchemes` range from derivatives, e.g. gradient ∇, to interpolations of values from one set of points to another. The aim in OpenFOAM is to offer an unrestricted choice to the user, starting with the choice of discretisation practice which is generally standard Gaussian finite volume integration. Gaussian integration is based on summing values on cell faces, which must be interpolated from cell centres. The user has a wide range of options for interpolation scheme, with certain schemes being specifically designed for particular derivative terms, especially the advection divergence $\nabla\cdot$ terms".

fvSolutions The equation solvers, tolerances and algorithms are controlled from the *fvSolution* dictionary. It's in this file that the solvers, algorithms and under-relaxation factors are set. "In general the *fvSolution* dictionary may contain any parameters

to control the solvers, algorithms, or in fact anything. If any parameter or sub-dictionary is missing when an solver is run, it will terminate, printing a detailed error message. The user can then add missing parameters accordingly".

decomposeParDict This is an optional file not necessary to run the solver, but necessary if we wish to distribute the case for running in parallel across multiple processors or processor cores. "The method of parallel computing used by OpenFOAM is known as domain decomposition, in which the geometry and associated fields are broken into pieces and allocated to separate processors for solution. The process of parallel computation involves: decomposition of mesh and fields; running the application in parallel; and, post-processing the decomposed [or recomposed] case. The parallel running uses the public domain openMPI implementation of the standard message passing interface Message Passing Interface (MPI) [(Forum, 1994)] by default, although other libraries can be used.

(...)

The mesh and fields are decomposed using the **decomposePar** utility. The underlying aim is to break up the domain with minimal effort but in such a way to guarantee an economic solution". The finished case can then be recomposed back together with the use of the **recomposePar** utility.

In Chapter 4, the section on experimental and numerical characterisation includes the customised case parameters which were were added to the modified *angledDcutExplicit* tutorial case.

3.2 Complementary tools for pre- and post-processing

As mentioned in the previous subsection, OpenFOAM is distributed with a set of pre- and post-processing tools which are customized to work with the accompanying version of the program. Some of these tools and utilities can be somewhat daunting for first time users given that they are run by command line instructions, their behaviour determined by a simple dictionary file where parameters are set.

Mesh generation can be accomplished with the use of established mesh software solutions and subsequently converted into OpenFOAM format with the use of the corresponding utility. Open source programs with a Graphical User Interface (GUI) such as Gmsh (Geuzaine and Remacle, 2009), or the more comprehensive SALOMÉ (Ribes and Caremoli, 2007) can be used for both pre-processing of a case mesh and post-processing, as well as visualisation of results. The included **ParaFOAM** utility, which is a customized version of the open-source ParaView program (Hansen and Johnson, 2005), can also be used for visualisation and data post processing. One isn't bound to open-source solutions alone, with established commercial software such as Tecplot 360 or EnSight also providing utilities for post-processing and visualization of results, and many other commercial

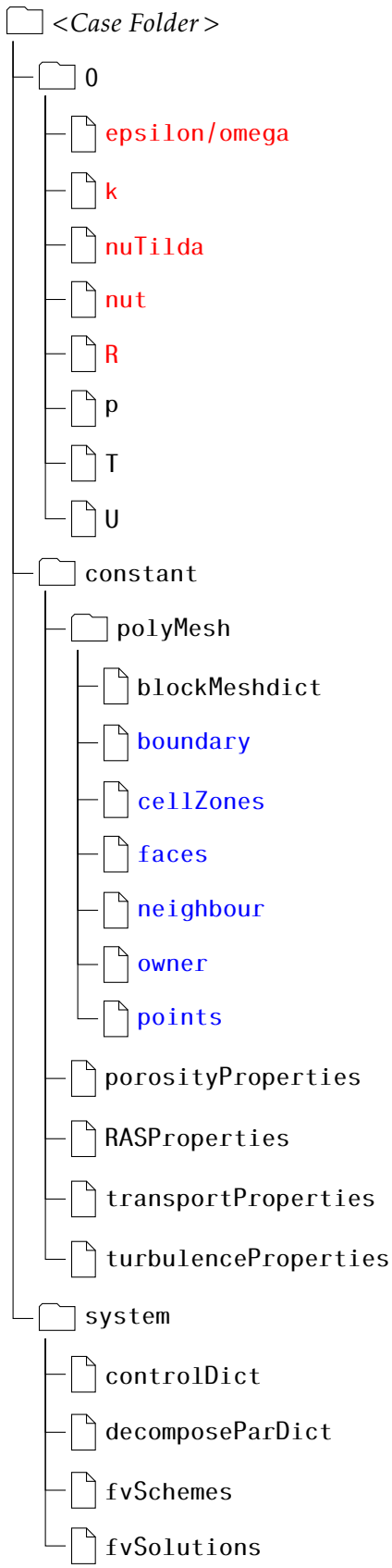

Figure 3.3: **porousSimpleFoam** case structure.

Computer Aided Design (CAD) solutions capable of generating STereoLithography file format (STL) files being capable of generating models for mesh creation. To import externally created meshes there are other utilities included with OpenFOAM in order to import meshes generated in popular commercial and open-source CFD solutions.

Given that the geometries in this work were relatively simple and straightforward, the meshing tool of choice was the **blockMesh** utility supplied with OpenFOAM. "The **blockMesh** utility creates parametric meshes with grading and curved edges. The mesh is generated from a dictionary file name ***blockMeshDict*** located in the ***constant/polyMesh*** directory of a case. **blockMesh** reads this dictionary, generates the mesh and writes out the mesh data to ***points*** an ***faces***, ***cells*** and ***boundary*** files in the same directory [(shown in blue text in Figure 3.3)].

The principle behind blockMesh is to decompose the main geometry into a set of 1 or more three dimensional, hexahedral blocks. Edges of the blocks can be straight lines, arcs or splines. The mesh is ostensibly specified as a number of cells in each direction of the block, sufficient information for **blockMesh** to generate the mesh data" (CFD Direct, 2014).

Other relevant tools include the pre-processing tool **topoSet** that operates on ***cellSets/faceSets/pointSets*** through a dictionary to, amongst other things, define a porous zone in a mesh after it has already been compiled. There are also post-processing tools such as **yPlusRAS**, which calculates and reports y^+ for all wall patches, for the specified times when using Reynolds-Averaged Simulation (RAS) turbulence models, and the **postChannel** utility, which post-processes data from channel flow calculations.

3.3 The porousSimpleFoam solver

The **porousSimpleFoam** solver is the **simpleFoam** single-phase, steady-state solver for turbulent flow of incompressible fluids with implicit or explicit porosity treatment. In the tutorial Hafsteinsson (2009), although originally describing the **rhoPorousSimpleFoam** based on **rhoSimpleFoam** (the compressible fluid version of the **simpleFoam** solver), the implicit porosity solver is described as meant to be "more robust and is needed if the resistances are large, heavily anisotropic or not aligned with the global coordinates". The implicit porosity treatment can be activated by simply adding the line "*nUCorrectors 2*;" to the *SIMPLE* field in the *system/fvSolutions* file.

It is based on the **simpleFOAM** solver, with merely having the porosity zones and Multiple Reference Frame (MRF) functionality included by default in its default configuration, thus not having to add it to an *fvOptions* file. It also makes it possible to choose between an explicit and implicit porosity treatment. The SIMPLE loop illustrated in Figure 3.4 is applied in the $*FOAM_APP/solvers/incompressible/simpleFoam/simpleFoam.C* file (and *porousSimpleFoam.C* file on the **porousSimpleFoam** sub-folder) as per Listing 3.1. For a detailed explanation of the collocated SIMPLE algorithm in OpenFOAM, consult Jasak (1996), Moukalled et al. (2016), and OpenFOAMWiki (2014).

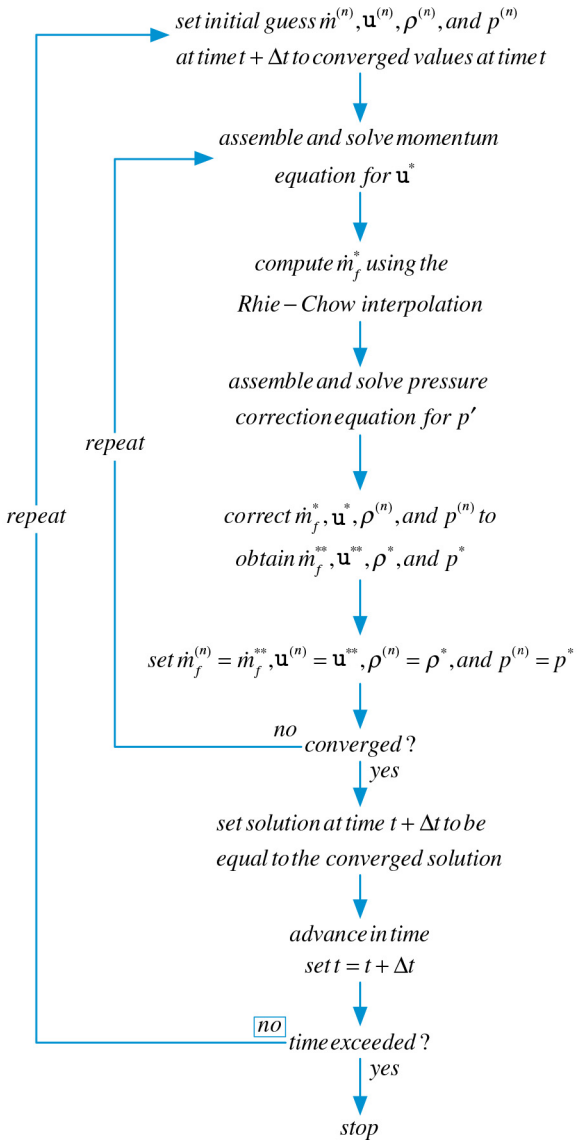

Figure 3.4: A flow chart of the SIMPLE algorithm. Adapted from Moukalled et al. (2016).

The condition for the main loop is defined by the `simple.loop()` object and function (see Nilsson (2016a) and Nilsson (2016b) for the basics of C++ and its use in OpenFOAM). It then includes in the loop the *UEqn.h* and *pEqn.h* header files which contain the velocity and pressure equations, respectively.

In the **porousSimpleFOAM** solver, these files already contain `if, else` conditions to specify the equations for either implicit or explicit porosity treatment, as shown in Listings 3.3 and 3.4.

Listing 3.1: Code for setting up the collocated SIMPLE loop as per Figure 3.4 in the *simpleFoam.C* file.

```
Info<< "\nStarting time loop\n" << endl;

    while (simple.loop())
    {
        Info<< "Time = " << runTime.timeName() << nl << endl;

        // --- Pressure-velocity SIMPLE corrector
        {
            #include "UEqn.H"
            #include "pEqn.H"
        }

        turbulence->correct();

        runTime.write();

        Info<< "ExecutionTime = " << runTime.elapsedCpuTime() << " s"
            << "  ClockTime = " << runTime.elapsedClockTime() << " s"
            << nl << endl;
    }

    Info<< "End\n" << endl;
```

3.4 Porous media flow in OpenFOAM

Despite the complexity of the OpenFOAM tool-box and its applicability to many CFD studies on par with many commercial software solutions, its application of porosity models still lacks some of the more intricate considerations, namely those mentioned in subsection 2.3.5, having only a somewhat more classical implementation of porous media.

This implementation will be described in this sub-section.

3.4.1 Governing equations

The classic formulations of porosity and their corresponding equations are addressed in Sub-section 2.3.4. In OpenFOAM, porous media is modelled "by attenuating the time derivative and adding a sink term to the Navier-Stokes equations" (Hafsteinsson, 2009)

$$\frac{\partial}{\partial t}(\rho u_i) + u_j \frac{\partial}{\partial x_j}(\rho u_i) = -\frac{\partial p}{\partial x_i} + \mu \frac{\partial \tau_{ij}}{\partial x_j} + S_i \tag{3.1}$$

The source term, S_i, is the Darcy-Forchheimer equation as per Equation 2.38, but formulated slightly different:

$$S_i = -\left(\mu D_{ij} + \frac{1}{2}\rho |u_{kk}| F_{ij}\right) u_i \tag{3.2}$$

In the case of isotropic porous media (homogeneous), we get:

$$S_i = -\left(\mu D + \frac{1}{2}\rho |u_{kk}| F\right) u_i \tag{3.3}$$

where D_{ij} and F_{ij} are represented as the scalars D and F, which when comparing Equation 3.3 to Equation 2.38, can be defined as:

$$D = \alpha = \frac{1}{K} \qquad [\mathrm{m}^{-2}] \tag{3.4}$$

and:

$$F = \beta = \frac{1}{\eta_p} \qquad [\mathrm{m}^{-1}] \tag{3.5}$$

As indicated in line 17 of Listing 3.2, "leading 0.5 is from 1/2*rho", and does not affect the value of F.

3.4.2 The class

The porous media models source files in OpenFOAM-2.x.x are located in the directory $*FOAM_SRC/finiteVolume/cfdTools/general/porosityModel/* directory, with the *DarcyForchheimer* model directory having the structure as per Figure 3.5.

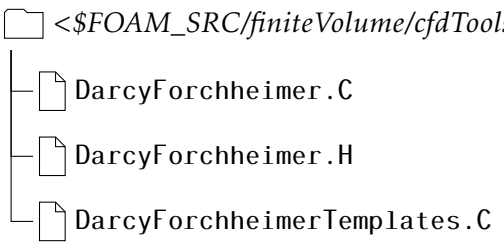

Figure 3.5: `DarcyForchheimer` source code folder structure.

The implementation of the porosity equations is found in the *DarcyForchheimerTemplates.C* file and the D and F constants values are read in *DarcyForchheimer.C* as per Listing 3.2.

3.4.3 The solver

The **porousSimpleFOAM** solver source code is located inside the **simpleFOAM** solver directory in: $*FOAM_APP/solvers/incompressible/simpleFoam/*. The directory tree is as in Figure 3.6.

As explained in Hafsteinsson, 2009, and updated for OpenFOAM-2.x.x, in *UEqn.H* (Listing 3.3) the momentum equation is constructed (lines 3 to 8) and the source term, S_i, is added by calling the member function `pZones.addResistance(UEqn())`.

3.4.4 The case

To make use of porous zones in **porousSimpleFOAM**, we must first define which zones in our mesh are to receive the porosity treatment. This can be done before meshing, by specifying an internal volume with a different name (usually this zone is simply called

Listing 3.2: Code for reading of D and F coefficients with global coordinate system in *DarcyForchheimer.C* file.

```
porosity1
{
if (coordSys_.R().uniform())
    {
        forAll (cellZoneIDs_, zoneI)
        {
            D_[zoneI].setSize(1);
            F_[zoneI].setSize(1);

            D_[zoneI][0] = tensor::zero;
            D_[zoneI][0].xx() = dXYZ_.value().x();
            D_[zoneI][0].yy() = dXYZ_.value().y();
            D_[zoneI][0].zz() = dXYZ_.value().z();

            D_[zoneI][0] = coordSys_.R().transformTensor(D_[zoneI][0]);

            // leading 0.5 is from 1/2*rho
            F_[zoneI][0] = tensor::zero;
            F_[zoneI][0].xx() = 0.5*fXYZ_.value().x();
            F_[zoneI][0].yy() = 0.5*fXYZ_.value().y();
            F_[zoneI][0].zz() = 0.5*fXYZ_.value().z();

            F_[zoneI][0] = coordSys_.R().transformTensor(F_[zoneI][0]);
        }
}
```

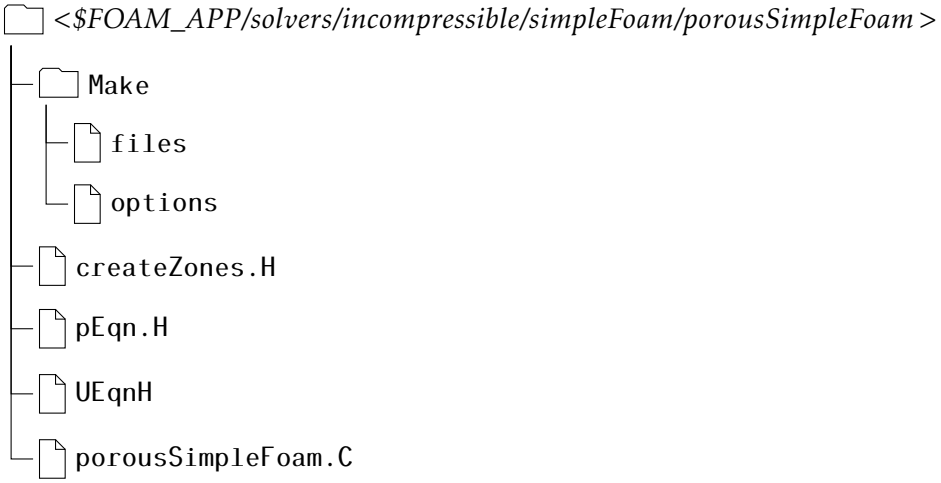

Figure 3.6: **porousSimpleFOAM** source code folder structure.

Listing 3.3: *UEqn.H* file structure with implicit porosity treatment section omitted.

```
1  porosity1
2  {
3      tmp<fvVectorMatrix> UEqn
4      (
5          fvm::div(phi, U)
6        + turbulence->divDevReff(U)
7        ==
8          fvOptions(U)
9      );
10
11     mrfZones.addCoriolis(UEqn());
12
13     UEqn().relax();
14
15     // Include the porous media resistance and solve the momentum equation
16     // either implicit in the tensorial resistance or transport using by
17     // including the spherical part of the resistance in the momentum diagonal
18
19     tmp<volScalarField> trAU;
20     tmp<volTensorField> trTU;
21
22     if (pressureImplicitPorosity)
23     {
24         (...)
25     }
26     else
27     {
28         pZones.addResistance(UEqn());
29
30         fvOptions.constrain(UEqn());
31
32         solve(UEqn() == -fvc::grad(p));
33
34         fvOptions.correct(U);
35
36         trAU = 1.0/UEqn().A();
37         trAU().rename("rAU");
38 }
```

porosity #, where # is a number if there is to be more than one porous zone) from the unobstructed flow volumes, or after meshing by use of the **topoSet** utility.

The porosity properties are then defined in the the file *constant/porosityProperties* (Figure 3.3 and Listing 3.5, which is particular to this solver. Other solvers that accept porous zones will usually have the porosity properties set in the *system/fvOptions* file.

In Listing 3.5, we can see the *porosityProperties* file for OpenFOAM 2.3.1 and is taken from the *angledDuctExplicit* tutorial case. This exact case can also be used for versions 2.4.0, and with a slight modification (one needs to simply comment lines 14 to 17, and 21 in Listing 3.5) to this *porosityProperties* file, the exact same case will run in version 2.2.2.

Here we set the D and F coefficients calculated as per Sub-Section 2.3 and Equations 3.4 and 3.5 set in a porosity zone called "porosity1", but which can be refer to any cell zone define in the *constant/polyMesh/blockMeshDict* file.

Listing 3.4: *pEqn.H* file structure with explicit porosity treatment relaxation factors.

```
volVectorField HbyA("HbyA", U);
if (pressureImplicitPorosity)
{
    HbyA = trTU()&UEqn().H();
}
else
{
    HbyA = trAU()*UEqn().H();
}

UEqn.clear();
surfaceScalarField phiHbyA("phiHbyA", fvc::interpolate(HbyA) & mesh.Sf());

mrfZones.relativeFlux(phiHbyA);
adjustPhi(phiHbyA, U, p);

while (simple.correctNonOrthogonal())
{
    tmp<fvScalarMatrix> tpEqn;

    if (pressureImplicitPorosity)
    {
        tpEqn = (fvm::laplacian(trTU(), p) == fvc::div(phiHbyA));
    }
    else
    {
        tpEqn = (fvm::laplacian(trAU(), p) == fvc::div(phiHbyA));
    }

    tpEqn().setReference(pRefCell, pRefValue);

    tpEqn().solve();

    if (simple.finalNonOrthogonalIter())
    {
        phi = phiHbyA - tpEqn().flux();
    }
}

#include "continuityErrs.H"

// Explicitly relax pressure for momentum corrector
p.relax();

if (pressureImplicitPorosity)
{
    U = HbyA - (trTU()&fvc::grad(p));
}
else
{
    U = HbyA - (trAU()*fvc::grad(p));
}

U.correctBoundaryConditions();
fvOptions.correct(U);
```

Listing 3.5: Porosity properties for *porosity1* zone in *angledDuctExplicit* tutorial case mesh

```
porosity1
{
    type            DarcyForchheimer;
    active          yes;
    cellZone        porosity;

    DarcyForchheimerCoeffs
    {
        d   d [0 -2 0 0 0 0 0] (5e7 -1000 -1000);
        f   f [0 -1 0 0 0 0 0] (0 0 0);

        coordinateSystem
        {
            type    cartesian;
            origin  (0 0 0);
            coordinateRotation
            {
                type    axesRotation;
                e1      (0.70710678 0.70710678 0);
                e2      (0 0 1);
            }
        }
    }
}
```

"Inside the cell zone a local coordinate system can be defined. The global coordinate system of the geometry is set by default. The coordinate system is defined with the `coordinateSystem` class. Which has several constructors . The vector e_1 is created as a linear combination of the global x- and y-axis so it is aligned with the angled duct and the vector e_2 is set orthogonal to e_1. The vector e_3 is then created in a right handed order by the `coordinateSystem` class orthogonally to both e_1 and e_2. More examples of how to create a local coordinate system can be found in the description at the header of *coordinateSystem.H*, located in *$FOAM_SRC/meshTools/coordinateSystems*".

In `DarcyForchheimerCoeffs` the viscous and inertial resistance are defined, *i.e.*, the source term from Equation 3.2. "The two dimensioned vectors, `d` and `f` are added to the diagonal of the tensors D_{ij} and F_{ij} respectively. The coordinates of these vectors correspond to the local coordinate system. Default values of `d` and `f` is zero. At least one component of the vectors need to be greater than zero. The code will automatically multiply negative values with the largest component of the vector and switch the sign to a positive value. This is done with the method `adjustNegativeResistance` which is implemented in" `DarcyForchheimer.C` (Hafsteinsson, 2009).

3.5 Implementation of new models in OpenFOAM

In this work several RAS turbulence models were used in order to validate the **porousSimpleFOAM**, however, many of the models used successfully by Filonovich (2015) and

Brito et al. (2016) are not included in the standard distributions of OpenFOAM. Although it was beyond the scope of this thesis to program and implement new turbulence models, such as Brito et al. (2016) use of the EARSM turbulence model to properly model secondary flows and their influence on stream-wise velocity distribution. However, we were able to make use of a BSL-EARSM model, implemented for OpenFOAM-1.7.x by Jeyapaul (2015) and subsequently adapted for versions 2.3.1 (also compatible with 2.2.2 and 2.4.0) and 4.1 by Yogesh (2017).

Likewise, new porosity models can be implemented and customised as exemplified in Gooya (2014) and Hafsteinsson (2009). A number of these models are described in Section A.2 of Appendix A.

Chapter 4

Case Studies

In this chapter an outline of the cases used for validation of the **porousSimpleFOAM** solver will be presented, with and without submerged vegetation, alongside each case's respective results and analysis. These are previously published works which encompass both experimental and numerical studies using both drag coefficient and porous media models to account for the effect of the submerged vegetation (when present).

Cases without submerged vegetation are run with D and F values (Equations 3.4 and 3.4, respectively) set to null. These are the experimental and numerical studies presented in research papers II and III in Filonovich (2015), published elsewhere as Filonovich et al. (2010) and Filonovich et al. (2014), respectively. The purpose of performing these studies with **porousSimpleFOAM** is in testing the implementation of the SIMPLE algorithm and the selected turbulence models ($k-\epsilon$, NonlinearKEShih and BSL-EARSM) so as to compare them with previously validated studies.

Analysis and comparison of select rectangular flume studies by Lopez and Garcia (1997) and Nezu and Sanjou (2008) were performed to test the porous media model in a simple channel geometry. Brito et al. (2016) is then used to test porous media and turbulence models on a symmetric compound open-channel.

All simulations were based on the *angledDuctExplicit* tutorial case with modified *transportProperties* for water flow ($\nu = 1 \times 10^{-6}$ $m^2 \cdot s^{-1}$), specific case mesh, turbulence model and porosity settings. Typically, unless specified, values in other files were left as is from the tutorial case.

Cases were run for 5000 steps with a unitary Δt. Results were considered if convergence for measured quantities stabilised below 10^{-4} within that number of steps, as per indication of LEAP CFD Team (2012).

In OpenFOAM, any kind of SIMPLE based solver doesn't have time derivation which is normally a natural limiter for the solution. This means, that for a special time interval

Δt, the solution will never go beyond this specified time step. Based on the fact that we do not have the time derivation within that algorithm, we are only interested in the steady-state behaviour. By simply setting the time step Δt to 1, the total simulation "time" is essentially the number of iterations performed within the SIMPLE loop. Changing the time step to other values **will not influence the solution**. At best, it will only allow us to reach a pre-set *pseudo end time* faster or not, as we are effectively setting a limit on the number of iterations to be performed by the algorithm (Holzmann, 2016).

Given that **simpleFOAM** (and by extension **porousSimpleFOAM** as well) is a single-phase solver, all numerical simulations made use of the same assumption as Filonovich et al. (2014), in that instead of a free surface the interface is treated as a flat plate with a slip condition instead. This has been proven a valid approach, also considering that current algebraic models fail to account for the formation of secondary currents due to the air-water interaction (Filonovich, 2015).

The turbulence models considered for most simulations were the classic $k-\epsilon$ turbulence model with open channel flow coefficients as per Table 2.3 (for direct comparison with cases where previous numerical studies had used this turbulence model), the NonlinearKEShih based on Shih et al. (1994) and implemented natively in OpenFOAM, and the BSL-EARSM by Menter et al. (2012), programmed for OpenFOAM 1.7.x by Jeyapaul (2015) and adapted to later versions by Yogesh (2017), and the SST for one particular case. Other turbulence models were tested (LRR, LienCubicKE) but with no valid results, which doesn't necessarily invalidate those models. Boundary conditions, initial conditions and mesh element distribution have to be taken into account for each turbulence model, and further considerations may have to be taken in order for these models to work properly with these case studies.

Typically values for ω based turbulent models were set at set $\omega = 2222.2\ s^{-1}$ (unless otherwise stated) which had been determined with the use of CFD-Online (2016) using the default k and ϵ values in the *angledDuctExplicit* tutorial case, assuming the relationship in Equation 2.77.

Given that not all simulations converged into stable residuals, only those which presented significant numerical results will be subject to analysis and further discussed.

All of the figures generated for this work's numerical studies were done so as to be as visually identical as possible to the analysis presented on the experimental and numerical works on which they are based. The added figures which illustrate secondary flow were generated using the post-processing tool Tecplot 360, which calculates the cross flow velocity (v_{cf}) for stream velocity purely in the x direction (Tecplot, Inc., 2014):

$$v_{cf} = \sqrt{v^2 + w^2} \qquad [m \cdot s^{-1}] \tag{4.1}$$

This cross flow is mentioned in this work as secondary flow.

Conclusions from these studies are then presented in the next chapter.

4.1 Non-vegetated channels

In this section the experimental and numerical parameters from the studies on non-vegetated channels are presented.

The purpose of the use for these numerical studies was to determine the validity of the **porousSimpleFoam** solver and the considered turbulence models in open channel flow before applying the porous-media condition.

4.1.1 Asymmetric rectangular compound channel

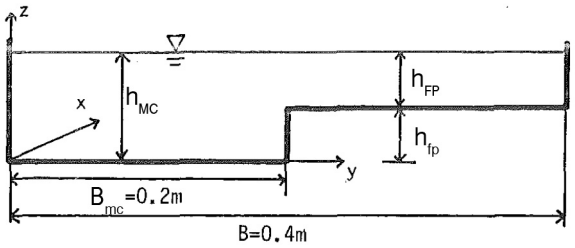

Figure 4.1: Adapted schematic description of floodplain open-channel flow from Tominaga and Nezu (1991).

The work presented in Filonovich et al. (2014) is based on the experimental study by Tominaga and Nezu (1991) of an asymmetrical rectangular compound channel (Figure 4.1), in particular experiment **S-2**. "The experiments were conducted in a tilting flume with 12.5 m length and 0.4×0.4 m cross-section. The bed wall was composed of a painted iron plate and the sidewalls were composed of glass. A fully developed and uniform flow was established at the test section 7.5 m downstream from the entrance of the channel" (Tominaga and Nezu, 1991). Here, h_{MC} e the depth of the MC, h_{FP} and h_{fp} the depth and height of the FP.

In their numerical study Filonovich et al. (2014) assumed that the flow is statistically homogenous in the stream-wise direction and driven by a constant pressure gradient Δp, thus made use of periodic boundary conditions for the inlet and outlet patches. The length of the domain in the stream-wise direction is $12h_{MC}$ and is discretised with uniformly spaced mesh in the stream-wise direction. In span-wise and in the vertical directions the mesh is refined close to the walls, free surface and transition zone between the MC and the FP. The grid considered for the BSL-EARSM simulation is of $200 \times 200 \times 80$ (40) hexahedral elements in the x, y and z directions, respectively, with the number in parenthesis indicating the number of elements in the FP in the z direction.

In this work, the computational domain was set up as that of Filonovich et al. (2014) (see Figure) but with a constant inlet flow of mean bulk flow velocity $U_A = 0.349$ $[m \cdot s^{-1}]$ as per Table 1 in Tominaga and Nezu (1991), and `inletoutlet` type patch for the outlet patch.

The simulations were run with the BSL-EARSM turbulence model so as to directly compare the implementation of Menter et al. (2012) by Jeyapaul (2015) with the validated implementation of that turbulence model in CFX. The SST was also used for direct comparison with results in the target study. The NonlinearKEShih model was used to test its ability to accurately predict the intricacies of compound open channel flow in comparison with other validated models.

Experimental results for Tominaga and Nezu (1991) case **S-2**, are comprehensive in the original paper. Figures 4.2 and 4.3 show the original experimental measurements for stream-wise velocity distribution and and secondary current vectors, respectively.

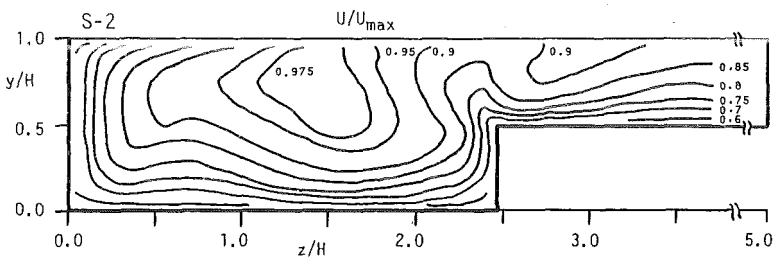

Figure 4.2: Isovels of primary mean stream-wise velocity U for experimental case **S-2**. Adapted from Tominaga and Nezu (1991).

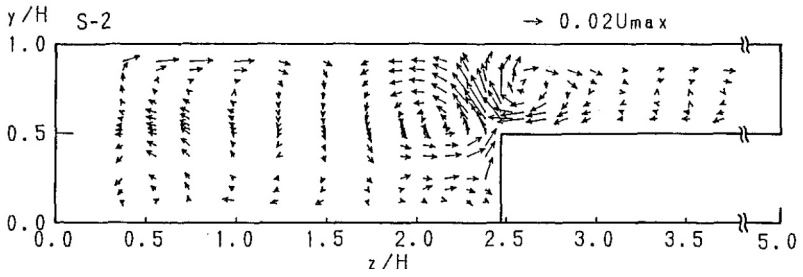

Figure 4.3: Secondary current vectors for experimental case **S-2**. Adapted from Tominaga and Nezu (1991).

Conclusions in Filonovich et al. (2014) point out that all used turbulence models in that work (BSL-EARSM, BSL-RSM and SSG-RSM) are able to reproduce the complex flow pattern of primary velocity field, secondary currents, Reynolds stresses, anisotropy of turbulence and production term of secondary currents, obtaining overall a good agreement between numerical results and the experimental data of Tominaga and Nezu (1991). Figure 4.4 illustrates the results from that work in regards to stream-wise velocity distribution and secondary current vectors (for further analysis please consult the source).

"For the particular flow studied (high flow depth) the flow is clearly dominated by wall turbulence and the anisotropy generated at the boundary corners. This helps to explain better performance of BSL's models against SSG-RSM. Although the latter constitutes a more realistic conceptual model, since it resolves the exact Reynolds transport equations

using a quadratic pressure strain term, the simpler BSL's models give better results due to a better wall treatment.

It was also concluded that the simpler model (BSL-EARSM) gave better results than the most complex ones (BSL-RSM and SSG-RSM), indicating that neglecting advection and diffusion terms in the exact transport equation for the Reynolds stress anisotropy promotes the generation of stronger secondary flow cells.

In this particular case (wall dominated anisotropic turbulence) it seems clear that a use of a simpler model can reproduce accurate results, as long as a proper wall treatment is used" (Filonovich et al., 2014).

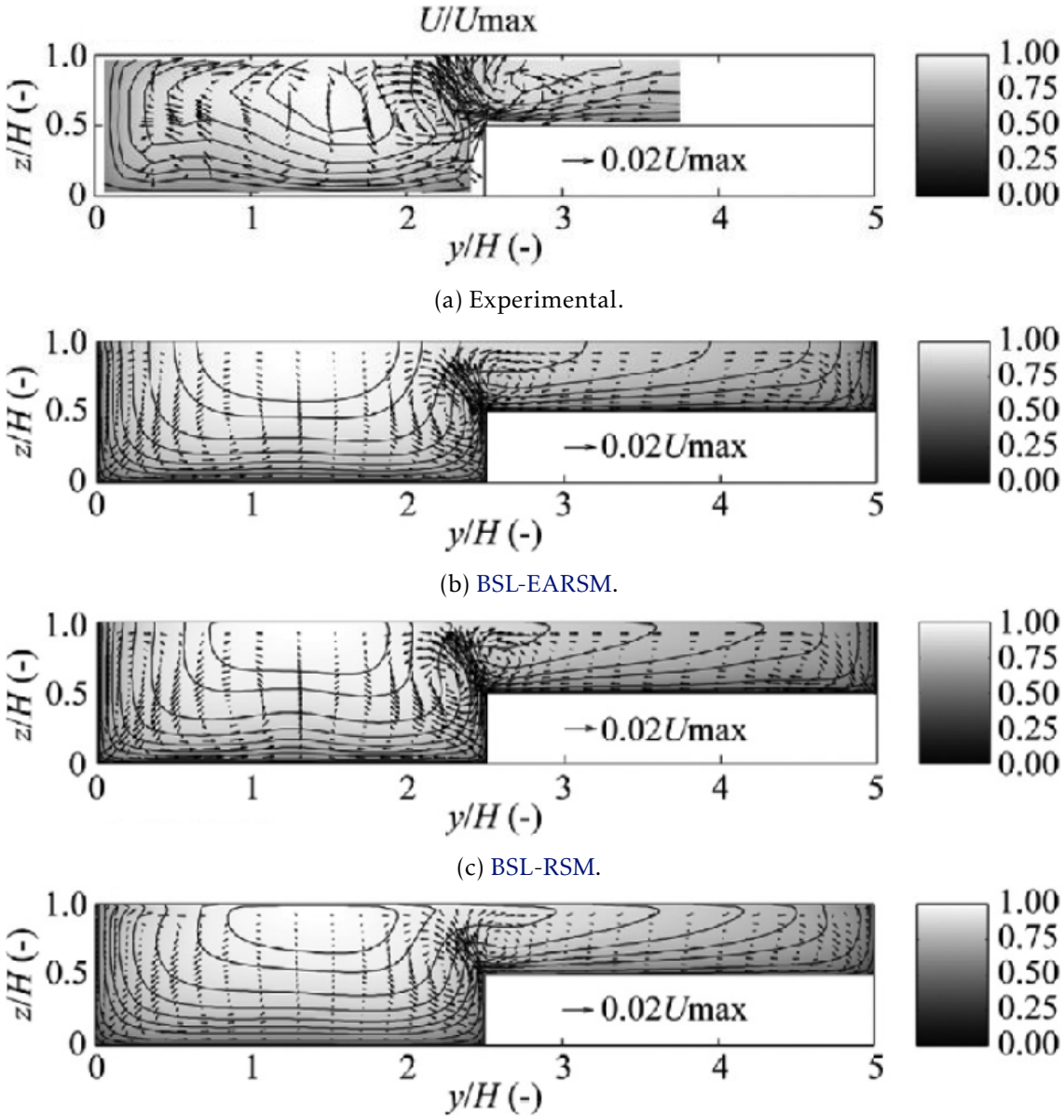

(a) Experimental.

(b) BSL-EARSM.

(c) BSL-RSM.

(d) SSG RSM.

Figure 4.4: Isovels of mean streamwise velocity U normalized by U_{max}. Adapted from Filonovich et al. (2014).

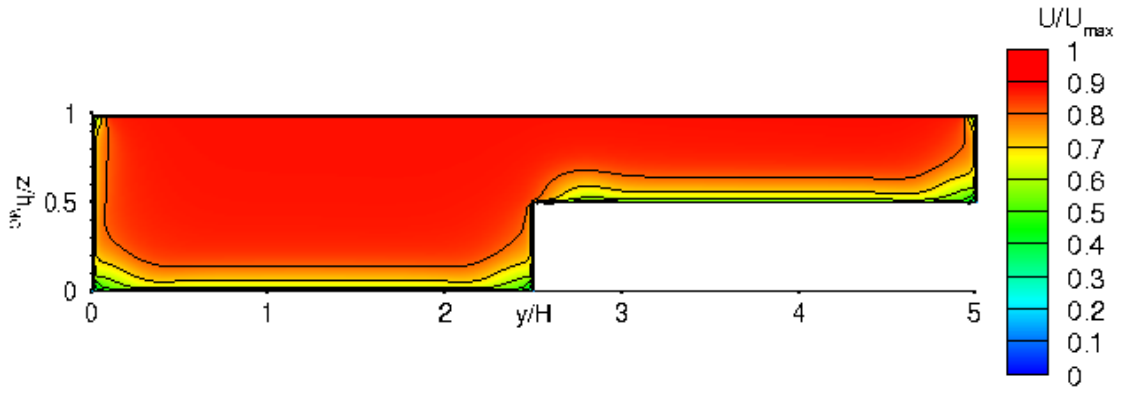

(a) **NonlinearKEShih**.

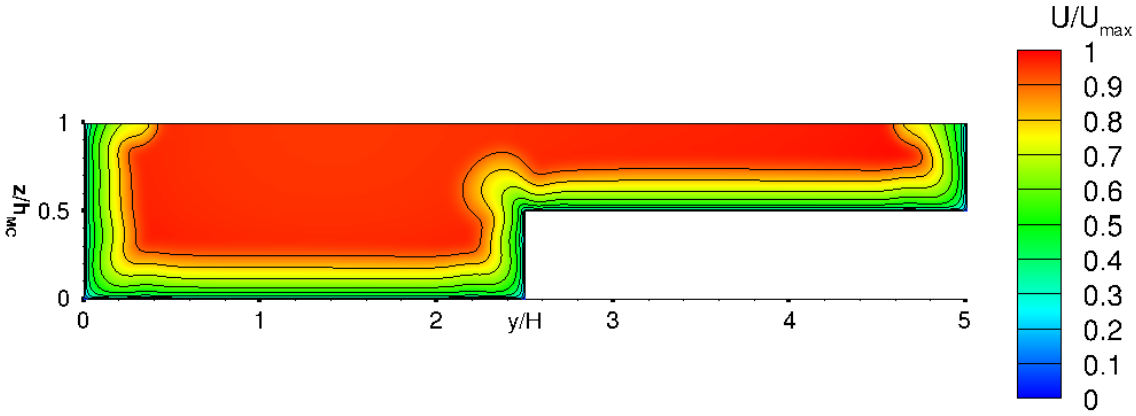

(b) BSL-EARSM.

Figure 4.5: Isovels of primary mean stream-wise velocity U normalized by U_{max} for numerical study of Tominaga and Nezu (1991) in OpenFOAM.

In this work, the use of the **NonlinearKEShih** and BSL-EARSM turbulence models was able to partly replicate the results of Filonovich et al. (2014) as seen in Figures 4.5, 4.6, 4.7 and 4.8. As can be seen in those Figures, the **NonlinearKEShih**, although able to account for secondary flow currents it is wildly inaccurate in their shape and placement, thus influencing the stream-wise velocity profiles along the channel cross section.

One particular feature of the stream-wise velocity profile captured by the BSL-EARSM model in this work is the "significant bulging upwards of the isovels at the interface due to the secondary currents generated by turbulence anisotropy" (Filonovich et al., 2014) as can be seen in Figure 4.5b, which is absent in the **NonlinearKEShih** model (Figure 4.5a).

The presence of secondary flow cells and their illustration in Figures 4.6 and 4.7 (the latter perhaps illustrating a clearer picture of their placement and magnitude) also demonstrates how the BSL-EARSM model used is in closer agreement with the experimental results of Tominaga and Nezu, 1991 and the numerical results of Filonovich et al. (2014).

Although the application of the BSL-EARSM model by Jeyapaul (2015) and Yogesh (2017) is also based on the work of Menter et al. (2012) as the one used by Filonovich et al. (2014), as mentioned previously (Chapter 2, Sub-section 2.4.3.2) the application

differs minutely (slightly different coefficients and wall treatment), and hasn't yet been extensively validated for compound open-channel flow.

Also, as mentioned in the previous section, the numerical study conditions vary slightly, as this work didn't make use of a periodic condition for the inlet and outlet patches, instead imposing a constant flow rate based on the mean bulk velocity provided in the original experimental data in Tominaga and Nezu (1991), which only provides a mean bulk velocity for the entire cross-section instead of U_{MC} and U_{FP} as in Brito et al. (2016) which would have presented a more realistic cross section stream-wise velocity profile at the inlet.

These small, albeit significant differences, are likely explanations for the discrepancies shown between both the numerical studies of Filonovich et al. (2014) and those of this work. However, they are sufficiently close to illustrate the present model's application is sufficiently able to numerically replicate the intended flow properties.

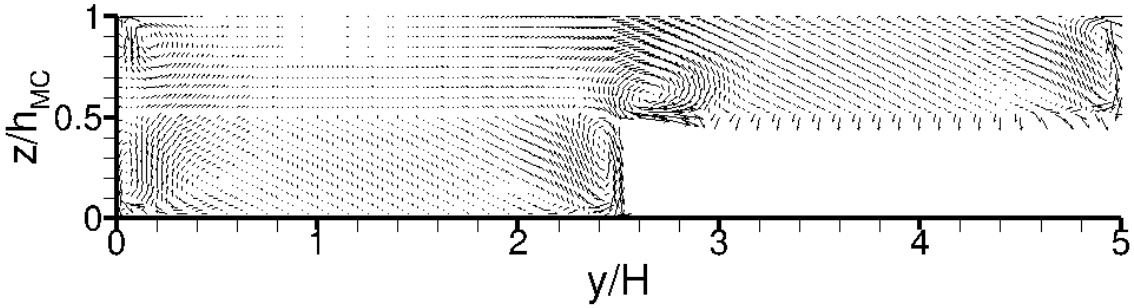

(a) **NonlinearKEShih**.

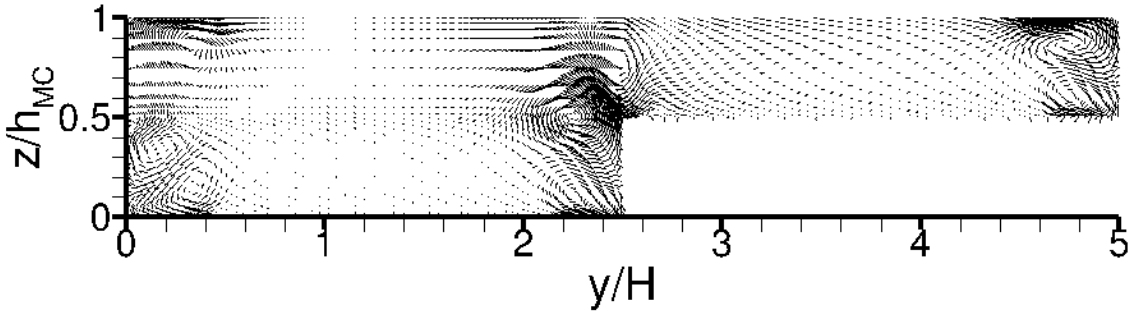

(b) BSL-EARSM.

Figure 4.6: Vector plot for numerical study of Tominaga and Nezu (1991) in OpenFOAM.

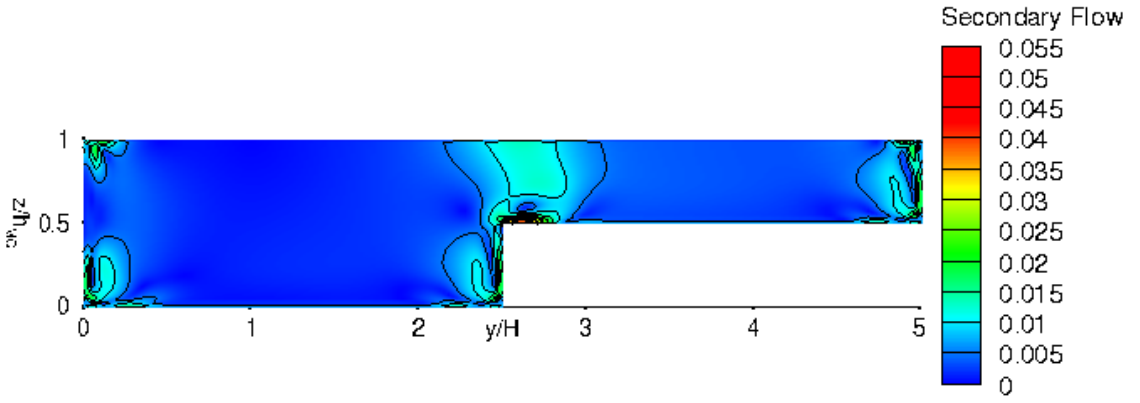

(a) **NonlinearKEShih**.

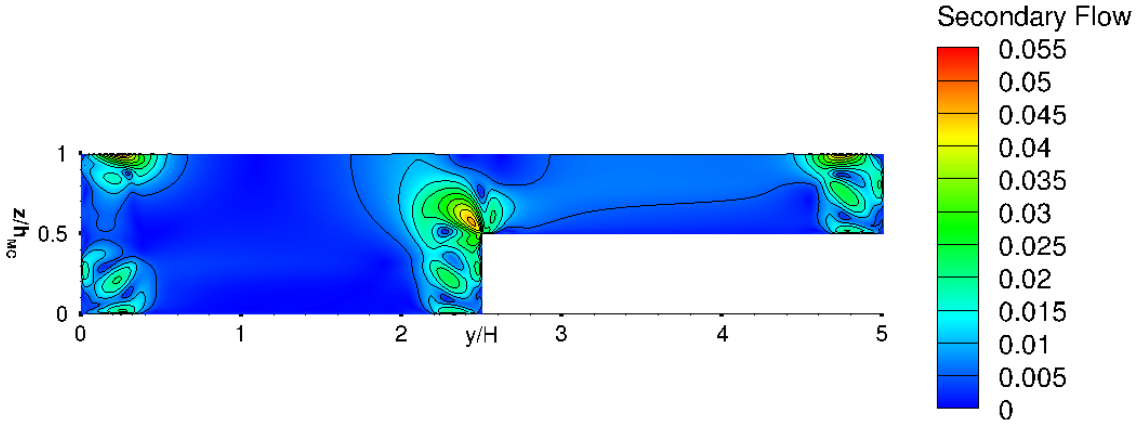

(b) BSL-EARSM.

Figure 4.7: Secondary flow velocity plot (normalized for maximum stream-wise velocity U_{max}) for numerical study of Tominaga and Nezu (1991) in OpenFOAM.

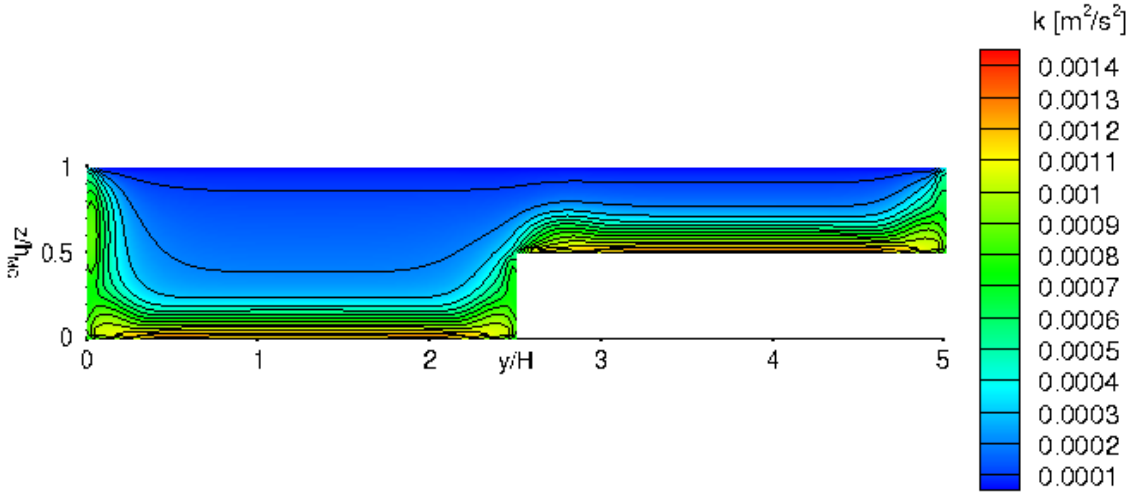

(a) **NonlinearKEShih**

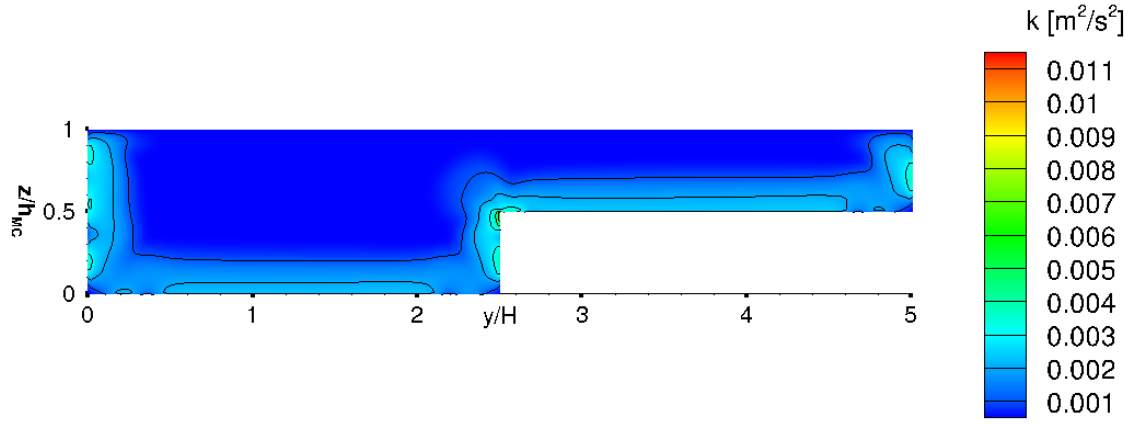

(b) BSL-EARSM

Figure 4.8: TKE (k) plot for numerical study of Tominaga and Nezu (1991) in OpenFOAM.

4.1.2 Asymmetric trapezoidal compound channel

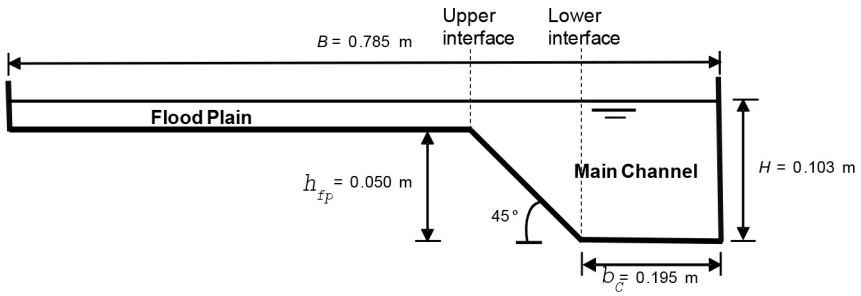

Figure 4.9: Cross-section from the asymmetric trapezoidal compound channel. Adapted from Filonovich et al. (2010).

The non-vegetated trapezoidal compound channel flow study is the one in Filonovich et al. (2010), where experimental studies were carried out in the Hydraulics Laboratory of the University of Beira Interior a in prismatic channel with a bed slope of $\theta = 0.001$, 10 $[m]$

length and with asymmetric trapezoidal compound section with dimension as per Figure 4.9. The uniform regime was established with a discharge of 24.7 $[l \cdot s^{-1}]$, which was input as a constant volumetric flow rate of 0.0274 $[m^3 \cdot s^{-1}]$ in the **porousSimpleFOAM** *U* file, inlet patch.

The original numerical study also made use of a free surface air-water interface, which was not possible in this study and thus simplified with a wall with slip condition in place of the free surface for reasons mentioned above.

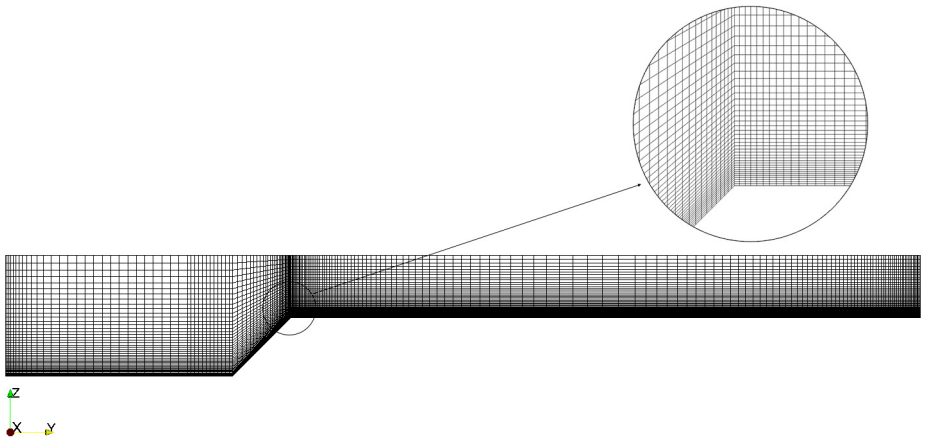

Figure 4.10: Mesh elements cross section distribution for **porousSimpleFOAM** for experimental study by Filonovich et al. (2010).

The original numerical study had a domain exactly coincident with the experimental flume, discretised using approximately 1,200,000 regular hexahedral elements aligned with the main directions. For turbulence modelling purposes, the z^+ of the element closest to the bottom walls were kept around 20 for the floodplain and 50 for the main channel, using therefore, wall functions for all the turbulent models" tested (Filonovich et al., 2010). In this study a distribution of hexahedral elements was similar to that in the study for Brito et al. (2016) (Figures 4.10 and 4.27 for this work and Brito et al. (2016), respectively), with 10,000,000 elements.

Filonovich et al. (2010) made use three different turbulent models, all based on the basic RANS equations:

- $k-\epsilon$
- SST
- EARSM

In this work direct comparisons were made with the first two models but instead of the third the NonlinearKEShih and BSL-EARSM models were used. For the former, two studies were conducted with and without law of the wall applied to the *epsilon* file

wall patches (from OpenFOAM version 2.4.0 this turbulence model will only accept a `zeroGradient` type for wall patches), and for the latter model ωvalues had to be set an order of magnitude higher than the base value defined above.

The reason for these different parameter values for the BSL-EARSM turbulence model is due to the imbalance caused by the uniform flow discharge at the inlet. For e.g., in Brito et al. (2016), data is provided for for flow discharge for the MC and FP, which results in different inlet velocities for each. However, in Filonovich et al. (2010) only a bulk flow discharge Q is provided, thus imposing the same stream-wise inlet velocity U across the entire cross-section. Because in reality the MC would have a higher inlet velocity, and the FP a lower one, when using the BSL-EARSM turbulence model one has to compensate for this imbalance and the resulting turbulence by setting initial conditions by increasing the turbulent dissipation rate ω in order to take into account an even smaller turbulence length scale l.

Much like the results in the previous Sub-section the numerical studies from this work based on Filonovich et al. (2010) show once again that although it can predict secondary currents, the **NonlinearKEShih** model makes wildly inaccurate predictions as to their placement, magnitude and subsequent impact on stream-wise velocity currents even when compared to the linear SST model (Figure 4.14), with the BSL-EARSM demonstrating the results closest to the original study's experimental and numerical results (Figure 4.13. However, slight discrepancies persist between the Filonovich et al. (2010) numerical study and that of this work. Much like the numerical study conducted in the previous Sub-section for Filonovich et al. (2014), the inlet span-wise velocity profile is uniform due to there only being a bulk flow rate provided in the experimental description.

Also, this work makes use of the adapted BSL-EARSM model while the original numerical study made use of the EARSM model. Even so by comparing the secondary current vector plots of both works (Figures 4.15 and 4.16) and the secondary flow plot for this work (Figure 4.17) it shows sufficiently agreeable results in terms of secondary flow placement and topology, although it slightly overestimates its maximum velocity which also impacts the stream-wise flow velocity profiles as shown in Figures 4.11 and 4.12. This over-estimation might be due to the use of a wall patch with no-slip condition, as it can be seen from Figure 4.11 that the free-surface air-water interaction does provide drag and subsequently slows down the flow at the free-surface.

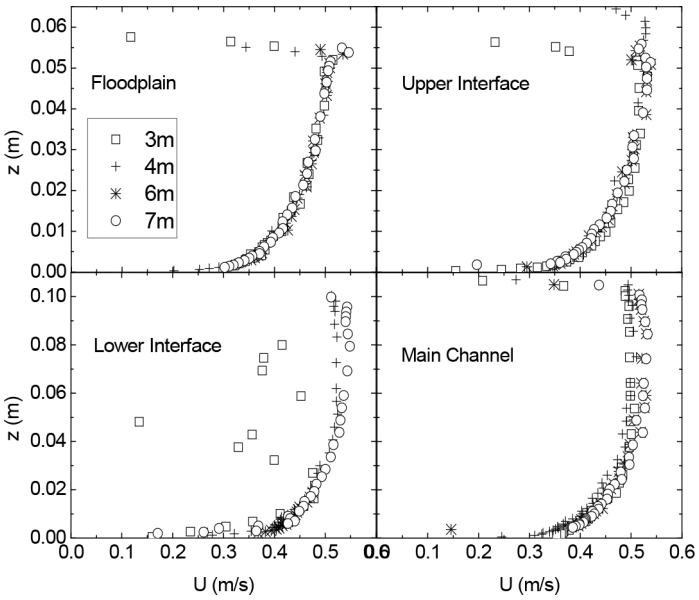

Figure 4.11: Measured vertical profiles of time-averaged velocity in the floodplain, in the upper and lower interfaces. Adapted from Filonovich et al. (2010).

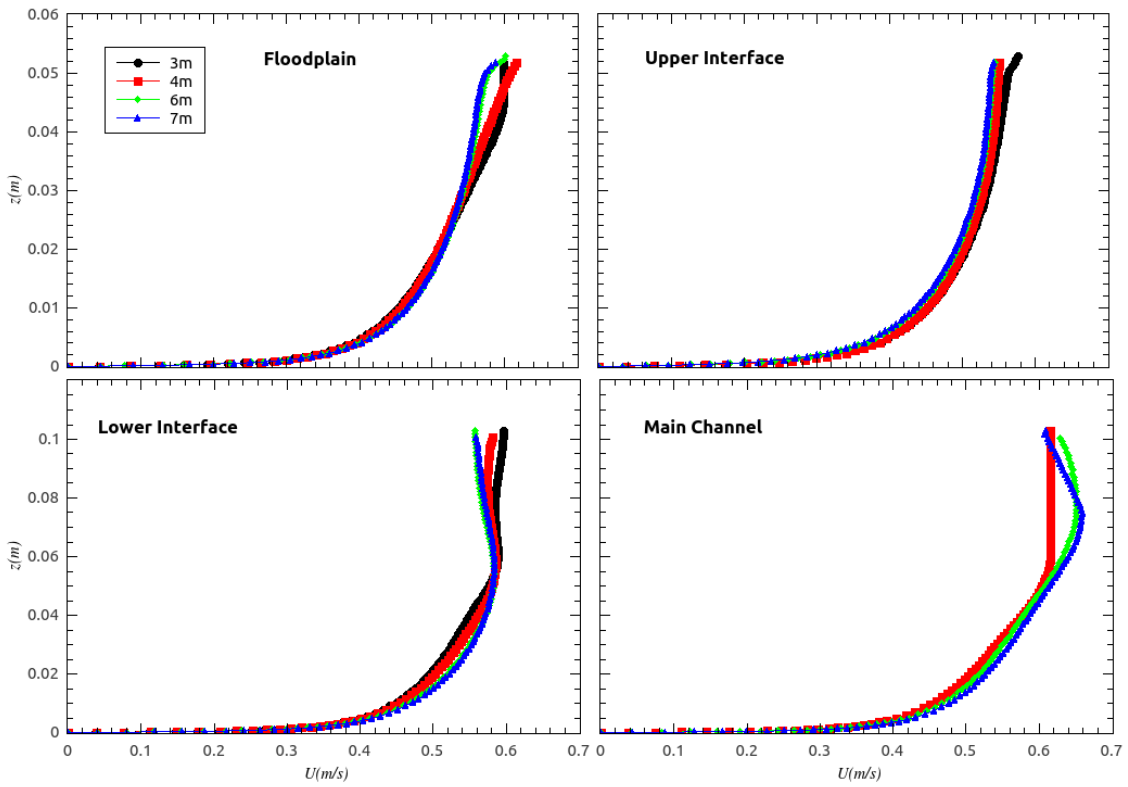

Figure 4.12: Measured vertical profiles of time-averaged as per Figure 4.11 for OpenFOAM numerical study with BSL-EARSM turbulence model.

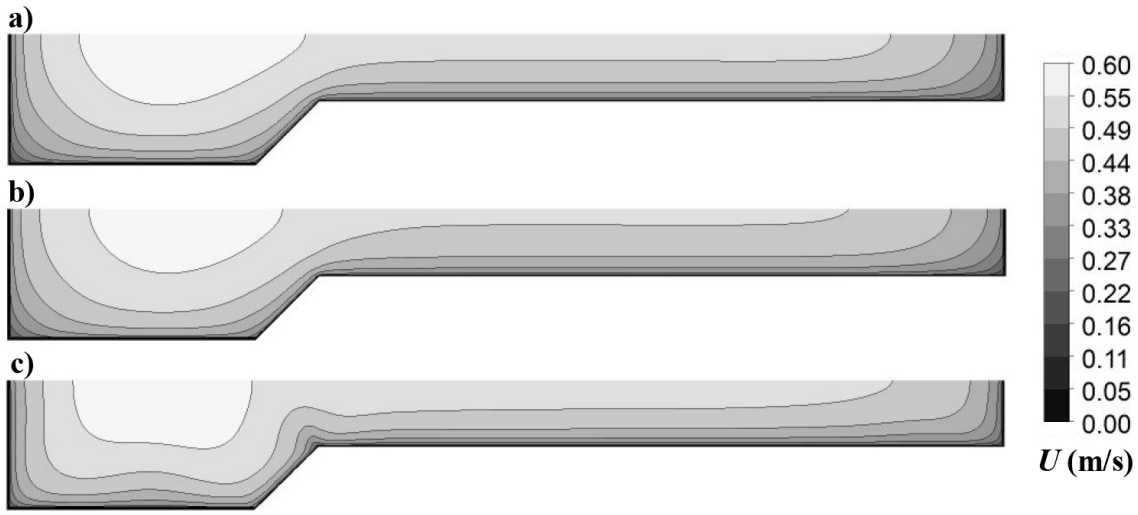

Figure 4.13: Isovel lines obtained numerically in cross-section $x = 7\ m$ with turbulence model: a) $k - \epsilon$; b) SST; and c) EARSM. Adapted from Filonovich et al. (2010).

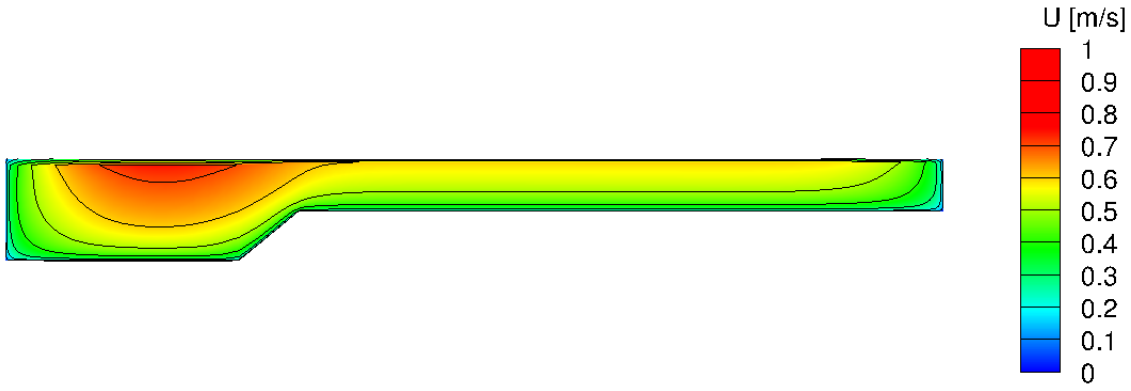

(a) SST.

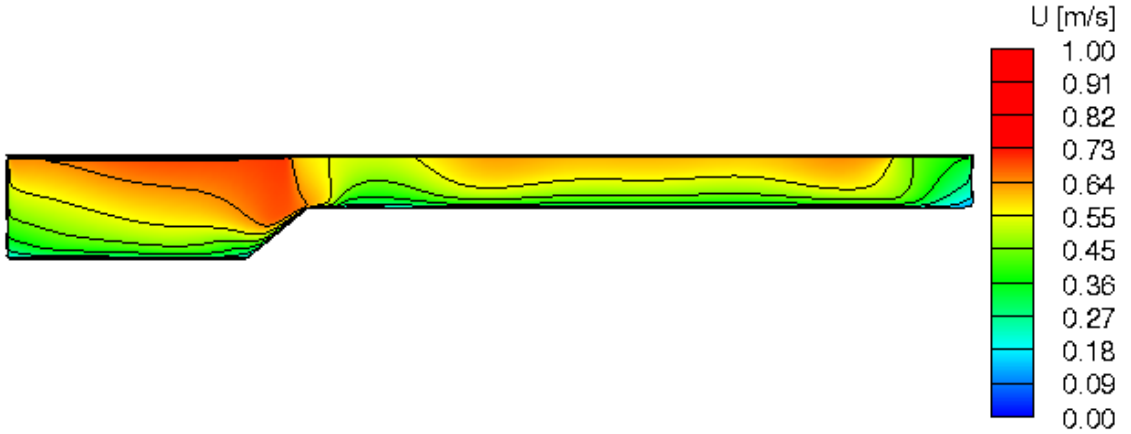

(b) **NonlinearKEShih**.

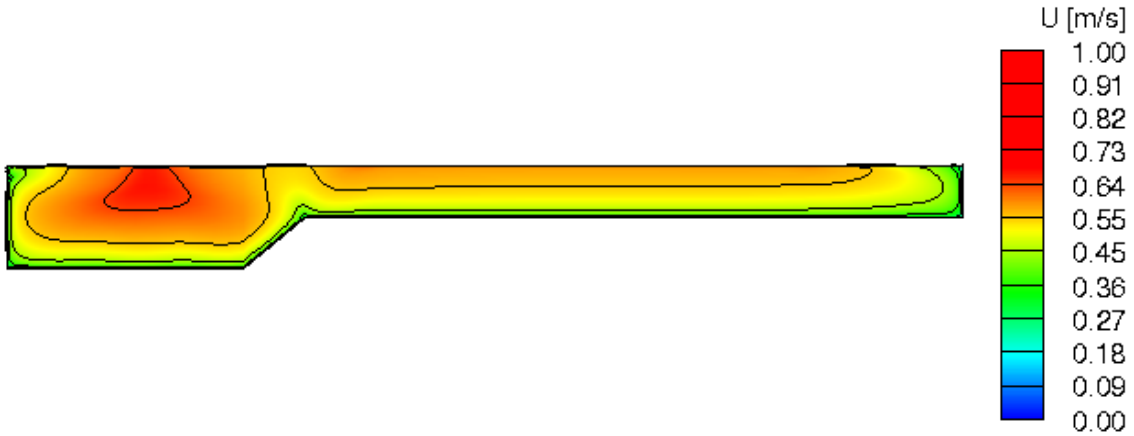

(c) BSL-EARSM.

Figure 4.14: Isovel lines obtained numerically in cross-section $x = 7\ m$ for numerical study of Filonovich et al. (2010) in OpenFOAM.

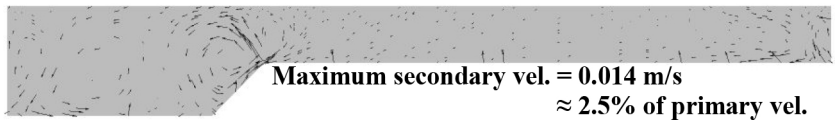

Figure 4.15: Secondary flow vectors obtained numerically in cross-section $x = 7\ m$ with EARSM turbulence model. Adapted from Filonovich et al. (2010).

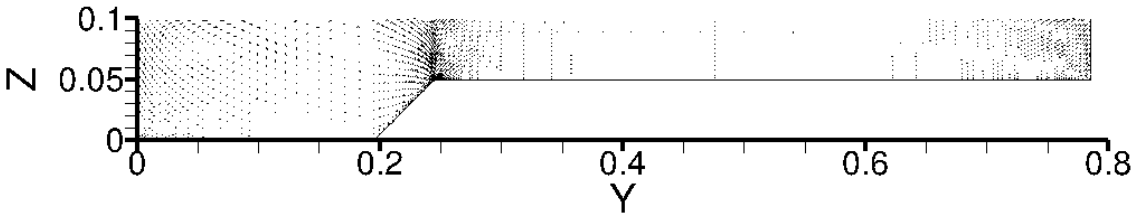

Figure 4.16: Secondary flow vectors obtained numerically for Filonovich et al. (2010) in cross-section $x = 7\ m$ with OpenFOAM and BSL-EARSM turbulence model.

Figure 4.17: Secondary flow obtained numerically for Filonovich et al. (2010) in cross-section $x = 7\ m$ with OpenFOAM and BSL-EARSM turbulence model.

The TKE plots of both numerical studies (Figures 4.18 and 4.19) reinforce the observations presented so far.

(a) $k - \epsilon$.

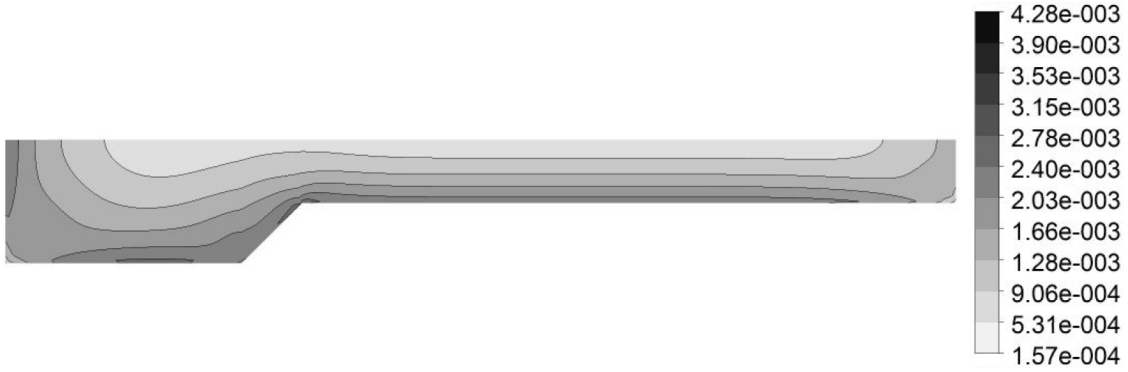

(b) SST.

(c) EARSM.

Figure 4.18: TKE results $[m^2/s^2]$, obtained numerically in cross-section $x = 7\ m$ with three different turbulence models. Adapted from Filonovich et al. (2010).

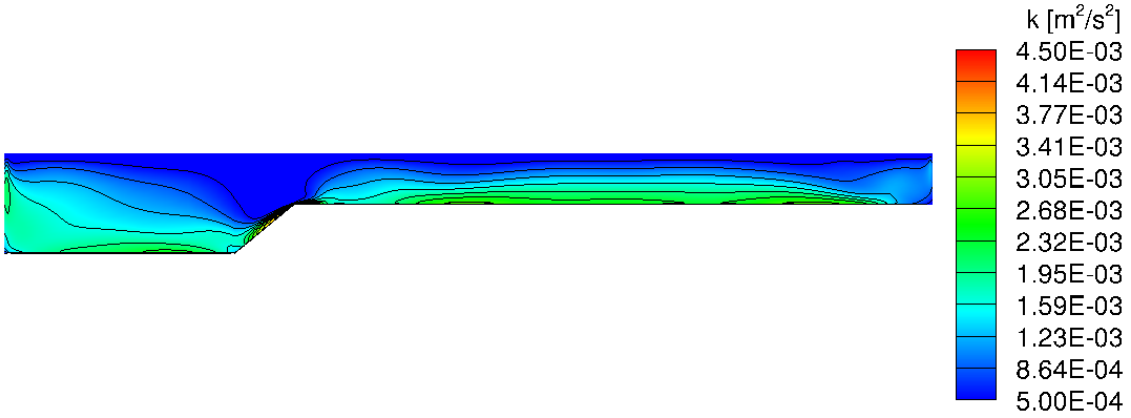

(a) **NonlinearKEShih**.

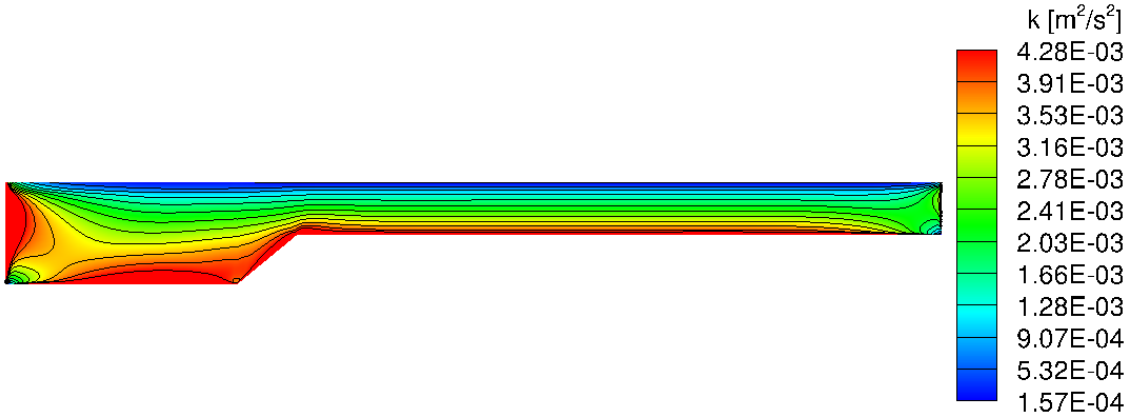

(b) SST.

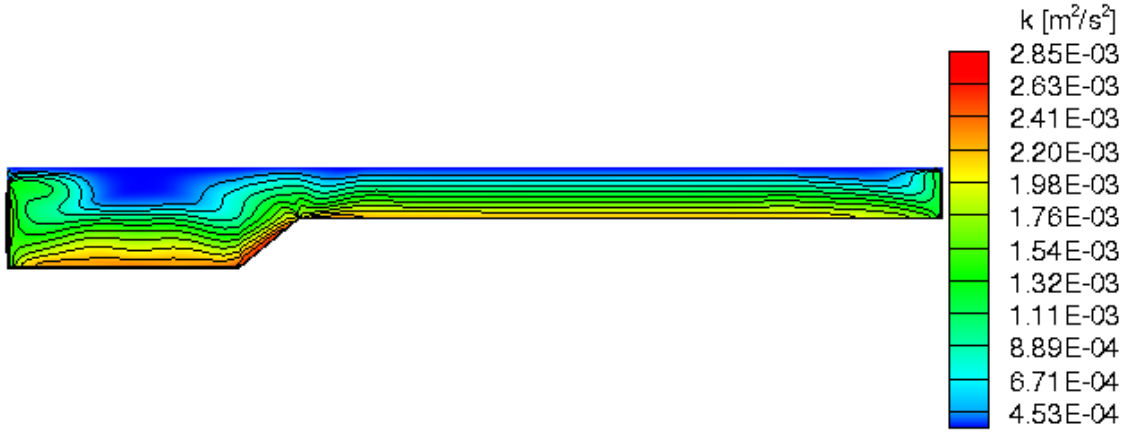

(c) BSL-EARSM.

Figure 4.19: TKE results $[m^2/s^2]$, obtained numerically for Filonovich et al. (2010) in cross-section $x = 7\ m$ with three different turbulence models in OpenFOAM.

4.2 Vegetated channels

In this section the porous media condition is applied in the numerical study of channels with submerged vegetation.

All numerical studies for vegetated cases were of symmetric channels and as such their

corresponding 3D computational domain was defined from the longitudinal symmetry plain of the channel, allowing the use of symmetry boundary condition in the middle of the MC. This was done so as to reduce the computational domain to half channel width and, consequently, reduce the computational time and computational resources required. As per Brito et al. (2016), this boundary condition ensures that the fluxes through the symmetry plain are zero, i.e., the velocity in the normal direction to that plain is zero and the gradients in that direction are negligible.

4.2.1 Symmetric rectangular simple channel

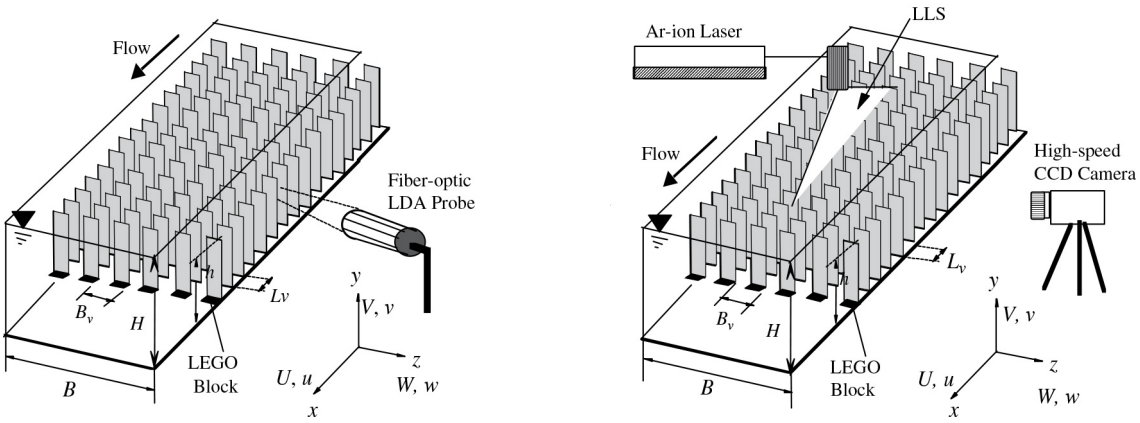

(a) LDA measurements (b) PIV measurements

Figure 4.20: Experimental setup. Adapted from Nezu and Sanjou (2008).

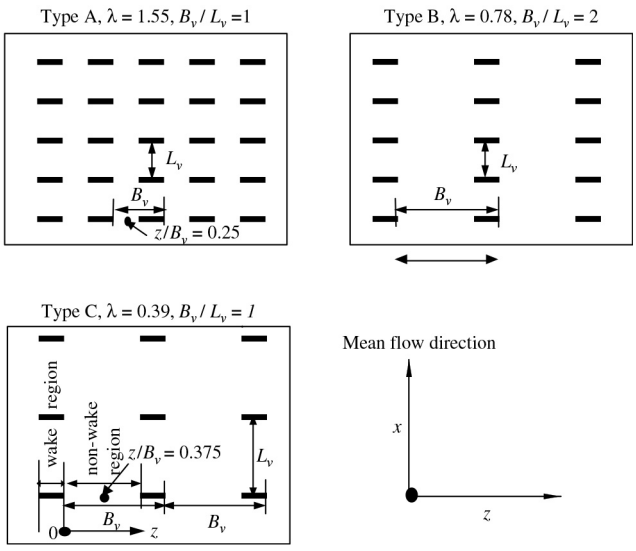

Figure 4.21: Allocation patterns of vegetation elements. Adapted from Nezu and Sanjou (2008).

Numerical studies were based on Exp. 1 and 9 from Lopez and Garcia (1997) (see also Fischer-Antze et al. (2001)) and experiments A-10, B-10 and C-10 from Nezu and Sanjou (2008) (Figure 4.20). The computational meshes for both experimental flumes used in OpenFOAM (Figure 4.22) consisted of hexahedral elements.

The computational domains for Lopez and Garcia (1997) was originally set with a cross section distribution of 25 elements in the y direction, 60 for the z direction (with 20 elements for the porous zone and 40 for the free-flow) and 1950 uniform element distribution in the x direction.

For Nezu and Sanjou (2008) the domain had 50 elements for the y direction, 100 elements for the z directions (20 for porous zone, 80 for the free flow) and 1000 uniformly spaced elements in the stream-wise x direction.

For all experiments space-averaged data of velocity components and shear stresses were collected for comparison with the simulation results. The experiments correspond to rigid vegetation, shallow submerged ($1 < H/h_v < 5$) and the density varies between transitional ($0.1 < \lambda < 0.23$) and dense ($\lambda > 0.23$) (see Nepf (2012a) and Nepf (2012b) for a revision on the vegetation characteristics).

The estimation of the porous media parameters followed the procedure defined in Li and Ma (2011) and used by Brito et al. (2016). Tables 4.2 and 4.4 are built from a spreadsheet given in personal correspondence (Leal, 2015), with the computations of the parameters mentioned previously.

The experimental parameters for Lopez and Garcia (1997) and Nezu and Sanjou (2008) are indicated in Tables 4.1 and 4.3, respectively. Their respective numerical simulations were run with the standard $k-\epsilon$, the NonlinearShihKE BSL-EARSM turbulence models.

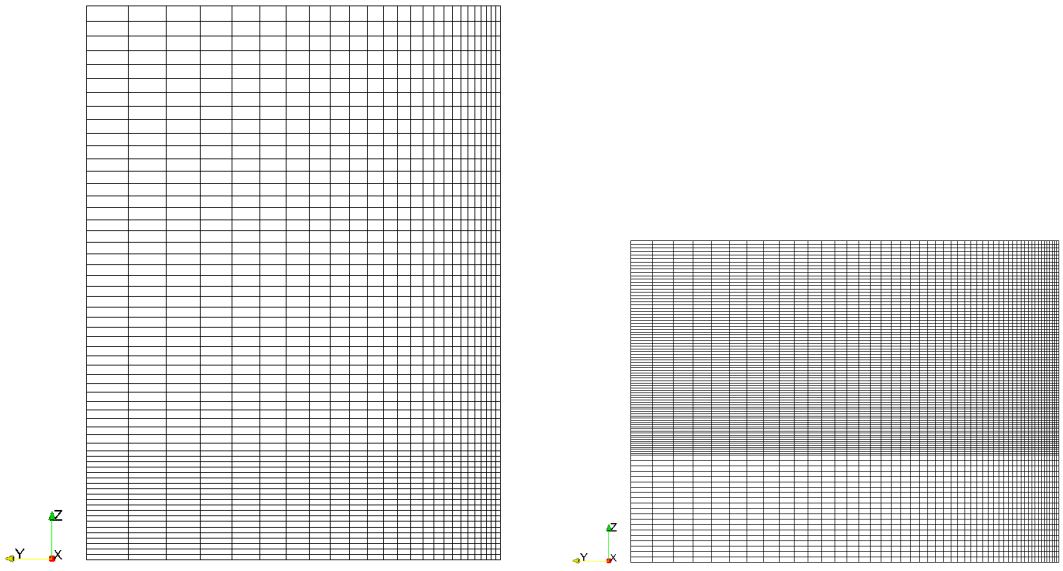

(a) Lopez and Garcia (1997). (b) Nezu and Sanjou (2008)

Figure 4.22: OpenFOAM mesh cross-section for **Nezu2008.**; Lopez and Garcia (1997)

Table 4.1: Lopez and Garcia (1997) experimental parameters

	L [m]	B [m]	H [m]	A [m^2]	U [$m \cdot s^{-1}$]	Q [$m^3 \cdot s^{-1}$]	$Q/2$ [$m^3 \cdot s^{-1}$]
Exp. 1	19.5	0.91	0.61	0.5551	0.322464421	0.179	0.0895
Exp. 9	19.5	0.91	0.61	0.5551	0.104485678	0.058	0.029

Table 4.2: Lopez and Garcia (1997) rectangular flume vegetation and porosity parameters

		Exp.1	**Exp.9**
d_v	[m]	0.0064	0.0064
h_v	[m]	0.12	0.12
ΔS	[m]	0.076626103	0.051006137
a	[m^{-1}]	1.09	2.46
φ	[-]	0.005478938	0.012365309
ϕ	[-]	0.994521062	0.987634691
λ	[-]	0.1308	0.2952
V_p	[m^3]	3.86039E-06	3.86039E-06
A_p	[m^2]	0.002412743	0.002412743
ψ	[-]	0.493242415	0.493242415
d_{vs}	[m]	0.004735127	0.004735127
K	[m^2]	4.898028263E-03	9.4178359688E-04
β	[m^{-1}]	2.058547051	4.74375612
D	[m^{-2}]	204.1637872	1061.815053
F	[m^{-1}]	2.058547051	4.74375612
H	[m]	0.335	0.214
H/h_v	[-]	2.79	1.78

Table 4.3: Nezu and Sanjou (2008) experimental parameters for A-10, B-10 and C-10 experiments

L [m]	B [m]	H [m]	A [m^2]	U [$m \cdot s^{-1}$]	Q [$m^3 \cdot s^{-1}$]	$Q/2$ [$m^3 \cdot s^{-1}$]
10	0.4	0.15	0.06	0.12	0.0072	0.0036

Table 4.4: Nezu and Sanjou (2008) rectangular flume vegetation and porosity parameters

		A-10	**B-10**	**C-10**
d_v (not cylinders)	[m]	0.008	0.008	0.008
h_v	[m]	0.05	0.05	0.05
ΔS	[m]	0.016095569	0.022689216	0.034401046
a	[m^{-1}]	30.88	15.54	6.76
φ	[-]	0.194024762	0.0976407	0.042474333
ϕ	[-]	0.805975238	0.9023593	0.957525667
λ	[-]	1.544	0.777	0.338
V_p	[m^3]	2.51327E-06	2.51327E-06	2.51327E-06
A_p	[m^2]	0.001256637	0.001256637	0.001256637
ψ	[-]	0.711378661	0.711378661	0.711378661
d_{vs}	[m]	0.008536544	0.008536544	0.008536544
K	[m^2]	6.7565295E-06	3.7441189E-05	2.3641283E-04
β	[m^{-1}]	75.97103306	27.24258756	9.918163425
D	[m^{-2}]	148004.978	26708.55357	4229.888846
F	[m^{-1}]	75.97103306	27.242587558	9.918163425
H	[m]	0.15	0.15	0.15
H/h_v	[-]	3.00	3.00	3.00

By starting with the simplest open-channel flow geometry it is intuitively expected that it would yield the stablest results due to the far less complex nature of the flow (as demonstrated in Chapter 2, Section 2.5). However, as we shall see from the results of numerical studies in OpenFOAM based on the work of Lopez and Garcia (1997) and Nezu and Sanjou (2008), this turned out not to be the case.

As can be seen for the case of **Exp. 1** by Lopez and Garcia (1997) and the case of **A-10** by Nezu and Sanjou (2008) (Figures 4.23 and 4.24, respectively), it is impossible to obtain any sort of residual stabilization under the given experimental conditions. All other cases yielded similar results which, for the sake of brevity, are not illustrated here.

Even with the use of the simplest linear turbulence model such as k-ϵ in both previously mentioned cases (Figures 4.23a and 4.24a, respectively), at best we can obtain residuals for values under 10^{-4}, but as we can see from Figure 4.24a these still won't stabilize to within a 4% margin within the given time-step limit.

Once secondary currents are taken into account with the use of both non-linear and algebraic turbulence models, results either oscillate wildly at high residual values in the case of the **NonlinearKEShih** turbulence model (Figures 4.23b and 4.24b), or in the case of the BSL-EARSM turbulence model either stabilizes at values greater than 10^{-4} with atypically high oscillations (Figure 4.24c) or simply "blew-up", i.e., gave a *floating point exception* (dividing by zero) (Holzmann, 2016).

Numerous other numerical trials of these cases with variations in mesh geometry and linear and non-linear Darcy-Forchheimer coefficient parameters (due to parameter input errors) yielded similar results.

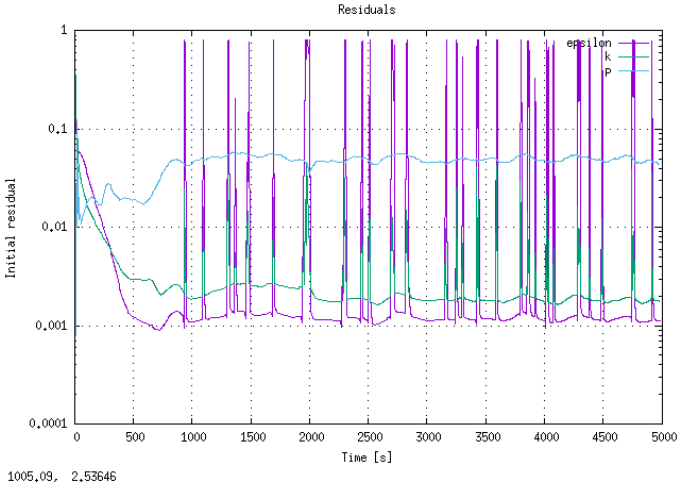

(a) $k-\epsilon$.

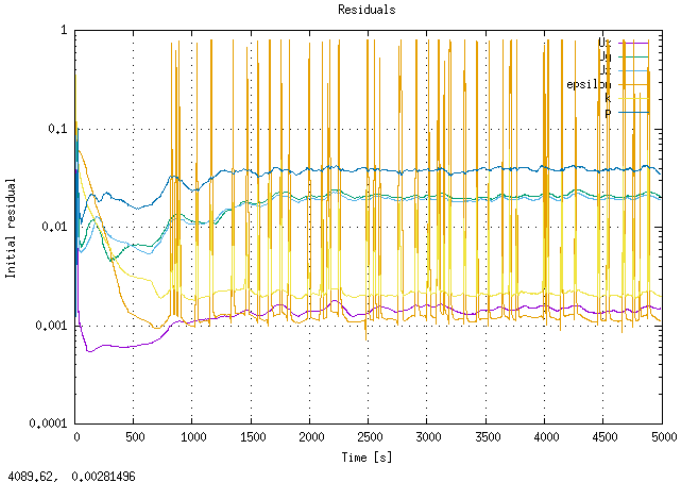

(b) **NonlinearKEShih**.

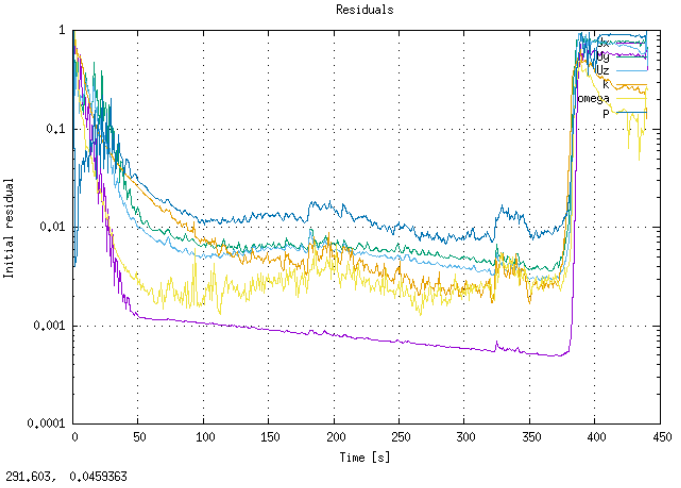

(c) BSL-EARSM.

Figure 4.23: Residuals of numerical study using three different turbulence models in OpenFOAM for case **Exp. 1** of Lopez and Garcia (1997).

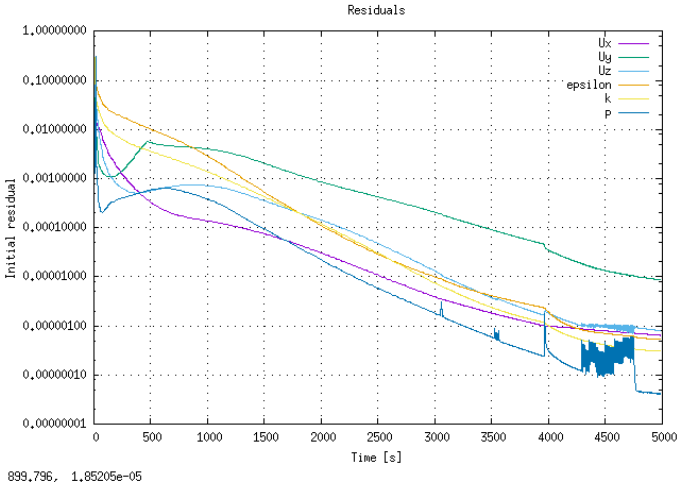

(a) $k-\epsilon$.

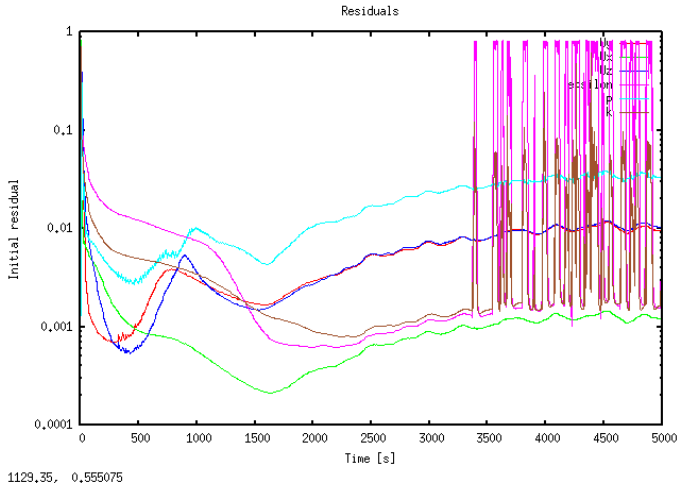

(b) **NonlinearKEShih**.

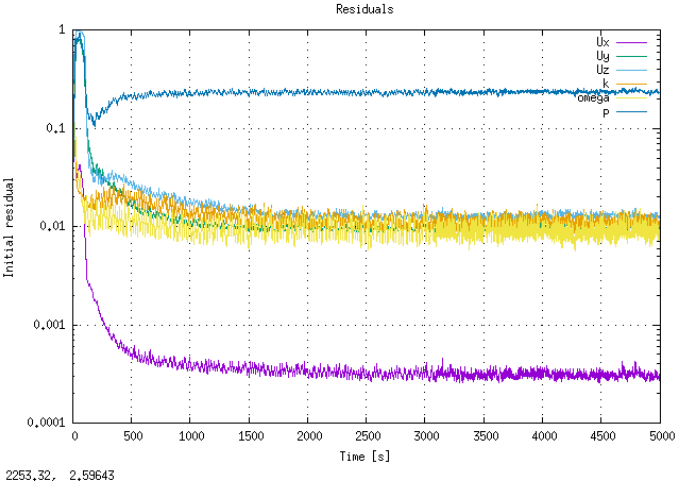

(c) BSL-EARSM.

Figure 4.24: Residuals of numerical study using three different turbulence models in OpenFOAM for case **A-10** of Nezu and Sanjou (2008).

4.2.2 Symmetric trapezoidal compound channel

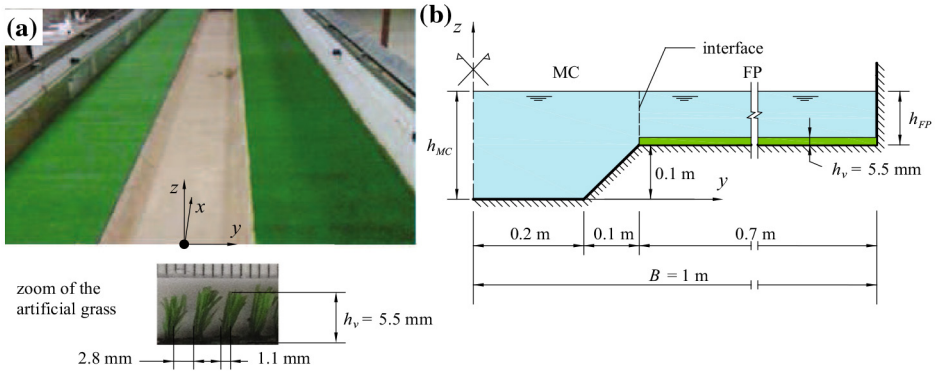

Figure 4.25: Experimental compound open-channel: (**a**) Photograph from upstream (zoom of artificial grass); (**b**) Illustration of cross-section. Adapted from Brito et al. (2016).

"The experiments were carried out in a compound open-channel located at the National Laboratory for Civil Engineering, in Lisbon. The channel is 10 m long, 2 m wide, and has longitudinal slope of 1.1×10^{-3} m/m (Fig. 4.25a). The cross-section is symmetrical, composed of two lateral FP, 0.7 m wide each, and one trapezoidal MC, 0.4 m wide, and $h_b = 0,1$ m high. The transition between the MC and FP is made by banks with 45° slope and half cross-section is $B = 1$ m wide (Fig. 4.25b). A Cartesian coordinate system is used in which x, y and z refer to the longitudinal, lateral and vertical directions, respectively (see Fig. 4.25a), and u, v and w are the components of instantaneous velocity. The system origin is defined as: $x = 0$ at the inlet cross-section; $y = 0$ at middle of the MC; and $z = 0$ at the MC bottom (see Fig. 4.25b). The MC is made of polished concrete with Nikuradse's absolut roughness $k_S = 0.15$ mm." (Brito et al., 2016). Two experiments were conducted with two different relative height (h_r) values, $h_r = 0.15$ and $h_r = 0.30$. However, given that only the latter's mesh was fully described in the published work, and **porousSimpleFOAM** results with the same number and distribution of elements did not allow for a convergence of residuals under the same simulation parameters, it was decided to focus merely on trying to reproduce the results obtained under $h_r = 0.30$. Submerged vegetation parameters are as described in Table 4.5 and a summary of experimental conditions for $h_r = 0.30$ in Table 4.6.

Table 4.5: Submerged vegetation and porosity parameters for Brito et al. (2016) $h_r = 0.30$ experimental study

h_v [mm]	d_v [mm]	ΔS [mm]	a [mm^{-1}]	φ [-]	ϕ [-]	λ [-]	K [m^2]	β [m^{-1}]
5.5	1.1	3.9	0.07	0.06	0.94	0.40	$2.46\times10^{-}6$	100

Brito et al. (2016) made use of the commercial software package ANSYS-CFX which

Table 4.6: Summary of experimental conditions for Brito et al. (2016) $h_r = 0.30$

h_{MC} [mm]	h_{FP} [mm]	h_{FP}/h_v [-]	Q_{FP} [l·s^{-1}]	Q_{MC} [l·s^{-1}]	U_{FP} [m·s^{-1}]	U_{MC} [m·s^{-1}]	U_A [m·s^{-1}]
143	43	7.8	16.6	42.3	0.28	0.56	0.43

models the free flow with the RANS equations and the porous media flow with the VARANS equations. Turbulence was modelled using the EARSM model included in the ANSYS-CFX package and the free surface was modelled using the Volume of Fluid (VoF) method described in Nichols (1981).

"In the upstream section a velocity inlet condition is imposed, assuming a uniform distribution in MC and FP computed from the experimental Q_{MC} and Q_{FP}, respectively, for each $h_r = 0.15$ and 0.30 (Table 4.6).

At the downstream cross-section of the computational domain a *pressure outlet* condition is applied, being the pressure determined by and hydrostatic distribution calculated from the measured water depth. This boundary condition is useful to simulate free-surface flows, especially when the free-surface level is know at a given downstream cross-section. This allows the domain size reduction and, consequently, the diminution of the number of mesh elements and the computational time. For boundaries with solid walls a *no slip wall* condition is used, implying normal and tangential velocities equal to zero. To solve the velocity numerically the law-of-the-wall is used.

(...)

[This is done] in order to limit the computation domain in the vertical direction, an opening boundary condition was applied in the top of the air region $C = 0$, allowing the fluid to cross the boundary surface in either direction maintaining a zero pressure (Versteeg and Malalasekera, 2007).

A scheme of the computational domain and boundary conditions used in this study is presented in the Fig. 4.26. In the computational domain the mesh was optimized by reducing the number of elements where small gradients of velocity, pressure and volume fraction are expected, and vice-versa. Therefore, the mesh is refined in the vertical direction near the free-surface due to high gradients of C and also near the bottom and the porous media top, due to high gradients of velocity. In the interface region between MC and FP the mesh is refined both in vertical and horizontal due to high gradients of velocity associated with the mixing-layer and secondary currents. Near the lateral walls the mesh is refined in the horizontal direction due to high gradients of velocity. Outside those refined regions the mesh is progressively coarser. All these criteria allow the convergence of residuals and ensure a good precision of the numerical solution (Versteeg and Malalasekera, 2007). In Fig. 4.27 a cross-sectional view of the mesh is presented. The discretization in the longitudinal direction x is coarser and uniform with 1000 elements (el.), representing the entire length of the channel (i.e. 10 m). It should be noted that the

size of elements in this direction is approximately ten times greater than the measured average diameter of vegetation and it was chosen after a mesh convergence analysis (not presented here)" (Brito et al., 2016).

In this work, given that there is a wall with slip condition as a replacement for the free surface, mesh refinement in the vertical z direction was taken as a single progression, more refined at the bottom of the channel.

The numerical study in Brito et al. (2016) was conducted with the use of the EARSM turbulence model in order to accurately simulate the formation and effects of secondary flows on the streamwise velocity. In this work we will only consider the BSL-EARSM and **NonlinearKEShih** for reasons already stated.

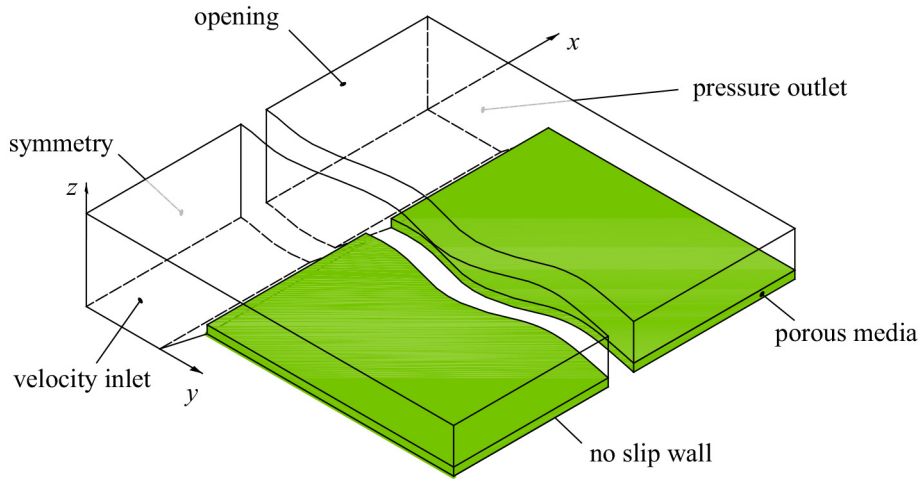

Figure 4.26: Scheme of the computational domain and boundary conditions for numerical study in Brito et al. (2016).

For the numerical simulation in Brito et al. (2016) it was necessary to choose the time step. This parameter is important because due to that solver having a time derivation. "The use of inappropriate values can cause loss of information and the non-convergence of the residual components of velocity, volume fraction, turbulence kinetic energy, turbulence dissipation and/or conservation of mass. Thus a time step $\Delta t = 0.01\ s$ was chosen (...)" (Brito et al., 2016).

For Brito et al. (2016) the "simulations were stopped when the convergence criteria were met. During the run three velocity components and pressure were monitored using monitor points throughout the computational domain. When the monitored values reached the asymptotic range and kept constant for at least 5000 time-steps, and if the root mean square normalized values of the equation residuals were below the residual target value, set to 10^{-6}, then the run is terminated. The simulation is assumed to be converged if two previous criteria met and if global unbalances are less than 0.01 % (...). The general procedure to establish the mesh was starting with a very fine mesh in all domain and then increase the size of the mesh elements keeping the errors of the monitoring points bellow 1 %. Afterwards, the mesh elements are increased in regions were

the gradients are smooth".

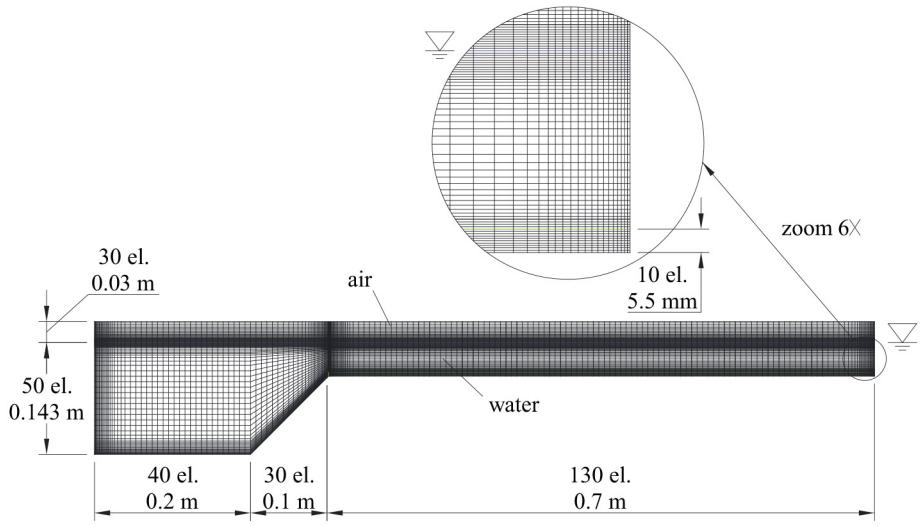

Figure 4.27: Cross-sectional view of the computational mesh for $h_r = 0.30$ in Brito et al. (2016).

As mentioned previously, the only numerical study that was able to be successfully conducted in this work was that for the case of $h_r = 0.30$, with the $h_r = 0.15$ case failing after numerous attempts with both finer and coarser meshes and varying turbulence model parameters, which always resulted in the simulation "blowing-up" in the first few time-steps.

Bulk flow rates for both MC and FP were provided in the experimental characterisation by Brito et al. (2016), as such (and as expected taking Section 4.1 into account) the BSL-EARSM turbulence model yielded the closest results to Brito et al. (2016) numerical study which, like Filonovich et al. (2010), made use of the EARSM turbulence model, and the **NonlinearKEShih** once again making wildly different predictions in terms of secondary current topology and placement as well as their influence on the stream-wise velocity distribution (Figures 4.29a and 4.33a, respectively).

However, the stream-wise isovels of Brito et al. (2016) in Figures 4.28 compared to the BSL-EARSM case of this work in Figure 4.33b show a closer agreement albeit with the same velocity over-prediction as detected in Section 4.1, and also a different velocity distribution across the FP.

The vertical time averaged stream-wise velocity profiles of Brito et al. (2016) and this work (Figures 4.30 and 4.31, respectively) illustrate both the noticeable over-prediction and stream-wise velocity distribution at two span-wise locations in the FP at $x = 7.5$ m.

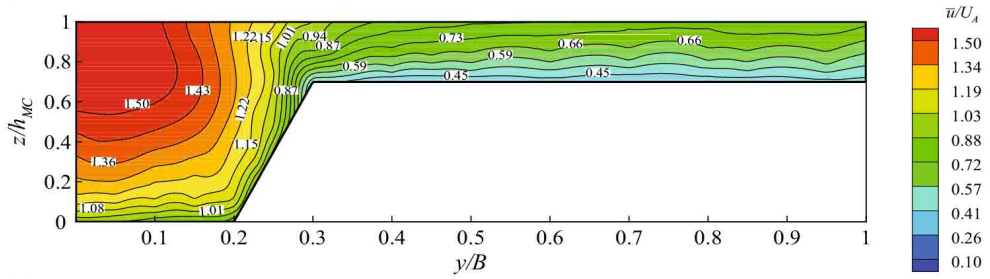

(a) Experimental.

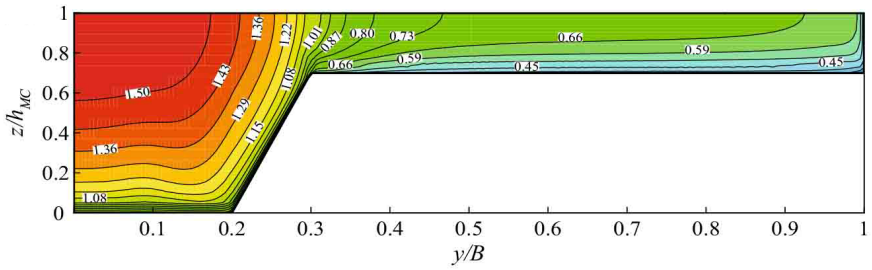

(b) Numerical.

Figure 4.28: Time-averaged stream-wise velocity field for $h_r = 0.30$. Adapted from Brito et al. (2016).

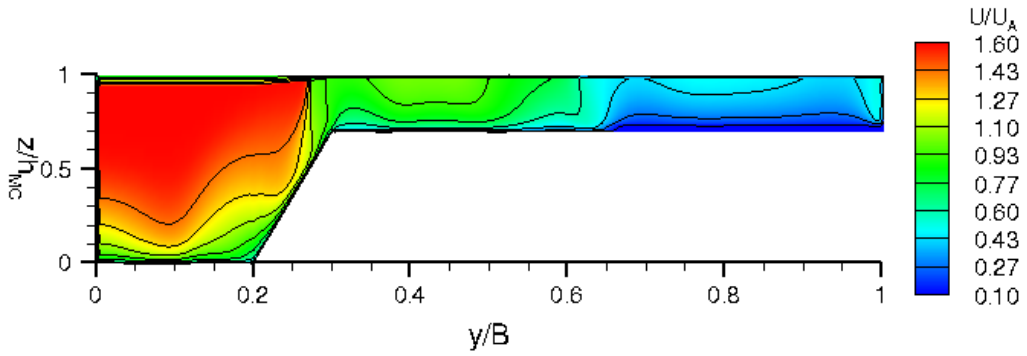

(a) **NonlinearKEShih**.

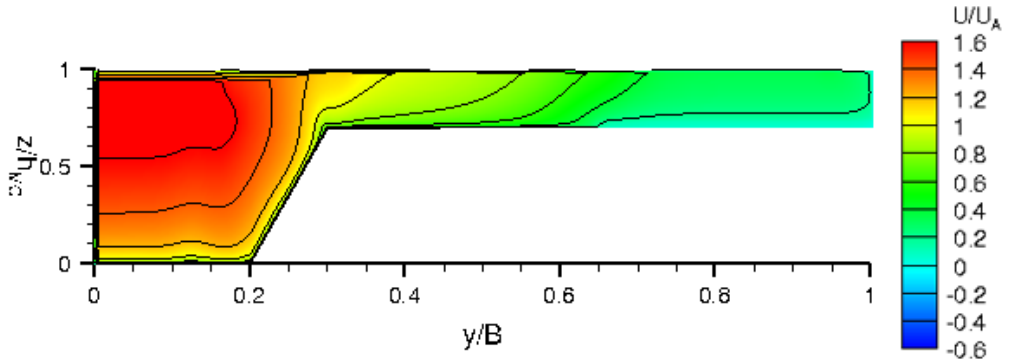

(b) BSL-EARSM.

Figure 4.29: Normalised stream-wise isovel plot for numerical study of Brito et al. (2016) $h_r = 0.30$ in OpenFOAM.

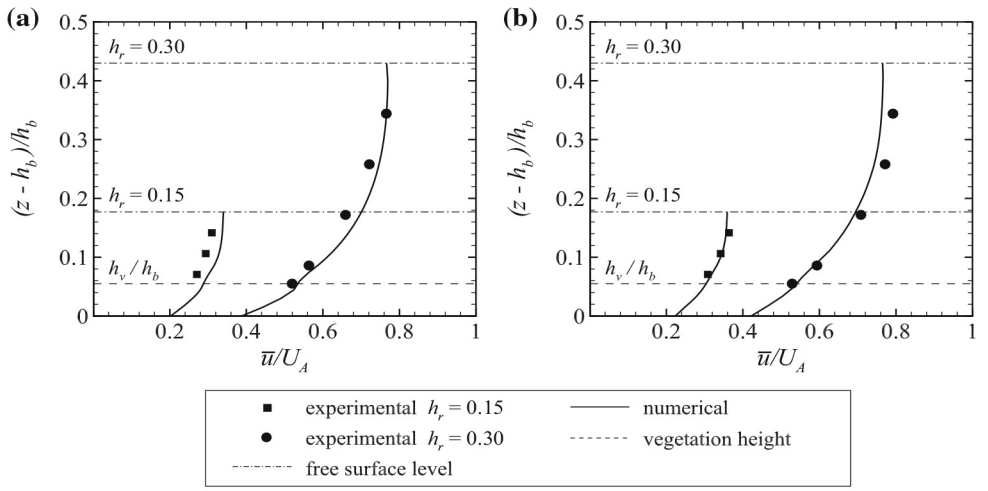

Figure 4.30: Vertical time averaged stream-wise velocity profile: (**a**) $y/B = 0.40$; (**b**) $y/B = 0.60$. Adapted from Brito et al. (2016).

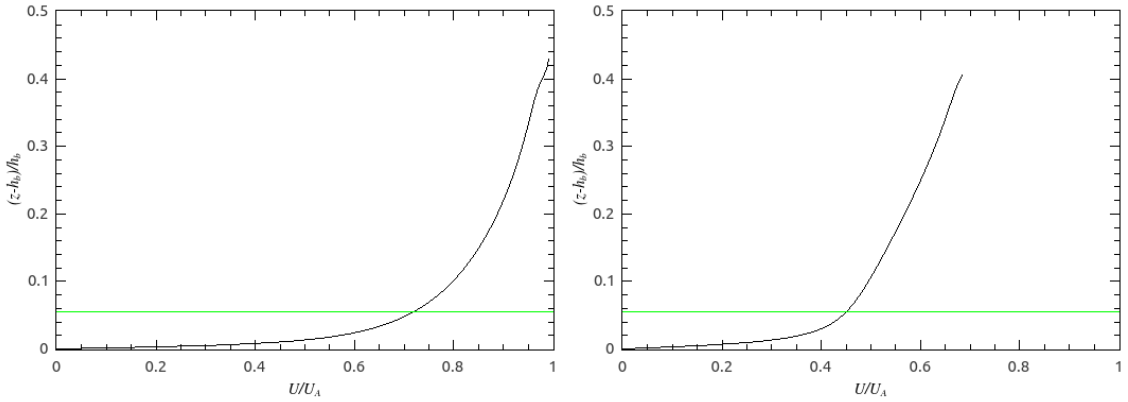

(a) $y/B = 0.4$. (b) $y/B = 0.6$.

Figure 4.31: Vertical time averaged stream-wise velocity profile for numerical study of Brito et al. (2016) $h_r = 0.30$ in OpenFOAM.

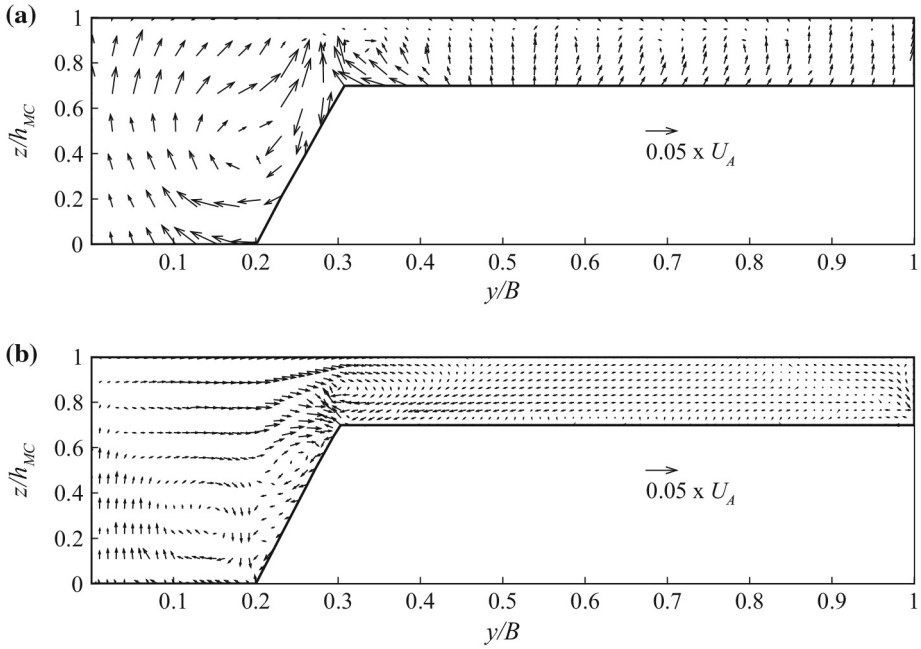

Figure 4.32: Secondary currents for $h_r = 0.30$: (**a**) experimental; (**b**) numerical. Adapted from Brito et al. (2016).

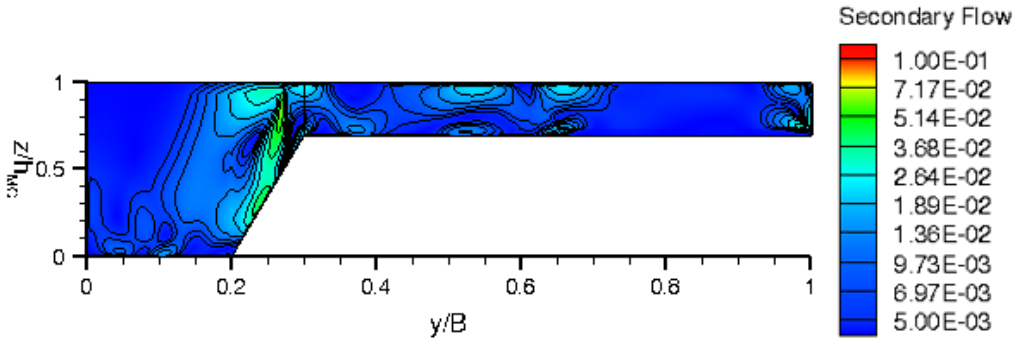

(a) **NonlinearKEShih**.

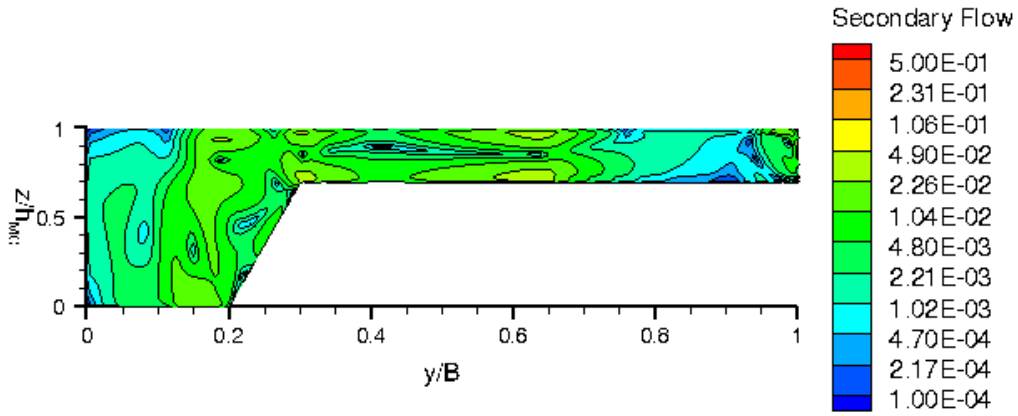

(b) BSL-EARSM.

Figure 4.33: Normalized secondary flow plot for numerical study of Brito et al. (2016) $h_r = 0.30$ in OpenFOAM.

Chapter 5

Conclusions and Future Studies

5.1 Conclusions

In the present study several numerical simulations of non-vegetated and vegetated (with analogous porous-media), simple and compound channel flows with both eddy-viscosity and algebraic turbulence models were performed using the open-source CFD toolbox OpenFOAM. The results of these simulations were presented in Chapter 4.

Regarding the objectives established in Chapter 1, Section 1.2, and the methodology laid out in the introduction of Chapter 4, the following conclusions can be listed:

- The **porousSimpleFoam** solver is adequate for the simulation of compound open-channel channel flow provided an adequate turbulence model is used.
- The use of non-linear eddy viscosity models in OpenFOAM is not straightforward in its application. The quadratic model **NonlinearKEShih** by Shih et al. (1994) fails to adequately model Prandtl's second type of secondary currents which in turn severely affects stream-wise velocity profiles across the entire channel cross-section. The cubic turbulence model **LienCubicKE** proved difficult to implement, with further considerations as to boundary conditions and near-wall mesh refinement likely necessary for a more thorough analysis of its applicability.
- The implementation by Jeyapaul (2015) and Yogesh (2017) of the BSL-EARSM turbulence model by Menter et al. (2012) produces significantly agreeable results. However, a more comprehensive comparative study should be conducted to account for the differences in implementation of the original model proposed by Menter et al. (2012), especially in regards to open-channel flow.
- The implementation of the Darcy-Forchheimer porosity model to OpenFOAM is demonstrated to be severely lacking in robustness for the types of flow in this work.

Even though it is able to account for anisotropy in the porous media if need be, the following characteristics of its implementation invalidate the OpenFOAM toolbox for the use of the technique implemented in this work (hybrid media flow):

  - The RANS equations used by the solver merely apply a drag term in the porous zones of the mesh (Equations 3.1 and 3.3), a term which is based on the classic Darcy-Forchheimer equation (Equation 2.38) but lacking in that it doesn't take into account the Darcy velocity $\mathbf{u}_D$ (Equation 2.31).
  - The solver doesn't apply a volumetric average to the RANS equations in the porous zones so as to discount the geometric inconsistencies of the REV, for which it should use the Dupuit-Forschheimer relationship for the Darcy velocity $\mathbf{u}_D$ (Equation 2.53).
  - There is no native type of submerged patch in OpenFOAM to which interface conditions can be set to account for the discontinuity in shear stresses present at the interface between the porous media and free-flow as described in Chapter 2, Sub-section 2.3.5.

- The cumulative effect of the conclusions listed above explain why the numerical simulations based on the experiments of Lopez and Garcia (1997) and Nezu and Sanjou (2008) failed to achieve convergence of the monitored residuals, despite the geometric simplicity of the channel cross-section. The fact that a porous zone was present across the entire channel cross-section exacerbated the problems listed as the flow was unable to develop properly and fully, as it was continuously having to deal with the shear-stress discontinuity across the entire flow length and span. This conclusion is reinforced by the fact that monitored residual quantities are higher, or even highly unstable once non-linear eddy viscosity or algebraic turbulence models (*i.e.*, models that account for secondary flow) are implemented.

- In agreement with the previous point are the cases by Brito et al. (2016), where only the case with the higher relative depth $h_r = 0.30$ was able to produce a valid numerical simulation, in this work, for these cases. For the case of $h_r = 0.15$ where there is a greater disparity in depth-averaged velocity (normalized for cross section bulk velocity) between the MC and FP (Brito et al., 2016), the shear-stress discontinuities prevented the solver from converging into a stable and agreeable solution. However, for the $h_r = 0.30$ case the higher h_{FP} along with the unobstructed MC allowed for a development of secondary flow cells (Figure 4.33b) of a magnitude and placement that the shear-stress discontinuities did not preclude the solver from converging to a stable solution. Even so, the stream-wise velocity profiles across the FP are inadequate (Figures 4.30 and 4.31). Given that the comparative studies for the cases of Filonovich et al. (2010) and Filonovich et al. (2014) showed some discrepancies between the numerical studies of those works with that of this one, one cannot at this time attribute all of the faults of the numerical study of this case

to the lack of sophistication of the present porous model in OpenFOAM. However, given the reasons listed so far, it is the likely major culprit.

In summary the present porous media model implemented in the OpenFOAM toolbox (up to version 2.40) is insufficient for the implementation of the simplification of the porous media model to a submerged rigid vegetation patch in open-channel flow, as it doesn't include the necessary modelling considerations for hybrid media flow as succinctly described by Lemos (2006).

5.2 Future Studies

The advantage of the OpenFOAM toolbox is in its versatility and customizability for researchers who need to test the implementation of new models, and its community based development. As such the implementation of a more robust porosity model should be undertaken given that the methodology tested in this work has been validated in previous studies with the use of commercial software solutions (Brito et al., 2016; Sonnenwald et al., 2016).

A VARANS based approach to porous media should be implemented. This has been demonstrated in works by Chen et al. (2015) and Higuera Caubilla (2015).

The model description for hybrid media by Lemos (2006) should be applied both for laminar flow (as presented in Sub-section 2.3.5) and turbulent flow (which is more complex than the laminar flow presented here), taking into account the need to implement an interface boundary condition to account for the shear stress discontinuity, especially with the use of a robust RSM model such as BSL-EARSM. This can be done without having to alter the OpenFOAM source code directly by using the SWiss Army Knife for FOAM (SWAK4FOAM) toolbox for OpenFOAM, in particular the **groovyBC** boundary condition that allows arbitrary expressions in the field-file.

Further work can also focus on the use of alternate differentiation schemes set in the `fvSchemes` dictionary file, as well as different under-relaxation factor values for fields and equations set in the `fvSolutions` dictionary file. These studies should be conducted so as to verify if the current porosity modelling in OpenFOAM is in fact completely unsuitable for this type of flow, or if it's possible to attenuate the porous media interface discontinuities mentioned in Sub-section 2.3.5.

In regards to the validity of the porous media as analogue to submerged vegetation method, further validation of the method taking into consideration the experimental cases by Lopez and Garcia (1997) and Nezu and Sanjou (2008) considered in this work should be conducted by following the procedures of Brito et al. (2016) and Sonnenwald et al. (2016), and their respective numerical tools.

Further studies of this technique should also contemplate its applicability to submerged flexible canopies (Appendix A.1), taking into consideration the modelling of anelastic deformation of porous media (Kolymbas, 1984).

Bibliography

Ackers, P. (1993a). "Stage-Discharge Functions for Two-Stage Channels: The Impact of New Research". en. In: *Water and Environment Journal* 7.1, pp. 52–59. ISSN: 1747-6585, 1747-6593. DOI: 10.1111/j.1747-6593.1993.tb00810.x. URL: http://doi.wiley.com/10.1111/j.1747-6593.1993.tb00810.x (visited on 11/07/2016).

Ackers, P. (1993b). "Flow formulae for straight two-stage channels". en. In: *Journal of Hydraulic Research* 31.4, pp. 509–531. ISSN: 0022-1686, 1814-2079. DOI: 10.1080/00221689309498874. URL: http://www.tandfonline.com/doi/abs/10.1080/00221689309498874 (visited on 11/07/2016).

Andersen, O. H. and H. F. Burcharth (1995). "On the One-Dimensional Steady and Unsteady Porous Flow Equation". In: *Coastal Engineering* 24, pp. 233–257.

Barree, R. and M. Conway (2004). "Beyond Beta Factors: A Complete Model for Darcy, Forchheimer, and Trans-Forchheimer Flow in Porous Media". In: Society of Petroleum Engineers. DOI: 10.2118/89325-MS. URL: http://www.onepetro.org/doi/10.2118/89325-MS (visited on 09/29/2016).

Bauer, M. (2017a). *2.3.4. Explicit Algebraic Reynolds Stress Model*. URL: https://www.sharcnet.ca/Software/Ansys/16.2.3/en-us/help/cfx_thry/thry_turb_earsm.html (visited on 06/14/2017).

— (2017b). *4.1.7. The Reynolds Stress Model*. en. URL: https://www.sharcnet.ca/Software/Ansys/16.2.3/en-us/help/cfx_mod/i1346049.html (visited on 06/12/2017).

Bazdidi-Tehrani, F., A. Mohammadi-Ahmar, M. Kiamansouri, and M. Jadidi (2015). "Investigation of various non-linear eddy viscosity turbulence models for simulating flow and pollutant dispersion on and around a cubical model building". en. In: *Building Simulation* 8.2, pp. 149–166. ISSN: 1996-3599, 1996-8744. DOI: 10.1007/s12273-014-0199-y. URL: http://link.springer.com/10.1007/s12273-014-0199-y (visited on 11/25/2016).

Bear, J. (1988). *Dynamics of fluids in porous media*. Dover books on physics and chemistry. New York: Dover. ISBN: 978-0-486-65675-5.

Bear, J. and M. Y. Corapcioglu, eds. (1984). *Fundamentals of Transport Phenomena in Porous Media*. Dordrecht: Springer Netherlands. ISBN: 978-94-009-6177-7 978-94-009-6175-3.

Boussinesq, J. (1877). *Essai Sur La Theorie Des Eaux Courantes*. French. 3rd. Vol. 1. XXIII. Paris: Imprimerie Nationale. URL: http://gallica.bnf.fr/ark:/12148/bpt6k56673076.

Box, G. E. P. and N. R. Draper (1987). *Empirical model-building and response surfaces*. eng. 7. Dr. Wiley series in probability and mathematical statistics. Applied probability and statistics. OCLC: 832443831. New York: Wiley. ISBN: 978-0-471-81033-9.

Brinkman, H. C. (1949). "A calculation of the viscous force exerted by a flowing fluid on a dense swarm of particles". en. In: *Flow, Turbulence and Combustion* 1.1. ISSN: 1386-6184, 1573-1987. DOI: 10.1007/BF02120313. URL: http://link.springer.com/10.1007/BF02120313 (visited on 10/12/2016).

Brito, M., J. Fernandes, and J. B. Leal (2016). "Porous media approach for RANS simulation of compound open-channel flows with submerged vegetated floodplains". en. In: *Environmental Fluid Mechanics* 16.6, pp. 1247–1266. ISSN: 1567-7419, 1573-1510. DOI: 10.1007/s10652-016-9481-0. URL: http://link.springer.com/10.1007/s10652-016-9481-0 (visited on 11/14/2016).

Brock, R. R. (1991). "Dupuit-Forchheimer theories for the shape of groundwater recharge mounds". en. In: *Journal of Hydrology* 124.3-4, pp. 279–291. ISSN: 00221694. DOI: 10.1016/0022-1694(91)90019-E. URL: http://linkinghub.elsevier.com/retrieve/pii/002216949190019E (visited on 06/25/2017).

Buchart, H. F. and C. Christensen (1911). "On Stationary and Non-stationary Porous Flow in Coarse Granular Materials". English. In: *MAST G6-S: Project 1*. Wave Action on and in coastal structures.

Cantanbria, U. (2014). *IHFOAM Manual*. en.

Cebeci, T. (2004). *Analysis of turbulent flows*. 2nd rev. a. Amsterdam ; Boston: Elsevier, p. 376. ISBN: 978-0-08-044350-8.

CFD Direct (2014). *OpenFOAM - The Open Source CFD Toolbox - User's Guide*. en. 2.3.1. United Kingdom: OpenCFD Ltd. URL: https://openfoam.org/.

— (2017). *About OpenFOAM*. en. URL: https://cfd.direct/openfoam/about/ (visited on 03/01/2017).

CFD-Online (2016). *CFD Online - Turbulence Properties, Conversions & Boundary Estimations*. URL: http://www.cfd-online.com/Tools/turbulence.php (visited on 07/11/2016).

— (2017). *RANS-based turbulence models*. URL: https://www.cfd-online.com/Wiki/RANS-based_turbulence_models (visited on 01/13/2017).

Chen, Z., C. Li, and J. Zhan (2015). "Simulation of Flows through Submerged Vegetation Patches Using Macroscopic Turbulence Models". In: *Procedia Engineering*. Frontiers in Fluid Mechanics Research 126, pp. 315–320. ISSN: 1877-7058. DOI: 10.1016/j.proeng.2015.11.194.

Cheng, N.-S., Z. Hao, and S. K. Tan (2008). "Comparison of quadratic and power law for nonlinear flow through porous media". en. In: *Experimental Thermal and Fluid Science* 32.8, pp. 1538–1547. ISSN: 08941777. DOI: 10.1016/j.expthermflusci.2008.04.

007. URL: http://linkinghub.elsevier.com/retrieve/pii/S0894177708000526 (visited on 03/19/2017).

Cokljat, D. and B. A. Younis (1995). "Second-Order Closure Study of Open-Channel Flows". en. In: *Journal of Hydraulic Engineering* 121.2, pp. 94–107. ISSN: 0733-9429, 1943-7900. DOI: 10.1061/(ASCE)0733-9429(1995)121:2(94). (Visited on 11/14/2016).

Cokljat, D. P. (1993). "Turbulence models for non-circular ducts and channels." en. Unpublished Doctoral thesis. City University London. URL: http://openaccess.city.ac.uk/id/eprint/8019.

Darby, S. E. (1999). "Effect of Riparian Vegetation on Flow Resistance and Flood Potential". en. In: *Journal of Hydraulic Engineering* 125.5, pp. 443–454. ISSN: 0733-9429, 1943-7900. DOI: 10.1061/(ASCE)0733-9429(1999)125:5(443). URL: http://ascelibrary.org/doi/10.1061/%28ASCE%290733-9429%281999%29125%3A5%28443%29 (visited on 06/16/2017).

Dijkstra, J. T. and R. E. Uittenbogaard (2010). "Modeling the interaction between flow and highly flexible aquatic vegetation: FLOW AND FLEXIBLE VEGETATION". en. In: *Water Resources Research* 46.12. ISSN: 00431397. DOI: 10.1029/2010WR009246. URL: http://doi.wiley.com/10.1029/2010WR009246 (visited on 06/25/2017).

Durbin, P. A. (2009). "Limiters and wall treatments in applied turbulence modeling". In: *Fluid Dynamics Research* 41.1, p. 012203. URL: http://stacks.iop.org/1873-7005/41/i=1/a=012203.

Dybbs, A. and R. V. Edwards (1994). en. In: NATO ASI Series 82, pp. 199–256.

Ehrhard, J. and N. Moussiopoulos (2000). "On a new nonlinear turbulence model for simulating flows around building-shaped structures". en. In: *Journal of Wind Engineering and Industrial Aerodynamics* 88.1, pp. 91–99. ISSN: 01676105. DOI: 10.1016/S0167-6105(00)00026-X. URL: http://linkinghub.elsevier.com/retrieve/pii/S016761050000026X (visited on 03/23/2017).

Ergun, S. (1952). "Fluid flow through packed columns". en. In: *Chemical Engineering Progress* 89, pp. 89–94.

Etemad, S., B. Sunden, and O. Daunius (2006). "Turbulent flow and heat transfer in a square-sectioned U-bend". In: *Progress in Computational Fluid Dynamics An International Journal* 6 (1/2/3). DOI: 10.1504/pcfd.2006.009486.

Experts Exchange (2015). *Processing Power Compared*. en. URL: http://pages.experts-exchange.com/processing-power-compared/ (visited on 03/22/2017).

Filonovich, M. (2015). "Numerical modelling of compound channel flow". English. doctoralThesis. Almada: Universidade Nova de Lisboa, Faculdade de Ciências e Tecnologia. URL: https://run.unl.pt/handle/10362/14993.

Filonovich, M., R. Azevedo, L. R. Rojas-Solórzano, and J. B. Leal (2010). "Simulation of the velocity field in compound channel flows using different closure models". eng. In: IAHR. URL: http://hdl.handle.net/10362/5032.

Filonovich, M., J. B. Leal, and L. R. Rojas-Solórzano (2014). "Prediction of compound channel secondary flows using anisotropic turbulent models". eng. In: *River Flow 2014: proceedings of the International Conference on Fluvial Hydraulics (River Flow 2014), Lausanne, Switzerland, 3 - 5 September 2014*. Ed. by A. J. Schleiss, G. De Cesare, M. J. Franca, and M. Pfister. A Balkema Book. Boca Raton London New York Leiden: CRC Press/Balkema. ISBN: 978-1-138-02674-2.

Fischer-Antze, T., T. Stoesser, P. Bates, and N. Olsen (2001). "3D numerical modelling of open-channel flow with submerged vegetation". In: *Journal of Hydraulic Research* 39.3, pp. 303–310. ISSN: 0022-1686. DOI: 10.1080/00221680109499833.

Ford, C., J. Carrotte, and A. Walker (2013). "The application of porous media to simulate the upstream effects of gas turbine injector swirl vanes". en. In: *Computers & Fluids* 77, pp. 143–151. ISSN: 00457930. DOI: 10.1016/j.compfluid.2013.03.001. URL: http://linkinghub.elsevier.com/retrieve/pii/S0045793013000844 (visited on 12/09/2016).

Forum, M. P. I. (1994). *MPI: A Message-Passing Interface Standard*. Tech. rep. Knoxville, TN, USA. URL: http://mpi-forum.org/docs/.

Franke, M., S. Wallin, and F. Thiele (2005). "Assessment of explicit algebraic Reynolds-stress turbulence models in aerodynamic computations". en. In: *Aerospace Science and Technology* 9.7, pp. 573–581. ISSN: 12709638. DOI: 10.1016/j.ast.2005.06.002. URL: http://linkinghub.elsevier.com/retrieve/pii/S1270963805000805 (visited on 02/01/2017).

Geuzaine, C. and J.-F. Remacle (2009). "Gmsh: a three-dimensional finite element mesh generator with built-in pre- and post-processing facilities". en. In: *International Journal for Numerical Methods in Engineering* 11.79, pp. 1309–1331.

Ghisalberti, M. (2005). "Momentum and scalar transport in vegetated shear flows". en. PhD Thesis. Massachusetts Institute of Technology: Massachusetts Institute of Technology. Dept. of Civil and Environmental Engineering. URL: http://dspace.mit.edu/handle/1721.1/31136.

Ghisalberti, M. and H. Nepf (2006). "The structure of the shear layer in flows over rigid and flexible canopies". In: *Environmental Fluid Mechanics* 6.3, pp. 277–301. ISSN: 15677419. DOI: 10.1007/s10652-006-0002-4.

Gooya, R. (2014). *Description of porousSimpleFoam and adding the Brinkman model to the porous models - Developed for OpenFOAM-2.2.x*. en. (Visited on 10/10/2016).

Gray, W. and P. Lee (1977). "On the theorems for local volume averaging of multiphase systems". en. In: *International Journal of Multiphase Flow* 3.4, pp. 333–340. ISSN: 03019322. DOI: 10.1016/0301-9322(77)90013-1. URL: http://linkinghub.elsevier.com/retrieve/pii/0301932277900131 (visited on 06/22/2017).

Hafsteinsson, H. E. (2009). *Porous Media in OpenFOAM*. en. Tutorial. Chalmers University of Technology, p. 14. URL: http://www.tfd.chalmers.se/~hani/kurser/OS_CFD_2008/HaukurElvarHafsteinsson/haukurReport.pdf (visited on 03/06/2017).

Handley, D. and P. Heggs (1968). "Momentum and heat transfer mechanisms in regular shaped packings". In: *Trans. Inst Chem. Eng.* 9.46, pp. 251–264.

Hansen, C. D. and C. R. Johnson, eds. (2005). *The visualization handbook*. eng. OCLC: 249539637. Amsterdam: Elsevier/Butterworth-Heinemann. ISBN: 978-0-12-387582-2.

Higuera Caubilla, P. (2015). "Application of Computational Fluid Dynamics to Wave Action on Structures". en. PhD Thesis. Cantabria, Spain: Universidad de Cantabria.

— (2017). *What is what and who is who in the OpenFOAM environment? - olaFoam*. URL: https://sites.google.com/site/olafoamcfd/blog/ (visited on 03/01/2017).

Holzmann, T. (2016). *Mathematics, Numerics, Derivations and OpenFOAM(R)*. en. Fourth edition. Leoben, Austria: Holzmann CFD. URL: www.holzmann.

Hsu, C. and P. Cheng (1990). "Thermal dispersion in a porous medium". en. In: *International Journal of Heat and Mass Transfer* 33.8, pp. 1587–1597. ISSN: 00179310. DOI: 10.1016/0017-9310(90)90015-M. URL: http://linkinghub.elsevier.com/retrieve/pii/001793109090015M (visited on 06/25/2017).

Hu, Z., M. Stive, T. Zitman, and T. Suzuki (2012). "DRAG COEFFICIENT OF VEGETATION IN FLOW MODELING". In: *Coastal Engineering Proceedings* 1.33. ISSN: 2156-1028, 0589-087X. DOI: 10.9753/icce.v33.posters.4. URL: http://journals.tdl.org/icce/index.php/icce/article/view/6405 (visited on 06/23/2017).

Jambhekar, V. A. (2011). "Forchheimer Porous-media Flow Models, Numerical Investigation and Comparison with Experimental Data". mastersThesis. Stuttgart: Universität Stuttgart.

Jasak, H. (1996). "Error Analysis and Estimation for the Finite Volume Method with Applications to Fluid Flows". en. PhD Thesis. London: University of London. URL: https://books.google.pt/books?id=_ghlHAAACAAJ.

Jeyapaul, E. (2015). *ejp / BSL-EARSM · GitLab*. URL: https://gitlab.com/ejp/BSL-EARSM (visited on 08/24/2016).

Jones, W. and B. Launder (1972). "The prediction of laminarization with a two-equation model of turbulence". In: *International Journal of Heat and Mass Transfer* 15 (2). DOI: 10.1016/0017-9310(72)90076-2.

Joodi, A. S., S. Sizaret, S. Binet, A. Bruand, P. Alberic, and M. Lepiller (2010). "Development of a Darcy-Brinkman model to simulate water flow and tracer transport in a heterogeneous karstic aquifer (Val d'Orléans, France)". en. In: *Hydrogeology Journal* 18.2, pp. 295–309. ISSN: 1431-2174, 1435-0157. DOI: 10.1007/s10040-009-0536-x. URL: http://link.springer.com/10.1007/s10040-009-0536-x (visited on 10/12/2016).

Kang, H. and S.-U. Choi (2006). "Turbulence modeling of compound open-channel flows with and without vegetation on the floodplain using the Reynolds stress model". en. In: *Advances in Water Resources* 29.11, pp. 1650–1664. ISSN: 03091708. DOI: 10.1016/j.advwatres.2005.12.004. URL: http://linkinghub.elsevier.com/retrieve/pii/S0309170805002952 (visited on 11/21/2016).

Kang Hyeongsik; Choi, S.-U. (2006). "Reynolds stress modelling of rectangular open-channel flow". In: *International Journal for Numerical Methods in Fluids* 51 (11). DOI: 10.1002/fld.1157.

Kara, S., T. Stoesser, and T. W. Sturm (2012). "Turbulence statistics in compound channels with deep and shallow overbank flows". en. In: *Journal of Hydraulic Research* 50.5, pp. 482–493. ISSN: 0022-1686, 1814-2079. DOI: 10.1080/00221686.2012.724194. URL: http://www.tandfonline.com/doi/abs/10.1080/00221686.2012.724194 (visited on 11/21/2016).

Keller, R. J. and W. Rodi (1988). "Prediction of flow characteristics in main channel/flood plain flows". en. In: *Journal of Hydraulic Research* 26.4, pp. 425–441. ISSN: 0022-1686, 1814-2079. DOI: 10.1080/00221688809499202. URL: http://www.tandfonline.com/doi/abs/10.1080/00221688809499202 (visited on 11/17/2016).

Knight, D. W. and K. Shiono (1990). "Turbulence measurements in a shear layer region of a compound channel". en. In: *Journal of Hydraulic Research* 28.2, pp. 175–196. ISSN: 0022-1686, 1814-2079. DOI: 10.1080/00221689009499085. URL: http://www.tandfonline.com/doi/abs/10.1080/00221689009499085 (visited on 11/21/2016).

Knight, D. W., N. Wright, and H. Morvan (2005). *Guidelines for applying commercial CFD software to open channel flow*. en.

Knight, D. W., M. Omran, and X. Tang (2007). "Modeling Depth-Averaged Velocity and Boundary Shear in Trapezoidal Channels with Secondary Flows". en. In: *Journal of Hydraulic Engineering* 133.1, pp. 39–47. ISSN: 0733-9429, 1943-7900. DOI: 10.1061/(ASCE)0733-9429(2007)133:1(39). URL: http://ascelibrary.org/doi/10.1061/%28ASCE%290733-9429%282007%29133%3A1%2839%29 (visited on 11/15/2016).

Kolmogorov, A. (1942). "The equations of turbulent motion in an incompressible fluid." RUS. In: *Izvestia Acad. Sci.* Vol. 6. USSR, pp. 56–58.

Kolymbas, D. (1984). "Anelastic Deformation of Porous Media". In: *Fundamentals of Transport Phenomena in Porous Media*. Ed. by J. Bear and M. Y. Corapcioglu. Dordrecht: Springer Netherlands, pp. 499–524. ISBN: 978-94-009-6177-7 978-94-009-6175-3. URL: http://link.springer.com/10.1007/978-94-009-6175-3 (visited on 04/12/2016).

Lai, B., J. L. Miskimins, and Y.-S. Wu (2009). "Non-Darcy Porous Media Flow According to the Barree and Conway Model: Laboratory and Numerical Modeling Studies". English. In: *2009 SPE Rocky Mountain Petroleum Technology Conference*. Denver, Colorado, USA.

Lambert, M. F. and W. R. Myers (1998). "ESTIMATING THE DISCHARGE CAPACITY IN STRAIGHT COMPOUND CHANNELS." en. In: *Proceedings of the Institution of Civil Engineers - Water Maritime and Energy* 130.2, pp. 84–94. ISSN: 1753-7819. DOI: 10.1680/iwtme.1998.30477. URL: http://www.icevirtuallibrary.com/doi/10.1680/iwtme.1998.30477 (visited on 11/07/2016).

Launder, B. E., G. J. Reece, and W. Rodi (1975). "Progress in the development of a Reynolds-stress turbulence closure". en. In: *Journal of Fluid Mechanics* 68.03, p. 537.

ISSN: 0022-1120, 1469-7645. DOI: 10.1017/S0022112075001814. URL: http://www.journals.cambridge.org/abstract_S0022112075001814 (visited on 01/31/2017).

Leal, J. B. (2015). *Vegetation Characteristics for Master Thesis*.

LEAP CFD Team (2012). *Computational Fluid Dynamics (CFD) Blog - LEAP Australia & New Zealand | Tips & Tricks: Convergence and Mesh Independence Study*. URL: https://www.computationalfluiddynamics.com.au/convergence-and-mesh-independent-study/,https://www.computationalfluiddynamics.com.au/convergence-and-mesh-independent-study/ (visited on 03/19/2017).

Lemos, M. J.S. d. (2006). *Turbulence in porous media: modeling and applications*. OCLC: ocm70400669. Amsterdam ; Boston: Elsevier. ISBN: 978-0-08-044491-8.

Leva, M. (1959). *Fluidization*. Series in Chemical Engineering. New York: McGraw-Hill.

Li, L. and W. Ma (2011). "Experimental Study on the Effective Particle Diameter of a Packed Bed with Non-Spherical Particles". In: *Transport in Porous Media* 89.1, pp. 35–48. ISSN: 01693913. DOI: 10.1007/s11242-011-9757-2.

Lien, F. S., W. L. Chen, and M. A. Leschziner (1996). "Low-Reynolds-number eddy-viscosity modeling based on non-linear stress-strain/vorticity relations". eng. In: *Engineering turbulence modelling and experiments 3: proceedings of the Third International Symposium on Engineering Turbulence Modelling and Measurements, Heraklion-Crete, Greece, 27 - 29 May, 1996*. Ed. by W. Rodi, G. Bergeles, and International Symposium on Engineering Turbulence Modelling and Measurements. Elsevier series in thermal and fluid sciences. OCLC: 832486611. Amsterdam: Elsevier, pp. 91–100. ISBN: 978-0-444-82463-9.

Lin, B. and K. Shiono (1995). "Numerical modelling of solute transport in compound channel flows". en. In: *Journal of Hydraulic Research* 33.6, pp. 773–788. ISSN: 0022-1686, 1814-2079. DOI: 10.1080/00221689509498551. URL: http://www.tandfonline.com/doi/abs/10.1080/00221689509498551 (visited on 11/21/2016).

Liu, H., P. R. Patil, and U. Narusawa (2007). "On Darcy-Brinkman Equation: Viscous Flow Between Two Parallel Plates Packed with Regular Square Arrays of Cylinders". en. In: *Entropy* 9.3, pp. 118–131. ISSN: 1099-4300. DOI: 10.3390/e9030118. URL: http://www.mdpi.com/1099-4300/9/3/118/ (visited on 10/12/2016).

Lopez, F. and M. Garcia (1997). *Open-Channel Flow Through Simulated Vegetation: Turbulence Modeling and Sediment Transport*. Tech. rep. DTIC Document. URL: http://oai.dtic.mil/oai/oai?verb=getRecord{\&}metadataPrefix=html{\&}identifier=ADA328041.

Macdonald, I. F., M. S. El-Sayed, K. Mow, and F. A. L. Dullien (1979). "Flow through Porous Media-the Ergun Equation Revisited". en. In: *Industrial & Engineering Chemistry Fundamentals* 18.3, pp. 199–208. ISSN: 0196-4313, 1541-4833. DOI: 10.1021/i160071a001. URL: http://pubs.acs.org/doi/abs/10.1021/i160071a001 (visited on 10/06/2016).

Madsen, O. S. and S. M. White (1976). *Reflection and transmission characteristics of porous rubble-mound breakwaters*. Tech. rep. US Army Corps of Engineers, CERC.

URL: http://repository.tudelft.nl/view/hydro/uuid:d82e594c-ed8c-4e18-b0fd-0ead288ad5a4/.

Marques, R. A. (2015). "Estudo numérico da interação de ondas com um quebra-mar poroso utilizando o código IHFOAM". Português. Master's Thesis. Almada: Universidade Nova de Lisboa, Faculdade de Ciências e Tecnologia. URL: https://run.unl.pt/handle/10362/16202.

Marriott, S. B., ed. (1999). *Floodplains: interdisciplinary approaches*. eng. Geological Society special publication 163. OCLC: 612147590. London: Geological Society. ISBN: 978-1-86239-050-8.

Mellink, B. A. (2012). "Numerical and experimental research of wave interaction with a porous breakwater". PhD thesis. URL: http://repository.tudelft.nl/view/ir/uuid:8c8d74ac-0990-4043-8d9c-ab2017719908/.

Menter, F. (1993). "[American Institute of Aeronautics and Astronautics 23rd Fluid Dynamics, Plasmadynamics, and Lasers Conference - Orlando,FL,U.S.A. (06 July 1993 - 09 July 1993)] 23rd Fluid Dynamics, Plasmadynamics, and Lasers Conference - Zonal Two Equation k-w Turbulence Models For Aerodynamic Flows". In: DOI: 10.2514/6.1993-2906.

Menter, F. R. (1994). "Two-equation eddy-viscosity turbulence models for engineering applications". In: *AIAA Journal* 32 (8). DOI: 10.2514/3.12149.

Menter, F. R., A. V. Garbaruk, and Y. Egorov (2012). "Explicit algebraic reynolds stress models for anisotropic wall-bounded flows". In: EDP Sciences, pp. 89–104. ISBN: 978-2-7598-0674-4 978-2-7598-0717-8. DOI: 10.1051/eucass/201203089. URL: http://www.eucass-proceedings.eu/10.1051/eucass/201203089 (visited on 02/01/2017).

Moukalled, F., L. Mangani, and M. Darwish (2016). *The Finite Volume Method in Computational Fluid Dynamics*. Vol. 113. Fluid Mechanics and Its Applications. DOI: 10.1007/978-3-319-16874-6. Cham: Springer International Publishing. ISBN: 978-3-319-16873-9 978-3-319-16874-6. URL: http://link.springer.com/10.1007/978-3-319-16874-6 (visited on 03/06/2017).

Moura, G. S. (2014). "Análise Teórico-Experimental de Micro Modelo de Meio Poroso". Português. PhD thesis. Rio de Janeiro, RJ - Brasil.

Myers, W. R. C. (1978). "Momentum Transfer In A Compound Channel". en. In: *Journal of Hydraulic Research* 16.2, pp. 139–150. ISSN: 0022-1686, 1814-2079. DOI: 10.1080/00221687809499626. URL: http://www.tandfonline.com/doi/abs/10.1080/00221687809499626 (visited on 11/16/2016).

Naot, D. and W. Rodi (1982). "Calculation of secondary currents in channel flow." In: *Journal of the Hydraulics Division (ASCE)* 108.8, pp. 948–968.

Naot, D., I. Nezu, and H. Nakagawa (1993). "Hydrodynamic Behavior of Compound Rectangular Open Channels". en. In: *Journal of Hydraulic Engineering* 119.3, pp. 390–408. ISSN: 0733-9429, 1943-7900. DOI: 10.1061/(ASCE)0733-9429(1993)119:

3(390). URL: http://ascelibrary.org/doi/10.1061/%28ASCE%290733-9429%281993%29119%3A3%28390%29 (visited on 11/21/2016).

Nepf H. M.; Vivoni, E. R. (2000). "Flow structure in depth-limited, vegetated flow". In: *Journal of Geophysical Research* 105 (C12). DOI: 10.1029/2000jc900145.

Nepf, H. M. (2012a). "Hydrodynamics of vegetated channels". In: *Journal of Hydraulic Research* 503.3, pp. 262–279. ISSN: 0022-1686. DOI: 10.1080/00221686.2012.696559. URL: http://www.tandfonline.com/action/journalInformation?journalCode=tjhr20$\backslash$nhttp://www.tandfonline.com/loi/tjhr20$\backslash$nhttp://dx.doi.org/10.1080/00221686.2012.696559.

Nepf, H. M. (2012b). "Flow and Transport in Regions with Aquatic Vegetation". In: *Annual Review of Fluid Mechanics* 44.1, pp. 123–142. ISSN: 0066-4189. DOI: 10.1146/annurev-fluid-120710-101048.

Nezu, I., H. Nakagawa, and A. Tominaga (1985). "Secondary Currents in a Straight Channel Flow and the Relation to Its Aspect Ratio". en. In: *Turbulent Shear Flows 4*. Ed. by L. J. S. Bradbury, F. Durst, B. E. Launder, F. W. Schmidt, and J. H. Whitelaw. Berlin, Heidelberg: Springer Berlin Heidelberg, pp. 246–260. ISBN: 978-3-642-69998-6 978-3-642-69996-2. URL: http://www.springerlink.com/index/10.1007/978-3-642-69996-2_20 (visited on 11/15/2016).

Nezu, I. (2005). "Open-Channel Flow Turbulence and Its Research Prospect in the 21st Century". In: *Journal of Hydraulic Engineering* 131 (4). DOI: 10.1061/(ASCE)0733-9429(2005)131:4(229).

Nezu, I. and M. Sanjou (2008). "Turburence structure and coherent motion in vegetated canopy open-channel flows". In: *Journal of Hydro-Environment Research* 2.2, pp. 62–90. ISSN: 15706443. DOI: 10.1016/j.jher.2008.05.003. URL: http://dx.doi.org/10.1016/j.jher.2008.05.003.

Nezu, I., K. Onitzuka, and K. Iketani (1999). "Coherent horizontal vortices in compound open-channel flows." English. In: *Hydraulic modeling: proceedings of the International Conference on Water, Environment, Ecology, Socio-economics and Health Engineering (WEESHE) : October 18-21, 1999, Seoul National University, Seoul, Korea*. OCLC: 43601961. Highlands Ranch, Colo.: Water Resources Publications, pp. 17–32. ISBN: 978-1-887201-22-3.

Nichols, C. H. B. (1981). "Volume of fluid (VOF) method for the dynamics of free boundaries". In: *Journal of Computational Physics* 39 (1). DOI: 10.1016/0021-9991(81)90145-5.

Nield, D. A. and A. Bejan (2013). *Convection in Porous Media*. en. DOI: 10.1007/978-1-4614-5541-7. New York, NY: Springer New York. ISBN: 978-1-4614-5540-0 978-1-4614-5541-7. URL: http://link.springer.com/10.1007/978-1-4614-5541-7 (visited on 06/19/2017).

Nilsson, H. (2016a). *Basics of C++ in OpenFOAM*. en. Class presentation. Chalmers University, Sweden. URL: https://pingpong.chalmers.se/public/pp/public_

courses/course07056/published/1497955220499/resourceId/3711490/content/UploadedResources/basicsOfC++.pdf.

Nilsson, H. (2016b). *Object orientation in C++ an OpenFOAM*. en. Class presentation. Chalmers University, Sweden. URL: https://pingpong.chalmers.se/public/pp/public_courses/course07056/published/1497955220499/resourceId/3711490/content/UploadedResources/objectOrientation.pdf.

"Numerical modeling of turbulent flow through isotropic porous media" (2014). In: *International Journal of Heat and Mass Transfer* 75, pp. 40–57. ISSN: 0017-9310.

Ochoa-Tapia, J. and S. Whitaker (1995a). "Momentum transfer at the boundary between a porous medium and a homogeneous fluid?I. Theoretical development". en. In: *International Journal of Heat and Mass Transfer* 38.14, pp. 2635–2646. ISSN: 00179310. DOI: 10.1016/0017-9310(94)00346-W. URL: http://linkinghub.elsevier.com/retrieve/pii/001793109400346W (visited on 06/19/2017).

— (1995b). "Momentum transfer at the boundary between a porous medium and a homogeneous fluid?II. Comparison with experiment". en. In: *International Journal of Heat and Mass Transfer* 38.14, pp. 2647–2655. ISSN: 00179310. DOI: 10.1016/0017-9310(94)00347-X. URL: http://linkinghub.elsevier.com/retrieve/pii/001793109400347X (visited on 06/19/2017).

OpenFOAMWiki (2014). *OpenFOAM guide/The SIMPLE algorithm in OpenFOAM - OpenFOAMWiki*. Wiki. URL: https://openfoamwiki.net/index.php/OpenFOAM_guide/The_SIMPLE_algorithm_in_OpenFOAM (visited on 03/13/2017).

Parnas, R. and Y. Cohen (1987). "POWER-LAW FLUIDS IN POROUS MEDIA". en. In: *Chemical Engineering Communications* 53.1-6, pp. 3–22. ISSN: 0098-6445, 1563-5201. DOI: 10.1080/00986448708911879. URL: http://www.tandfonline.com/doi/abs/10.1080/00986448708911879 (visited on 03/17/2017).

Passalacqua, A. (2008). *Porous zone in OpenFOAM – Alberto Passalacqua*. URL: http://albertopassalacqua.com/?p=82 (visited on 04/12/2016).

Pedras, M. H. and M. J. de Lemos (2001). "Macroscopic turbulence modeling for incompressible flow through undeformable porous media". en. In: *International Journal of Heat and Mass Transfer* 44.6, pp. 1081–1093. ISSN: 00179310. DOI: 10.1016/S0017-9310(00)00202-7. URL: http://linkinghub.elsevier.com/retrieve/pii/S0017931000002027 (visited on 10/17/2016).

Peralta, C., J. Schmidt, and B. Stoevesandt (2014). "The influence of orographic features on wind farm efficiencies". In: *ITM Web of Conferences* 2. Ed. by W. Medjroubi, B. Stoevesand, and C. Peralta, p. 02002. ISSN: 2271-2097. DOI: 10.1051/itmconf/20140202002. URL: http://www.itm-conferences.org/10.1051/itmconf/20140202002 (visited on 10/27/2016).

Pezzinga, G. (1994). "Velocity Distribution in Compound Channel Flows by Numerical Modeling". en. In: *Journal of Hydraulic Engineering* 120.10, pp. 1176–1198. ISSN: 0733-9429, 1943-7900. DOI: 10.1061/(ASCE)0733-9429(1994)120:10(1176). URL:

http://ascelibrary.org/doi/10.1061/%28ASCE%290733-9429%281994%29120%3A10%281176%29 (visited on 11/17/2016).

Phanikumar, M. S. and R. L. Mahajan (2002). "Non-Darcy natural convection in high porosity metal foams". In: *International Journal of Heat and Mass Transfer* 45.18, pp. 3781–3793. URL: http://www.sciencedirect.com/science/article/pii/S0017931002000893.

Polezhaev, Y. V. (2006). *Porous Medium*. English. URL: http://www.thermopedia.com/fr/content/1047/.

Pope, S. B. (2000). *Turbulent flows*. Cambridge ; New York: Cambridge University Press, p. 771. ISBN: 978-0-521-59125-6 978-0-521-59886-6.

Prandtl, L. (2004). *Prandtl's essentials of fluid mechanics*. eng. Ed. by H. Oertel and M. Böhle. 2. ed. Applied mathematical sciences 158. OCLC: 249164399. New York: Springer. ISBN: 978-0-387-40437-0.

Ribes, A. and C. Caremoli (2007). "Salome platform component model for numerical simulation". In: IEEE, pp. 553–564. ISBN: 978-0-7695-2870-0. DOI: 10.1109/COMPSAC.2007.185. URL: http://ieeexplore.ieee.org/document/4291178/ (visited on 03/01/2017).

Ritzi, R. W. and P. Bobeck (2008). "Comprehensive principles of quantitative hydrogeology established by Darcy (1856) and Dupuit (1857): QUANTITATIVE HYDROGEOLOGY". en. In: *Water Resources Research* 44.10. ISSN: 00431397. DOI: 10.1029/2008WR007002. URL: http://doi.wiley.com/10.1029/2008WR007002 (visited on 06/25/2017).

Rodi, W. (1980). "Turbulence models and their application in hydraulics - A state of the art review". In: *NASA STI/Recon Technical Report A* 81.

Roshani, E. F.F.B.J.C.H.M. S. (1993). "Correlations of pressure drop in packed beds taking into account the effect of confining wall". In: *International Journal of Heat and Mass Transfer* 36 (2). DOI: 10.1016/0017-9310(93)80028-s.

Saint-Venant, A. (1871). "Theorie du mouvement non permanent des eaux, avec application aux crues des rivieres et a l'introduction de marees dans leurs lits". fr. In: *Comptes rendus des seances de l'Academie des Sciences*.

Shi, J., T. Thomas, and J. Williams (1999). "Large-eddy simulation of flow in a rectangular open channel". In: *Journal of Hydraulic Research* 37 (3). DOI: 10.1080/00221686.1999.9628252.

Shih, T.-H., W. W. Liou, A. Shabbir, Z. Yang, and J. Zhu (1994). *A vorticity dynamics based model for the turbulent dissipation: Model development and validation*. en. Technical Report NASA-TM-106177, ICOMP-93-20, CMOTT-93-08, E-7877, NAS 1.15:106177. Cleveland, OH, United States: NASA Lewis Research Center, p. 31.

Shiono, K. and D. W. Knight (1991). "Turbulent open-channel flows with variable depth across the channel". en. In: *Journal of Fluid Mechanics* 222.-1, p. 617. ISSN: 0022-1120, 1469-7645. DOI: 10.1017/S0022112091001246. URL: http://www.journals.cambridge.org/abstract_S0022112091001246 (visited on 11/07/2016).

Slattery, J. C. (1967). "Flow of viscoelastic fluids through porous media". en. In: *AIChE Journal* 13.6, pp. 1066–1071. ISSN: 0001-1541, 1547-5905. DOI: 10.1002/aic.690130606. URL: http://doi.wiley.com/10.1002/aic.690130606 (visited on 06/22/2017).

Smart, C. L. (2013). *Hydrology Lecture 19w Groundwater 1*. en. Class presentation. Kean University, NJ, USA. URL: http://www.kean.edu/~csmart/Hydrology/Lectures (visited on 06/21/2017).

Sofialidis, D. and P. Prinos (1998). "Compound Open-Channel Flow Modeling with Nonlinear Low-Reynolds $\boldsymbol{k}$ -ϵ Models". en. In: *Journal of Hydraulic Engineering* 124.3, pp. 253–262. ISSN: 0733-9429, 1943-7900. DOI: 10.1061/(ASCE)0733-9429(1998)124:3(253). URL: http://ascelibrary.org/doi/10.1061/%28ASCE%290733-9429%281998%29124%3A3%28253%29 (visited on 11/17/2016).

Sonnenwald, F., V. Stovin, and I. Guymer (2016). "Feasibility of the Porous Zone Approach to Modelling Vegetation in CFD". In: *Hydrodynamic and Mass Transport at Freshwater Aquatic Interfaces*. Ed. by P. Rowiński and A. Marion. Cham: Springer International Publishing, pp. 63–75. ISBN: 978-3-319-27749-3 978-3-319-27750-9. URL: http://link.springer.com/10.1007/978-3-319-27750-9_6 (visited on 09/12/2016).

Souza, G. de and H. P. A. Souto (2014). "COMPARAÇÃO DOS MODELOS DE DARCY, FORCHHEIMER E BARREE E CONWAY NA SIMULAÇÃO DE RESERVATÓRIOS DE GÁS". Português. In: Universidade Católica de Petrópolis (UCP), Petrópolis/RJ, Brasil.

Speziale, C. G. (1987). "On nonlinear K-l and K -ϵ models of turbulence". en. In: *Journal of Fluid Mechanics* 178.-1, p. 459. ISSN: 0022-1120, 1469-7645. DOI: 10.1017/S0022112087001319. URL: http://www.journals.cambridge.org/abstract_S0022112087001319 (visited on 11/17/2016).

Speziale, C. G. and X.-H. Xu (1996). "Towards the development of second-order closure models for nonequilibrium turbulent flows". en. In: *International Journal of Heat and Fluid Flow* 17.3, pp. 238–244. ISSN: 0142727X. DOI: 10.1016/0142-727X(96)00028-8. URL: http://linkinghub.elsevier.com/retrieve/pii/0142727X96000288 (visited on 02/01/2017).

Speziale, C. G., S. Sarkar, and T. B. Gatski (1991). "Modelling the pressure–strain correlation of turbulence: an invariant dynamical systems approach". In: *Journal of Fluid Mechanics* 227 (-1). DOI: 10.1017/S0022112091000101.

Stallman, R. (2016). *Why Open Source misses the point of Free Software*. URL: https://www.gnu.org/philosophy/open-source-misses-the-point.html (visited on 03/22/2017).

Support, C. (2013). *OpenFOAM-Training-by-CFD-Support*. URL: http://www.cfdsupport.com/OpenFOAM-Training-by-CFD-Support/ (visited on 04/12/2016).

Tecplot, Inc. (2014). *Tecplot 360 EX User's Manual*. en. Tecplot, Inc. URL: http://www.tecplot.com/support/documentation/.

Terrier, B. (2010). "Flow characteristics in straight compound channels with vegetation along the main channel". en. PhD Thesis. Loughborough: Loughborough University. URL: https://dspace.lboro.ac.uk/2134/6326.

The Hamilton Project (2011). *Cost of Computing Power Equal to an iPad2 | The Hamilton Project*. URL: http://www.hamiltonproject.org/charts/cost_of_computing_power_equal_to_an_ipad2 (visited on 03/22/2017).

Ting, C.-L., M.-C. Lin, and C.-Y. Cheng (2004). "Porosity effects on non-breaking surface waves over permeable submerged breakwaters". en. In: *Coastal Engineering* 50.4, pp. 213–224. ISSN: 03783839. DOI: 10.1016/j.coastaleng.2003.10.003. URL: http://linkinghub.elsevier.com/retrieve/pii/S0378383903001145.

Tominaga, A. and K. Ezaki (1988). "Hydraulic characteristics of compound channel flow." en. In: *Sixth Congress, the Asian and Pacific Regional Division of the International Association for Hydraulic Research: Proceedings : Kyoto, July 20-22, 1988*. Kyoto, Japan: Local organizing committee of the congress. URL: https://books.google.pt/books?id=J9E6HAAACAAJ.

Tominaga, A. and I. Nezu (1991). "Turbulent Structure in Compound Open-Channel Flows". en. In: *Journal of Hydraulic Engineering* 117.1, pp. 21–41. ISSN: 0733-9429, 1943-7900. DOI: 10.1061/(ASCE)0733-9429(1991)117:1(21). URL: http://ascelibrary.org/doi/10.1061/%28ASCE%290733-9429%281991%29117%3A1%2821%29 (visited on 11/17/2016).

Tominaga, A., I. Nezu, K. Ezaki, and H. Nakagawa (1989). "Three-dimensional turbulent structure in straight open channel flows". In: *Journal of Hydraulic Research* 27 (1). DOI: 10.1080/00221688909499249.

Uittenbogaard, R. (2003). "Modelling turbulence in vegetated aquatic flows". en. In: Trento, Italy. URL: http://cudam.ing.unitn.it/workshop/2003/R_F.

Vafai, K., ed. (2005). *Handbook of porous media*. eng. 2. ed. Boca Raton: Taylor & Francis, p. 752. ISBN: 978-0-8247-2747-5.

Versteeg, H. K. and W. Malalasekera (2007). *An introduction to computational fluid dynamics: the finite volume method*. 2nd ed. Harlow, England ; New York: Pearson Education Ltd, p. 503. ISBN: 978-0-13-127498-3.

Whitaker, S. (1969). "ADVANCES IN THEORY OF FLUID MOTION IN POROUS MEDIA". en. In: *Industrial & Engineering Chemistry* 61.12, pp. 14–28. ISSN: 0019-7866, 1541-5724. DOI: 10.1021/ie50720a004. URL: http://pubs.acs.org/doi/abs/10.1021/ie50720a004 (visited on 06/22/2017).

Whitaker, S. (1999). *The Method of Volume Averaging*. English. OCLC: 913435706. ISBN: 978-94-017-3389-2. URL: http://public.eblib.com/choice/publicfullrecord.aspx?p=3106854 (visited on 06/23/2017).

WILCOX, D. C. (1988). "Reassessment of the scale-determining equation for advanced turbulence models". In: *AIAA Journal* 26 (11). DOI: 10.2514/3.10041.

Wilcox, D. C. (2006). *Turbulence modeling for CFD*. eng. 3. ed. La Cañada, Calif: DCW Industries. ISBN: 978-1-928729-08-2.

Williams, A. F., H. F. Burcharth, and H. Adel (1992). "The Permeability of Rubble Mound Breakwaters. New Measurements and New Ideas". In: *Coastal Engineering Proceedings* 1.23. URL: https://journals.tdl.org/icce/index.php/icce/article/viewArticle/4809.

Wright, N., A. Crossley, H. Morvan, and T. Stoesser (2004). "Detailed validation of CFD for flows in straight channels". eng. In: *River flow 2004: proceedings of the Second International Conference on Fluvial Hydraulics, 23-25 June 2004, Napoli, Italy*. Ed. by M. Greco and International Conference on Fluvial Hydraulics. Leiden: Balkema. ISBN: 978-90-5809-658-6.

Xie, Z., B. Lin, and R. A. Falconer (2013). "Large-eddy simulation of the turbulent structure in compound open-channel flows". en. In: *Advances in Water Resources* 53, pp. 66–75. ISSN: 03091708. DOI: 10.1016/j.advwatres.2012.10.009. URL: http://linkinghub.elsevier.com/retrieve/pii/S0309170812002710 (visited on 06/28/2017).

Yang, S.-Q., S. K. Tan, and X.-K. Wang (2012). "Mechanism of secondary currents in open channel flows: SECONDARY CURRENTS, SAND RIDGES, FLOWS". en. In: *Journal of Geophysical Research: Earth Surface* 117.F4, n/a–n/a. ISSN: 01480227. DOI: 10.1029/2012JF002510. URL: http://doi.wiley.com/10.1029/2012JF002510 (visited on 08/15/2017).

Yogesh, K. (2017). *BSL EARSM - OpenFOAMWiki*. URL: https://openfoamwiki.net/index.php/BSL_EARSM (visited on 02/01/2017).

Yuen, K. W. H. (1989). "A study of boundary shear stress flow resistance and momentum transfer in open channels with simple and compound trapezoidal cross-section." PhD Thesis. Birmingham, U.K.: University of Birmingham. URL: http://www.birmingham.ac.uk/research/activity/civil-engineering/archive/short-term/floods/flowdata/background/phd-theses/yuen.aspx.

Appendix A

Further considerations on the literature review

This appendix is a development of Chapter 2 with further theoretical considerations on submerged vegetated flow, supplementary models and formulations of porous flow equations and a more comprehensive *Re* characterisation in porous media flow.

A.1 Flexible Canopies and Monami

Although the scope of this thesis is on the effect of rigid dense submerged vegetation in compound channel flow, it's still important to take into account what causes and effects flexible vegetation patches have on channel flow it is a commonly observed phenomenon (Nepf, 2012b). According to Nepf (2012b), "under some conditions, the canopy-scale vortices produce sufficient instantaneous drag to overcome buoyancy and rigidity of individual blades. The passage of the travelling vortices then causes a local depression in the canopy, which travels along the canopy interface, in sync with the canopy vortices (Figure A.1a). This progressive waving of canopy blades is called a monami (...). It has been observed to occur extensively in the field (...). The frequency matches the frequency of vortex passage, which is given by instability theory (...). However, if the instantaneous drag associated with the canopy-scale vortices is not sufficient to depress individual blades, the monami does not occur, even though the canopy scale vortices are present". Nepf (2012b) goes into detailed explanation of the causes and effects of both types of flexible canopy phenomena on both the velocity profiles (A.1a) and turbulent stress profiles (Figure A.1b) of flow under both conditions as well as how the flexibility of the canopy and the presence of monami affect the turbulent exchange between the canopy and the overflow.

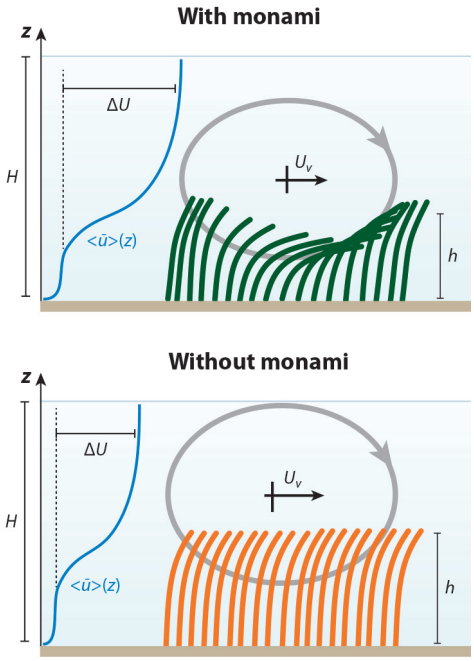

a For dense submerged canopies ($\lambda > 0.1$), the drag discontinuity at the top of the canopy generates a region of shear resembling a free shear layer, which in turn generates canopy-scale vortices by Kelvin-Helmholtz instability. The passage of these canopy-scale vortices over the canopy may generate a progressive waving of the canopy that is called a monami (*green canopy*). If the shear layer vortices are too weak, the canopy will bend but not wave (*orange canopy*).

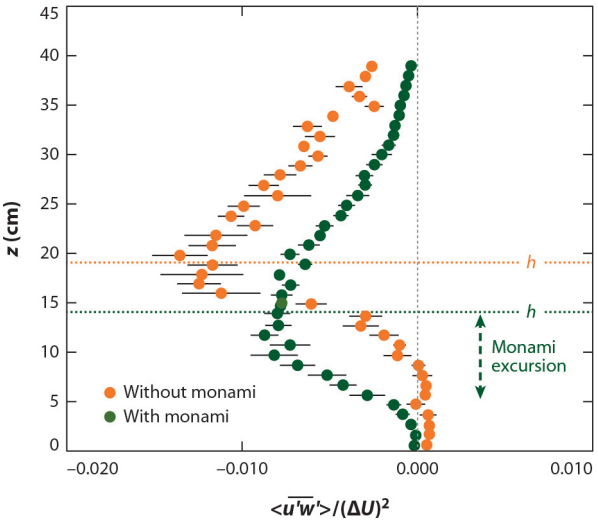

b With the weaker current, no monami occurs (*orange dots*). With a stronger current, a monami is produced (*green dots*). The vertical excurssion of the canopy interface associated with the monami i shown with the dashed double-arrow. Under the stronger current (*green dots*), the individual blades are deflected further, reducing the mean canopy height (h), relative to the conditions with the weaker current (*orange dots*).

Figure A.1: Velocity profiles on submerged flexible canopy flow with and without monami (a) and profiles of normalized turbulent stress in and above flexible canopy for two flow conditions, based on the data by Ghisalberti and Nepf, 2006. Adapted from Nepf (2012b).

A.2 Supplementary porous media models

In this section a few extra models based on the Darcy-Forchheimer porous medium flow are presented. Power law models (Parnas and Cohen, 1987) are not contemplated as there is already an included model in OpenFOAM as mentioned and exemplified in citetHafsteinsson2009, and as it is typically used to model flow of Non-Newtonian fluids in porous media. A comparison of both models quadratic and power law models has been conducted by Cheng et al. (2008).

A.2.1 Darcy-Brinkman Equation

"The Brinkman equation [Brinkman (1949)] describes the fluid flow in porous media where velocities are high with no-negligible momentum transport by shear stress. In the

Darcy model, it is effectively assumed that all stress within the flow is negligible compare[d] to the stress carried by the interface of the solid porous media. This assumption cannot be regarded to be physically realistic for high permeability porous media where at least part of the viscous stress is limited within the fluid domain. The Brinkman equation, which accounts for the transition from Darcy flow to viscous free flow, is ideal to be used for high permeability porous regimes" (Joodi et al., 2010).

"The Darcy-Brinkman equation is a governing equation for flow through a porous medium with an extra Laplacian (viscous) term (Brinkman term) added to the classical Darcy equation. The equation has been used widely to analyze high-porosity media. The dynamic viscosity, μ_e, associated with the Brinkman term is referred to as the effective viscosity. Studies in the past yielded varying results for the magnitude of the viscosity ratio [see Equation A.1] between slightly less than unity to as high as $<\sim 10$ for high porosity porous media (...)" (Liu et al., 2007). The viscosity ratio $\hat{\mu}$ is given as follows:

$$\hat{\mu} = \frac{\mu_e}{\mu} \tag{A.1}$$

where μ is the fluid viscosity, and μ_e is the effective viscosity, which "theoretically takes into account the stress within the fluid as it flows through a porous medium. However experimental of μ_e is not trivial (...). Therefore, (...), μ_e is [sometimes] set to be equal to the fluid viscosity μ" (Joodi et al., 2010).

"The validity of the Darcy-Brinkman equation has also been a subject of investigation, particularly in relation to the boundary conditions at the solid (as well as fluid) interface. (...) The analysis which solves the Navier Stokes equations rather than the Darcy equation, yields a relation between the permeability of the regular array structure and the porosity (volume fraction occupied by the flow), confirming that the Darcy equation is valid for flow through regular structures over the whole spectrum of the porosity" (Liu et al., 2007). The governing equation based on the Darcy-Brinkman equation for porous media is:

$$-\frac{\partial p}{\partial x} = \frac{\mu}{K}\mathbf{u}_D + \mu_e \nabla^2 \mathbf{u}_D \tag{A.2}$$

"The dependent variable in Darcy's law is the pressure alone, whereas pressure and direction velocities are the dependent variables in the Brinkman equation" (Joodi et al., 2010).

As described in Barree and Conway (2004), Bear and Corapcioglu (1984), Brinkman (1949), Buchart and Christensen (1911), Lai et al. (2009), Li and Ma (2011), Liu et al. (2007), Madsen and White (1976), Marques (2015), Mellink (2012), Moura (2014), "Numerical modeling of turbulent flow through isotropic porous media" (2014), Passalacqua (2008), Phanikumar and Mahajan (2002), Polezhaev (2006), Souza and Souto (2014), Ting et al. (2004), Vafai (2005), and Williams et al. (1992) there are various ways to express Darcy and non-Darcy flow mathematically. In addition to the original formulations of Darcy and Forchheimer's original work, there have also been new models proposed which seek to address the shortcomings of the Forchheimer law, in regards to the variation of

coefficients depending on fluid velocity. A brief description of these formulations and extra models will be mentioned in this section as a reference for future studies. Further details can be obtained by consulting the source materials.

A.2.2 Hydraulic gradient (I)

In his thesis, Marques (2015) makes use of an alternative formulation of the Darcy Law equation in which it's expressed in terms of the hydraulic gradient I:

$$I = -\frac{\mathrm{d}p}{\mathrm{d}x}\left(\frac{1}{g\rho}\right) \tag{A.3}$$

which when inserted in Equation 2.31 produces a dimensional coefficient, a $[s/m]$. This coefficient accounts for the pressure drop due to friction and the porous media characteristics, such as its porosity and its internal geometry. This coefficient must be calibrated on a case by case basis since it's dependent on the properties of the porous media and the fluid viscosity (Marques, 2015). It is defined in his thesis as follows:

$$I = a_I \times \mathbf{u}_D \tag{A.4}$$

where a_I $[s\ m^{-1}]$ is the linear resistance coefficient.

This then means that the Forchheimer law is now expressed as follows:

$$I = a_I \mathbf{u}_D + b_I \mathbf{u}_D |\mathbf{u}_D| \tag{A.5}$$

where b_I $[s^2\ m^{-2}]$ is the non-linear resistance coefficient.

The linear term, a_I (eq A.4) accounts for the laminar flow and the quadratic term, b_I (eq. A.5), accounts for the inertial turbulent part of the flow. Both terms must be empirically calibrated (Marques, 2015). According to observations by Buchart and Christensen, 1911, there are problems with the applicability of the Forchheimer law in the transitional regime, and so it was proposed that both the a_I and b_I coefficients take on different values depending on the flow regime. Figure A.3 illustrates how the transition from the laminar to the fully turbulent regime occurs in a continuous manner in porous media, and not abruptly such as in duct flow (Marques, 2015).

Marques (2015) elaborates further on the use of this formulation, namely the different formulations of how to obtain both coefficients and the "extended" version of these equations for application to non-stationary (multi-phase) flow. As the methodology which is the scope of this thesis is not valid for multi-phase flow (Sonnenwald et al., 2016), the equations for that type of porous media flow are not mentioned. However, this alternative formulation of the Darcy law and Forchheimer law were presented since Marques (2015) made use of IHFOAM, a newly developed three-dimensional numerical two-phase flow solver specially designed to simulate coastal, offshore and hydraulic engineering processes, which is based on OpenFOAM's interFoam solver (Cantanbria, 2014). IHFOAM defines porous media as applied in Andersen and Burcharth (1995), and any application

of a porous media as a stand in for a submerged dense patch of vegetation with that particular solver would need to take this formulation of porous media flow into account.

A.2.3 Barree-Conway equation

Although the Forchheimer equation has been used in its various forms to compensate for Darcy's law's shortcomings, it too has its own limited range of applicability as recent experimental data has shown by Barree and Conway, 2004. "At high potential gradients the flow rate cannot be predicted from Darcy or Forchheimer equations. These data also show that β is not a single valued function of permeability, as has been expected, but is as much a function of Reynolds Number as the apparent Darcy permeability. This leads to different values of β for the same proppant, depending on the range of flow rates used for the measurement" (Barree and Conway, 2004). In their paper, Barree and Conway (2004) proposed an alternative to the modified Ergun equation (see Section 2.3.4.2). In this section a brief description regarding isothermal stationary porous media flow is presented, as summed up by Jambhekar (2011) and with some references to the original source material.

"Barree and Conway (2004) performed an experimental analysis of the non-Darcy flows through porous media. They represented the Forchheimer equation in a form similar to the Darcy equation as given below" (Jambhekar, 2011):

$$\frac{\partial P}{\partial x} = -\frac{\mu}{K_{app}}\mathbf{u}_D \tag{A.6}$$

where $\mathbf{u}_D$ is the Forchheimer velocity vector and K_{app} is called apparent permeability and is defined as follows:

$$\frac{1}{K_{app}} = \frac{1}{K}\left(1 + \beta\frac{K\rho|\mathbf{u}_D|}{\mu}\right) \tag{A.7}$$

Thus, the Forchheimer equation can be rewritten as below:

$$\frac{\partial p}{\partial L} = -\frac{\mu}{K}\mathbf{u}_D\left(1 + \beta\frac{K\rho|\mathbf{u}_D|}{\mu}\right) \tag{A.8}$$

As shown in Figure A.2, "the experimental data of Barre and Conway (thick blue line) did not follow the linear apparent permeability K_{app} (thin blue and red lines) given by Equation A.6 for a constant Forchheimer coefficient β (slope). Thus, Barree and Conway (2004) argued that the Forchheimer coefficient β and thus, the apparent permeability K_{app} must vary with the flow rate. Barree and Conway also stated that a general model for a non-Darcy flow can be obtained by giving up on the expectation for a constant Forchheimer coefficient β. (...)

From Equation [A.6], Barree and Conway suggested that the apparent permeability K_{app} can also be given as follows:

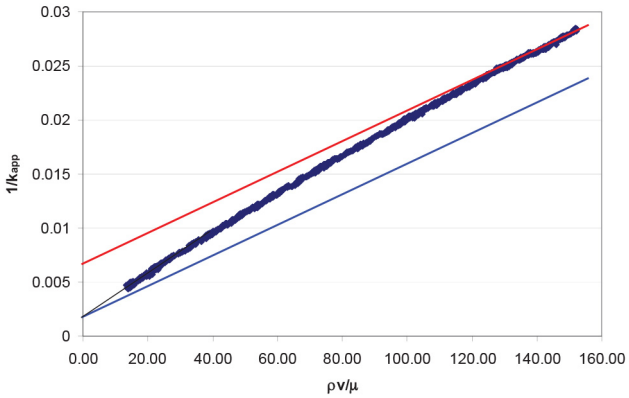

Figure A.2: Deviation of experimental data from Forchheimer linear equation (Barree and Conway, 2004).

$$K_{app} = \frac{K}{1 + Re} \tag{A.9}$$

where the Reynolds Number Re (see Equation [2.26]) is evaluated based on the characteristic length $\beta\ K\ [m]$. There exists no direct relationship for the interpretation of the Forchheimer coeeficient β and it has to be determined from the experimental data" (Jambhekar, 2011).

Jambhekar (2011) goes on to comment on the applicability of this model for multiphase flow, even though his own case study does not make use of it. His discussion will not be included here.

Although OpenFOAM doesn't make use of this model, the open-source nature of its code means that in can be applied to a numerical solver if a user so wishes, just as the authors of the IHFOAM solver applied the Andersen and Burcharth (1995) approach in defining porous media, or more to the point, how Gooya (2014) applied the Darcy-Brinkman equation to define porous media. The reason for using such a model would be to validate it given that it aims to be a general purpose model, and Barree and Conway (2004) initial findings show a possible general correlation for characteristic length τ (see Section 2.3.3.5) with permeability K for all porous media. Although that relation had not yet been confirmed at the time of publication, and was presented in the article pending future study and evaluation, continued use of this formulation in works published since then seem to suggest that it might hold true. It would seem then fortuitous to also verify its validity for the topic of this thesis, i.e., dense submerged vegetation as porous media.

A.3 Reynolds number (Re) in porous media flow

In his work, Marques (2015) cites Dybbs and Edwards (1994) who define the porous medium Reynolds number Re_p as dependent on grain size, porosity and fluid velocity in the pores, as follows:

$$Re_p = \frac{u_s d_p \rho}{\mu} \tag{A.10}$$

where d_p is the pore diameter and $\mathbf{u}_s$, the fluid velocity in the pores (seepage velocity).

Marques (2015) describes the flow in porous media (see Figure A.3 as first described and illustrated by Dybbs and Edwards (1994), later summarized by Andersen and Burcharth (1995) and quoted here from this later source, with additional remarks and adapted figures by Marques (2015):

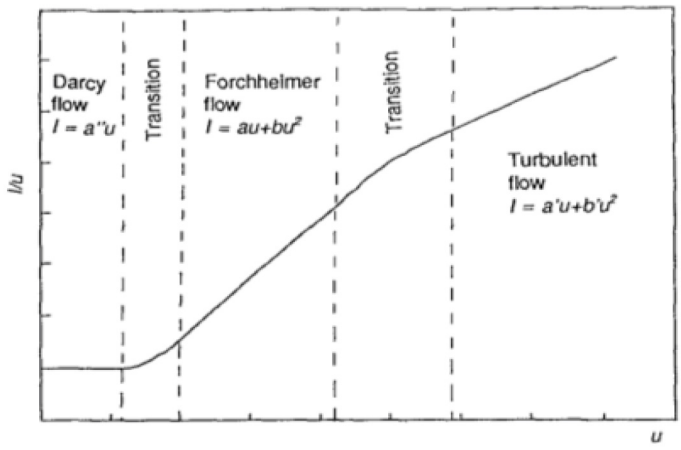

Figure A.3: Porous media flow regions. Adapted from Marques (2015).

1. The Darcy flow regime

   "The Darcy or creeping flow regime where the flow is dominated by viscous forces and the exact nature of the velocity distribution is determined by local geometry. This type of flow occurs at $Re < 1$. At $Re \simeq 1$, boundary layers begin to develop near the solid boundaries of the pores" (Andersen and Burcharth, 1995).

2. The Forchheimer flow regime

   "The inertial flow regime. This initiates at *Re* between 1 and 10 where the boundary layers become more pronounced and an 'inertial core' appears. The developing of these 'core' flows outside the boundary layers is the reason for the non-linear relationship between pressure drop and flow rate. As the *Re* increases, the 'core' flows enlarge in size and their influence becomes more and more significant on the overall flow picture. This steady non-linear laminar flow regime persists to a $Re \sim 150$" (Andersen and Burcharth, 1995). "The energy loss (...) is due to friction in the flow through the narrow tortuous paths of the porous medium" (Bear, 1988). In this regime, the flow remains laminar (see Figure A.4), however the relation between the pressure gradient and fluid velocity is non-linear (Marques, 2015).

3. The transitional regime

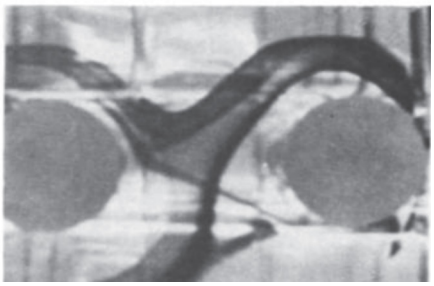

Figure A.4: Porous media flow with Re_p = 86. Adapted from Marques (2015).

"An unsteady laminar flow regime in the Reynolds number range of 150 to 300. At $Re \sim 150$, the first evidence of unsteady flow is observed in the form of laminar wake oscillations in the pores" (see Figure A.5). "These oscillations take the form of travelling waves characterised by distinct periods, amplitudes and growth rates. In this flow regime, these oscillations exhibit preferred frequencies that seem to correspond to specific growth rates. Vortices form at $Re \sim 250$ and persist to $Re \sim 300$" (Andersen and Burcharth, 1995).

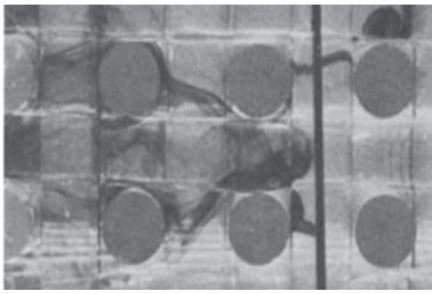

Figure A.5: Porous media flow with Re_p = 225. Adapted from Marques (2015).

4. The fully turbulent (rough turbulent) flow regime

   " A highly unsteady and chaotic flow regime for $Re > 300$, qualitatively resembling turbulent flow" (Andersen and Burcharth, 1995), (see Figure A.6).

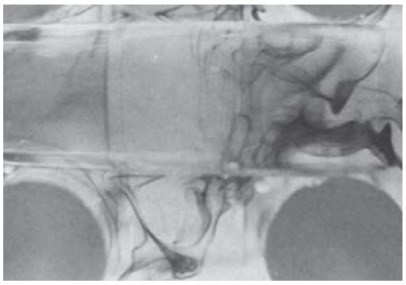

Figure A.6: Porous media flow with Re_p = 305. Adapted from Marques (2015).

Table A.1 sums up the porous media flow regimes and the valid equations for each regime, following the formulation described in Section (2.3.4.2). It's important to mention

that the constant a_I' in the fully turbulent flow regime is only used as a mathematical adjustment and holds no physical meaning (Marques, 2015).

Table A.1: Porous Media regime flow classification. Adapted from Marques (2015)

Flow Regime	**Reynolds (Re_p)**	**Equation (Figure 2.8)**
Darcy	$Re_p < [1,10]$	$I = a_I''\mathbf{u}_D$
Forchheimer	$[1,10] < Re_p < 150$	$I = a_I\mathbf{u}_D + b_I{\mathbf{u}_D}^2$
Transitional	$150 < Re_p < 300$	
Fully turbulent	$300 < Re_p$	$I = a_I'\mathbf{u}_D + b_I'{\mathbf{u}_D}^2$

Furthermore, Barree and Conway, 2004 state that "to adequately model non-linear flow behaviour the value of Re can be expressed in terms of $\rho\ \mathbf{u}/\mu$ to some transition constant, τ_t, that can be determined by non-linear regression of actual lab apparent permeability data.

$$Re = \frac{\rho\mathbf{u}}{\mu\tau_t} \tag{A.11}$$

The advantages of this approach is that the valued of τ is a constant for any system, and is not dependent on the experimental conditions under which it is determined, which is the case with β" (see Sections 2.3.4.2 and A.2.3).